



**POLITECNICO
MILANO 1863**

SCHOOL OF INDUSTRIAL AND INFORMATION ENGINEERING

Master of Science in Mechanical Engineering

**INVESTIGATIONS OF SURFACE REGULAR
PATTERNING THROUGH MICROMILLING**

Supervisor: Massimiliano Pietro Giovanni ANNONI

Co-supervisor: Paolo PARENTI

Luca SIMEON

899205

Academic Year: 2018/2019

Acknowledgments

I would first like to thank my thesis advisor Prof. Massimiliano Annoni of the Mechanical Engineering School at Politecnico di Milano for the technical support provided during the development of this master thesis. I would also like to extend warm thanks to PhD Paolo Parenti for supporting me with his advice during all the thesis work.

Special thanks also to Ing. Salvatore Cataldo for his help and support during all this work. Finally, I would also take this opportunity to express gratitude to all the Tecnologie Meccaniche laboratory members at Politecnico di Milano, especially Ing. Francesco Cacciatore and Ing. Pasquale Aquilino for always been ready to offer me the support during all the experiments inside the laboratory.

Abstract

The diffraction gratings are regular structures made on the surface of a certain workpiece, through the use of different technological processes. These gratings are nothing but evenly spaced regular structures generated by technologies i.e. laser, chemical processes or microcutting of a tool. The micromilling process, therefore, is well inserted in this context: the aim of the research work is to study primarily the feasibility and then the quality of textured surfaces, proceeding with an investigation and optimization of the various cutting parameters, through various experiments conducted on test pieces. The analysis is carried out by acquiring the surfaces under the microscope to extract various parameters related to the regularity of the surface and its roughness.

Part of the research is carried out in collaboration with the University of Bradford in order to study the impact of the cutting parameters on the realization of regular surfaces on Stavax ESR steel injection molding inserts, while a part is in collaboration with the university of Padua in order to study the capability of the micromills to generate this regular surface on NiP coated steel.

The results obtained show that through the selection of the optimal cutting parameters and an in-depth understanding of the cutting mechanism, these regular structures can be recreated on surfaces of different materials by micromilling.

Keywords: micromilling, regular structures, diffraction gratings, Stavax ESR steel, NiP coating.

Abstract (Italiano)

I reticoli di diffrazioni sono strutture regolari realizzate sulla superficie di un certo pezzo, attraverso l'impiego di diversi processi tecnologici. Tali reticoli non sono altro che strutture regolari equamente spaziate, generate da tecnologie come il laser, processi chimici o microlavorazioni con utensile. Il processo di microfresatura, perciò, si inserisce bene in questo contesto: l'intento di tale lavoro di ricerca è quello di studiare in primis la fattibilità ed in seguito la qualità di superfici testurizzate, procedendo con un'investigazione e un'ottimizzazione dei vari parametri di taglio, attraverso varie sperimentazioni condotte su pezzi di prova. L'analisi è condotta acquisendo tali superfici al microscopio al fine di estrarre vari parametri riferiti alla regolarità della superficie e alla sua rugosità.

Una parte della ricerca è svolta in collaborazione con l'Università di Bradford al fine di studiare l'impatto dei parametri di taglio sulla realizzazione di superfici regolari su inserti per stampaggio a iniezione in acciaio Stavax ESR, mentre una parte in collaborazione con l'Università di Padova al fine di studiare l'abilità delle microfresche di generare tale superficie regolare su acciaio ricoperto al NiP.

I risultati ottenuti mostrano che attraverso la selezione dei parametri di taglio ottimali e un'approfondita comprensione del meccanismo di taglio, tali strutture regolari possono essere ricreate su superfici di diversi materiali mediante microfresatura.

Parole chiave: microfresatura, strutture regolari, griglie di diffrazione, acciaio Stavax ESR, rivestimento al NiP.

Contents index

INVESTIGATIONS OF SURFACE REGULAR PATTERNING THROUGH MICROMILLING	I
ACKNOWLEDGMENTS	I
ABSTRACT.....	III
ABSTRACT (ITALIANO)	V
CONTENTS INDEX	VII
FIGURES INDEX.....	XI
TABLES INDEX.....	XVII
1. INTRODUCTION	19
1.1 INTRODUCTION AND PROBLEM STATEMENT	19
2. STATE OF THE ART	21
2.1 MACRO VS MICRO MILLING	21
2.1.1 <i>Size effect</i>	22
2.1.2 <i>Material micro-structure</i>	24
2.1.3 <i>“Minimum chip thickness”</i>	25
2.1.4 <i>Burr formation</i>	27
2.1.5 <i>Tool wear</i>	27
2.1.6 <i>Tool and workpiece deformations</i>	28
2.2 SURFACE TEXTURE CHARACTERIZATION	29
2.2.1 <i>Height parameters</i>	30
2.2.2 <i>Spatial/spacing parameters</i>	34
2.2.3 <i>Hybrid parameters</i>	37
2.3 PROCESS PARAMETERS	38
2.4 TECHNIQUES FOR MACHINING OPTICAL MOULDS.....	48

2.4.1 Diamond engraving	48
2.4.2 Diamond turning.....	51
3. AIMS OF THE WORK	55
3.1 CASE STUDY 1: MACHINING OF STAVAX ESR STEEL	55
3.2 CASE STUDY 2: MACHINING OF NiP COATING	57
4. MATERIALS AND METHOD	59
4.1 USED MATERIALS	59
4.1.1 Uddeholm Stavax ESR steel (Case study 1)	59
4.1.2 H13 steel (Case study 1).....	61
4.1.3 Electroless-plated NiP steel (Case study 2)	62
4.2 MANUFACTURING SYSTEMS	63
4.2.1 Kern EVO 5-axis CNC machining centre	63
4.3 TOOL SELECTION.....	64
4.3.1 Mitsubishi D015MS2SS0.....	64
4.3.2 BFT TDMG 31 040 KA60.....	64
4.3.3 Zecha 481.030	64
4.4 MEASUREMENT EQUIPMENTS	65
4.4.1 Mahr MarSurf CWM 100	65
4.5 SENSORS AND ACQUISITION CHAIN	67
4.5.1 Kistler Microdynamometer 9317b.....	67
4.5.2 Kistler MicroDyn type 9109AA.....	68
4.6 SOFTWARES.....	69
4.7 SETUP	70
4.7.1 Setup for case study 1.....	70
4.7.2 Setup for case study 2.....	72
5. MODELLING AND CALCULATIONS.....	75
5.1 MODELLING OF CUTTING OPERATIONS	75
5.2 MODELLING OF THE RUN-OUT ON SURFACE REGULARITY	80
5.3 CALCULATIONS ON CUTTING PARAMETERS FOR STAVAX STEEL	81
5.4 CALCULATIONS ON NiP COATING RADIAL DEPTH OF CUT	81
6. CASE STUDY 1: EXPERIMENTS	83
6.1 SCREENING OPERATIONS ON H13 STEEL	83

6.1.1 Response variable: F_{xy}	85
6.1.2 Response variable: F_z	87
6.1.3 Response variable: F_{tot}	88
6.1.4 Response variable: S_a	90
6.1.5 Effect of the cutting parameters on regularity	91
6.2 EXTENDED EVALUATION ON H13 STEEL	95
6.2.1 Response variable: F_{xy}	97
6.2.2 Response variable: F_{tot}	101
6.2.3 Response variable: S_a	104
6.2.4 Effect of the cutting parameters on regularity	107
6.2.5 Selection of the values for each working parameter	113
6.3 EVALUATION OF THE OVERLAP ON H13 STEEL	113
6.3.1 Overlap: 0%	114
6.3.2 Overlap: 10%	115
6.3.3 Overlap: 40%	115
6.3.4 Overlap: 70%	116
6.3.5 Selection of the value of overlap	118
6.4 MACHINING OF THE STAVAX ESR STEEL INSERTS	118
6.4.1 Experiments on the test insert	119
6.4.2 Cutting parameters for machining the inserts	120
6.4.3 Machining of the inserts	121
7. CASE STUDY 2: EXPERIMENTS	125
7.1 PREVIOUS EXPERIMENTS	125
7.2 TEST ON NIP EVALUATING THE INFLUENCE OF CUTTING PARAMETERS	128
7.2.1 Response variable: S_a	130
7.2.2 Response variable: Str	131
7.2.3 Acquired surfaces varying the cutting parameters	133
7.3 TEST ON NIP EVALUATING Z-STEP, TOOL AND INCLINATION ANGLE	135
7.3.1 Response variable: S_a	136
7.3.2 Response variable: Str	138
7.3.3 Acquired surfaces varying z-step, tool and angle	140
7.4 RESULTS ON NIP COATING	142
8. CONCLUSIONS.....	145
8.1 CONCLUSIONS ON CASE STUDY 1	145

8.2 CONCLUSIONS ON CASE STUDY 2.....	146
9. APPENDIX.....	149
9.1 APPENDIX A	149
9.2 APPENDIX B.....	155
9.3 APPENDIX C.....	157
9.4 APPENDIX D	159
9.5 APPENDIX E.....	161
9.6 APPENDIX F.....	163
REFERENCES.....	167

Figures index

Figure 1. Schematic of the cutting edge in (a) conventional macro-scale and (b) micro-scale cutting [1].	22
Figure 2. Schematic of the cutter's edge and of the partial effective rake angle for two different points, c_1 and c_2 , within the chip [3].	23
Figure 3. SEM image of the cutting edge of a 200 μm ball end mill [6].	23
Figure 4. End milling of ductile iron workpiece [7].	24
Figure 5. Chip formation mechanism in micro machining [3].	25
Figure 6. Intermittent cut condition [10].	26
Figure 7. Chip load/force for: (a) ferrite and (b) perlite [11].	26
Figure 8. Optical images of tool profiles: (a) sharp new tool and (b) worn tool [13].	28
Figure 9. Schematic illustration of the basic components of surface texture [15].	30
Figure 10. Example of positive and negative Skewness [17].	32
Figure 11. Example of Kurtosis >3 and <3 [17].	33
Figure 12. Autocorrelation peak with applied threshold of 0.2 (white part above the threshold) [16].	34
Figure 13. Shortest radius measured from the centre to the contour of the thresholded lobe on the autocorrelation plot [16].	35
Figure 14. Minimum and maximum radii measured on the central lobe of the autocorrelation plot [16].	36
Figure 15. Polar spectrum graph representing the texture directions [16].	37
Figure 16. CAM simulation of circular pocket milling operation [18].	38
Figure 17. Surface of micro milled circular pocket [18].	39
Figure 18. Surface roughness as a function of experimental conditions [18].	40
Figure 19. Surface roughness as function of (a) rotational cutting speed, (b) depth of cut, (c) feed rate [19].	41
Figure 20. (a) the old strategy, (b) the new strategy [21].	42
Figure 21. The comparison of the geometries of (a) features by old strategy and (b) features by new strategy, (c) the comparison of the average profiles [21].	43
Figure 22. Surface roughness as a function of pixel number [21].	43

Figure 23. Surface roughness as a function of different cutting parameters using a flat end mill [22].	44
Figure 24. Surface roughness as a function of different cutting parameters using a ball end mill [22].	44
Figure 25. 3D topography of machined surface using (a) a flat end mill, (b) a ball end mill [22].	45
Figure 26. Effect of milling speed on (a) 2D surface roughness and (b) 3D surface roughness [23].	45
Figure 27. Effect of feed per tooth on (a) 2D surface roughness and (b) 3D surface roughness [23].	46
Figure 28. Effect of depth of cut on (a) 2D surface roughness and (b) 3D surface roughness [23].	46
Figure 29. Theoretical surface with three different inserts [24].	47
Figure 30. (a) theoretical and (b) measured profile at constant feed per tooth [24].	47
Figure 31. Theoretical and measured surface roughness as a function of feed per tooth [24].	48
Figure 32. Drawing of the mould insert [25].	48
Figure 33. Machined mould insert [25].	49
Figure 34. Diamond engraved mould insert (a) 200 lines/mm, (b) 100 lines/mm, (c) 30 lines/mm, magnification x1500 [25].	49
Figure 35. (a) scheme of tool path cutting operation, (b) detail of cutting operation [26].	50
Figure 36. (a) atomic microscope image of machined surface, (b) an extracted profile [26].	50
Figure 37. Diamond turning machining setup [27].	51
Figure 38. SEM photographs of the Fresnel microstructure: (a) general view and (b) detailed view [27].	52
Figure 39. Measurement results of the Fresnel microstructure: (a) 3D interferometer image, (b) 2D interferometer image, and (c) 2D cross-sectional profile [27].	52
Figure 40. (a) diamond turned mould insert, (b) surface topography measured with a white light interferometer and (c) extracted surface profile A-B [28].	53
Figure 41. Surface profile of the injection moulded (a) PMMA surface, (b) COC surface, (c) COP surface [28].	53
Figure 42. Drawing of the moulded part containing the microneedles.	56
Figure 43. Insert for injection moulding to be machined.	57
Figure 44. Drawing of the mould and the reflex insert for injection moulding of the RRs.	57
Figure 45. Kern EVO 5-axis CNC machining centre.	63
Figure 46. Mahr MarSurf CWM 100.	65

Figure 47. Forces acquisition set up: (a) load cell, (b) channel x, y and z.	67
Figure 48. Acquisition system scheme for Kistler 9317b.	68
Figure 49. Kistler MicroDyn type 9109AA.	68
Figure 50. Acquisition system scheme for Kistler 9109AA.	69
Figure 51. (a) sample 1 and (b) sample 2 in H13 steel for screening operations.	70
Figure 52. 3D view of the aluminum support.	71
Figure 53. Design of the flat insert for cutting tests on NiP.	73
Figure 54. Influence of the back cut on the surface topography [29].	75
Figure 55. Influence of the microgeometric properties of cutting edges on the surface roughness, comparing an ideal shape with a detailed representation [29].	76
Figure 56. (a) undeformed tool, (b) bended tool.	76
Figure 57. Tool with infinite stiffness cutting scheme.	78
Figure 58. Trajectory done by the two teeth of a mill.	78
Figure 59. Tool with finite stiffness cutting scheme.	79
Figure 60. Regular structure generated by the passage of the tool.	79
Figure 61. Scheme of the inclined tool (rotation of the B-axis).	80
Figure 62. Scheme to calculate the radial depth of cut.	82
Figure 63. (a) individual value plot for F_{xy} , (b) main effect plot for F_{xy} , screening on H13.	85
Figure 64. (a) scatterplot for F_{xy} of SRES vs FITS; S; fz; a_p , (b) probability plot of SRES, screening on H13.	86
Figure 65. (a) individual value plot for F_z , (b) main effect plot for F_z .	87
Figure 66. (a) scatterplot for F_z of SRES vs FITS; S; fz; a_p , (b) probability plot of SRES.	88
Figure 67. (a) individual value plot for F_{tot} , (b) main effect plot for F_{tot} .	88
Figure 68. (a) scatterplot for F_{tot} of SRES vs FITS; S; fz; a_p , (b) probability plot of SRES.	89
Figure 69. (a) individual value plot for S_a , (b) main effect plot for S_a .	90
Figure 70. (a) scatterplot for S_a of SRES vs FITS; S; fz; a_p , (b) probability plot of SRES.	91
Figure 71. (a) extracted area, (b) 3D extracted area, (c) extracted profile at $V_c=141.4$ m/min, $f_z=30$ μ m/tooth, $a_p=0.08$ mm (replica 1).	92
Figure 72. (a) extracted area, (b) 3D extracted area, (c) extracted profile at $V_c=141.4$ m/min, $f_z=30$ μ m/tooth, $a_p=0.08$ mm (replica 2).	93
Figure 73. (a) extracted area, (b) 3D extracted area, (c) extracted profile at $V_c=141.4$ m/min, $f_z=15$ μ m/tooth, $a_p=0.08$ mm.	93
Figure 74. (a) extracted area, (b) 3D extracted area, (c) extracted profile at $V_c=94.2$ m/min, $f_z=30$ μ m/tooth, $a_p=0.04$ mm.	94

Figure 75. (a) extracted area, (b) 3D extracted area, (c) extracted profile at $V_c=188.5$ m/min, $f_z=7$ $\mu\text{m}/\text{tooth}$, $a_p=0.08$ mm.	95
Figure 76. (a) individual value plot for F_{xy} , (b) main effect plot for F_{xy} , extended tests on H13.	97
Figure 77. Interaction plot for F_{xy} , extended tests on H13.	98
Figure 78. (a) scatterplot for F_{xy} of SRES vs FITS; S ; f_z ; a_p , (b) probability plot of SRES, extended tests on H13.	99
Figure 79. Probability plot of SRES of the reduced model, extended tests on H13.	100
Figure 80. (a) individual value plot for F_{tot} , (b) main effect plot for F_{tot} , extended tests on H13.	101
Figure 81. Interaction plot for F_{tot} , extended tests on H13.	101
Figure 82. (a) scatterplot for F_{tot} of SRES vs FITS; S ; f_z ; a_p , (b) probability plot of SRES, extended tests on H13.	103
Figure 83. Probability plot of SRES of the reduced model, extended tests on H13.	103
Figure 84. (a) individual value plot for S_a , (b) main effect plot for S_a , extended tests on H13.	104
Figure 85. Interaction plot for S_a , extended tests on H13.	105
Figure 86. (a) scatterplot for S_a of SRES vs FITS; S ; f_z ; a_p , (b) probability plot of SRES, extended tests on H13.	106
Figure 87. Extracted profile at $V_c=141.4$ m/min, $f_z= 15$ $\mu\text{m}/\text{tooth}$, $a_p=0.07$ mm (a) replica 1, (b) replica 2, (c) replica 3.	107
Figure 88. Extracted profile at $V_c=141.4$ m/min, $f_z= 30$ $\mu\text{m}/\text{tooth}$, $a_p=0.07$ mm (a) replica 1, (b) replica 2, (c) replica 3.	108
Figure 89. Extracted profile at $V_c=141.4$ m/min, $f_z= 15$ $\mu\text{m}/\text{tooth}$, $a_p=0.10$ mm (a) replica 1, (b) replica 2, (c) replica 3.	109
Figure 90. Extracted profile at $V_c=141.4$ m/min, $f_z= 30$ $\mu\text{m}/\text{tooth}$, $a_p=0.10$ mm (a) replica 1, (b) replica 2, (c) replica 3.	109
Figure 91. Extracted profile at $V_c=188.5$ m/min, $f_z= 15$ $\mu\text{m}/\text{tooth}$, $a_p=0.07$ mm (a) replica 1, (b) replica 2, (c) replica 3.	110
Figure 92. Extracted profile at $V_c=188.5$ m/min, $f_z= 30$ $\mu\text{m}/\text{tooth}$, $a_p=0.07$ mm (a) replica 1, (b) replica 2, (c) replica 3.	111
Figure 93. Extracted profile at $V_c=188.5$ m/min, $f_z= 15$ $\mu\text{m}/\text{tooth}$, $a_p=0.10$ mm (a) replica 1, (b) replica 2, (c) replica 3.	111
Figure 94. Extracted profile at $V_c=188.5$ m/min, $f_z= 30$ $\mu\text{m}/\text{tooth}$, $a_p=0.10$ mm (a) replica 1, (b) replica 2, (c) replica 3.	112

Figure 95. (a) extracted area, (b) extracted profile at 0% overlap.	114
Figure 96. (a) extracted area, (b) extracted profile at 10% overlap.	115
Figure 97. (a) extracted area, (b) extracted profile at 40% overlap.	116
Figure 98. (a) extracted area, (b) extracted profile at 70% overlap.	117
Figure 99. (a) extracted area, (b) 3D extracted area, (c) extracted profile for Insert A.	121
Figure 100. (a) extracted area, (b) 3D extracted area, (c) extracted profile for Insert B.	122
Figure 101. (a) extracted area, (b) 3D extracted area, (c) extracted profile for Insert C.	123
Figure 102. Effect of (a), (c) feed per tooth and (b), (d) cutting speed on surface roughness [31].	126
Figure 103. Scheme of the manufacturing with (a) prism fabrication using a traditional milling process, (b) NiP coating deposition and (c) finishing passes [31].	127
Figure 104. Surface topography of the 18.4° tilted faces on (a) NiP and (b) NiP 2 mould inserts [31].	128
Figure 105. (a) individual value plot for Sa, (b) main effect plot for Sa, first experimental campaign on NiP coating.	130
Figure 106. (a) scatterplot for Sa of SRES vs FITS; Vc; fz; angle, (b) probability plot of SRES, first experimental campaign on NiP coating.	131
Figure 107. (a) individual value plot for Str, (b) main effect plot for Str, first experimental campaign on NiP coating.	131
Figure 108. (a) scatterplot for Str of SRES vs FITS; Vc; fz; angle, (b) probability plot of SRES, first experimental campaign on NiP coating.	132
Figure 109. (a) extracted area, (b) 3D extracted area, (c) extracted profile at Vc=14 m/min, fz=1.5 μm/tooth, angle=7°.	133
Figure 110. (a) extracted area, (b) 3D extracted area, (c) extracted profile at Vc=21 m/min, fz=2 μm/tooth, angle=7°.	134
Figure 111. (a) extracted area, (b) 3D extracted area, (c) extracted profile at Vc=17.5 m/min, fz=1 μm/tooth, angle=12°.	134
Figure 112. (a) individual value plot for Sa, (b) main effect plot for Sa, second experimental campaign on NiP coating.	136
Figure 113. (a) scatterplot for Sa of SRES vs FITS; z step; tool; angle, (b) probability plot of SRES, second experimental campaign on NiP coating.	137
Figure 114. Probability plot of SRES of the reduced model, second experimental campaign on NiP coating.	138
Figure 115. (a) individual value plot for Str, (b) main effect plot for Str, second experimental campaign on NiP coating.	138

Figure 116. (a) scatterplot for Str of SRES vs FITS; Vc; fz; angle, (b) probability plot of SRES, second experimental campaign on NiP coating.	139
Figure 117. (a) extracted area, (b) 3D extracted area, (c) extracted profile at z-step=1 μm , new tool, angle=7°.	140
Figure 118. (a) extracted area, (b) 3D extracted area, (c) extracted profile at z-step=3 μm , new tool, angle=7°.	141
Figure 119. (a) extracted area, (b) 3D extracted area, (c) extracted profile at z-step=5 μm , new tool, angle=12°.	141
Figure 120. Picture of the three machined inserts.	146
Figure 121. 3D extracted area (a) z-step=1 μm , new tool, angle=7°, (b) z-step=3 μm , new tool, angle=7°.	148

Tables index

Table 1. <i>Chemical composition of Stavax ESR steel.</i>	59
Table 2. <i>Chemical composition of H13 steel.</i>	61
Table 3. <i>Factors and outputs for screening operation on H13, sample 1.</i>	84
Table 4. <i>Factors and outputs for screening operation on H13, sample 2.</i>	84
Table 5. <i>Design of experiments on H13 and outputs.</i>	96
Table 6. <i>Factors level for previous test on NiP coating [31].</i>	125
Table 7. <i>Mean values of surface roughness and waviness for the NiP-coated moulds and moulded RRs [31].</i>	127
Table 8. <i>Surface parameters for NiP 1 and NiP 2 [31].</i>	128
Table 9. <i>Factors and outputs for NiP evaluation of cutting parameters.</i>	129
Table 10. <i>Factors and outputs for NiP evaluation of z-step, tool and angle as parameters.</i>	135
Table 11. <i>Mean values of Sa and Str varying the z-step.</i>	142
Table 12. <i>Extracted surfaces of NiP coating for the tests on cutting parameters.</i>	164

1. INTRODUCTION

1.1 Introduction and problem statement

The demand for micro-scale products used in the biomedical and consumer electronics industries has been increasing in recent years. Among micro processing, micromilling, micro electro discharge machining and microlaser processing are common techniques used to manufacture micro-scale parts made with different materials. Micromilling is a process of chip removal which, as stated in the name, is part of the world of micromachining and whose bases, however, derive from conventional milling on a macroscopic scale. This process is constantly evolving and finds particular use in the mould sector, thanks to its high versatility in the realization of 3D components in an accurate and repeatable way.

In the field of the realization of complex microstructures, the micromilling is able to confer optical properties to the surface of a material through the realization of regular structures, which are nothing more than equidistant structures with the same geometry, characterized therefore by a certain regularity. This regular surface is therefore able to function as an optic and can be used in different sectors, i.e. monitoring or security system. In this case it's possible to call it optical micromilling, as it is possible to use this technology both to directly texture the surface of a certain material and through replication with moulding processes. Micromilling is able to

produce microstructures characterized by complex geometries, such as micromoulds for injection moulding: the area of injection moulding is of great industrial interest thanks to the possibility of producing large batches of low-cost micro-components. This research work therefore starts from this idea, that is to study the micromilling process, that is to understand the degree of regularity that this process can give and how it could be used in the future for processes for injection moulding. The goal is to understand the mechanism and optimize the various cutting parameters in order to create a qualitatively best possible diffraction grid directly on the surfaces of the materials being processed, through various experiments on the materials used to make moulds. The various experiments were conducted in the MI_crolab (Micro Machining Laboratory) of the Mechanical Engineering Department of the Politecnico di Milano, using a 5-axis machining centre. A part of the research is carried out in collaboration with the University of Bradford and consists in the preliminary study and finally in the realization of regular diffractive surfaces on inserts for injection moulding in Stavax ESR steel, while another part is carried out in collaboration with the University of Padua to study and create such regular surfaces on steel with NiP coating.

2. STATE OF THE ART

2.1 Macro vs micro milling

The trend toward miniaturization has increased dramatically over the last decades and it is expected to increase more and more, especially within the fields concerned with bioengineering, electronics, aerospace and many others [1]. This growing need of micro-operations is characterizing all the different technologies, from laser to waterjet operations, from additive manufacturing to removal processes etc. In this context, micromilling is well inserted: it is defined as the downscaling of traditional milling process using end mills, whose diameters are in a sub-millimetre range [2]. Micromilling has established its importance in micro context due to its higher material removal rate (MRR) compared to other micro operations and its applicability in realizing microstructures with high aspect ratios and complex geometries on different engineering materials, such as metallic alloys, ceramics and polymeric materials [3][4][5].

Micro machining techniques derived from the widespread knowledge on conventional milling operations. The cutting mechanism is the same as that of conventional milling, but moving on to the micro context, new aspects emerged and were analysed and modelled in order to obtain a vast knowledge even in the micro-milling field [1]: the material is removed generating a chip by a miniaturized cutting tool set in relative rotation with respect to the workpiece, but new parameters have

to be considered to properly characterize the entire process. Many studies and researches have been done to analyze in detail these new aspects associated to micro milling; here a list of the main ones is reported:

- Size effect;
- Material micro-structure;
- “Minimum chip thickness”;
- Burr formation;
- Tool wear;
- Tool and workpiece deformations;

2.1.1 Size effect

In the transition from conventional milling to micro milling, the size effect proved to be a fundamental aspect not to be overlooked. This phenomenon occurs considering miniaturized tool used for micro operations. In fact, any tool used in macro-scale machining presents the tool edge radius (r_e) between the clearance and the rake face lower of some order of magnitude compared to the undeformed chip thickness (h) to be cut, allowing to be assumed as perfectly sharp, following on Merchant’s analysis, Figure 1(a). Based on this observation, no contact between machined surface and the clearance face occurs and the mechanism of cutting is essentially by shearing. On the other hand, the radius of the cutting edge becomes not negligible using a miniaturized tool and its value reaches the same magnitude of the thickness of material to be removed, Figure 1(b) [1][2][6].

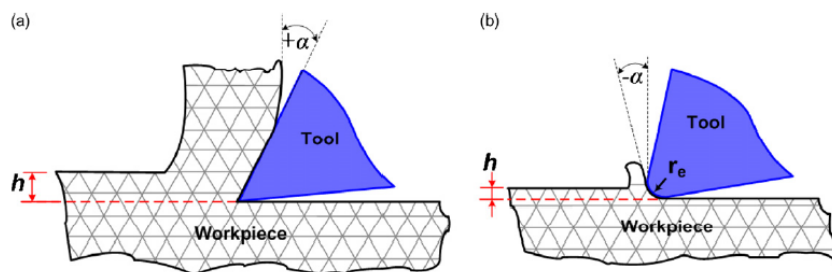


Figure 1. Schematic of the cutting edge in (a) conventional macro-scale and (b) micro-scale cutting

[1].

This is a drawback generated during the downscaling from macro to micro tools because it is not possible to scale all the dimensions proportionally, due to the limitations of the technologies used in production; as a consequence, the rake angle is not univocally defined, but it changes locally, thus the partial effective rake angle at every particular position ($\alpha_{r,e(c)}$) is defined as the inclination angle of the tangent to the arc of the cutter's edge at that particular point [3] and its value is highly negative, Figure 2.

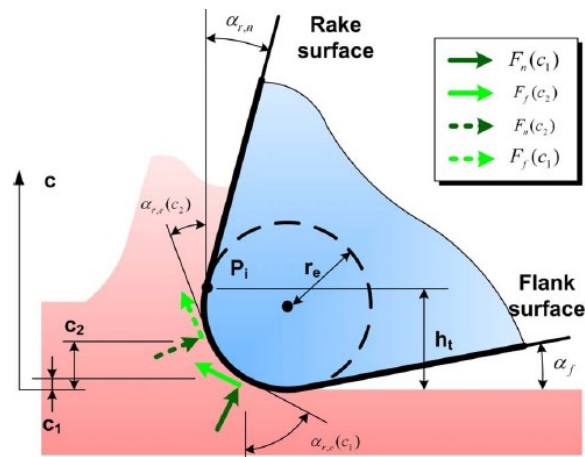


Figure 2. Schematic of the cutter's edge and of the partial effective rake angle for two different points, c_1 and c_2 , within the chip [3].

This local negative rake angle generates a ploughing effect on the previously worked surface determining a direct increase in cutting forces and a worse surface quality.

In Figure 3, a SEM image of the cutting edge of a 200 μm ball end mill, in which it is possible to observe that the edge is not perfectly sharp as could be assumed for a tool for macro operations:

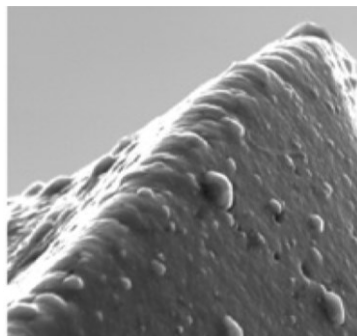


Figure 3. SEM image of the cutting edge of a 200 μm ball end mill [6].

2.1.2 Material micro-structure

While in traditional machining the material could be considered homogeneous and isotropic, in micromilling processes the material structure becomes extremely important. Cutter geometrical dimensions and chip thickness become comparable with grains, cavities and inclusions sizes, that are usually between 100 nm and 100 μm . As the depths of cut and feed rates are reduced, the chip load encountered in the process becomes the same order of magnitude as the grain size of many alloys. Whereas, in conventional milling processes, the workpiece material can be considered to be homogeneous and isotropic, in the micro-milling process, it must be modelled as heterogeneous and, in some cases, anisotropic.

This multiphase material cutting generates high variations in forces amplitude and high frequency vibrational components, proportional to phase dimensions. The force amplitude is different because phases usually have different mechanical characteristics passing from a phase to another [7]. These vibrations can lead to vibrational issues, that could accelerate also the tool breakage, and surface quality losses. In Figure 4, a drawing of an end milling operation on ductile iron workpiece, in which it is shown the different phases, i.e. graphite, ferrite, pearlite.

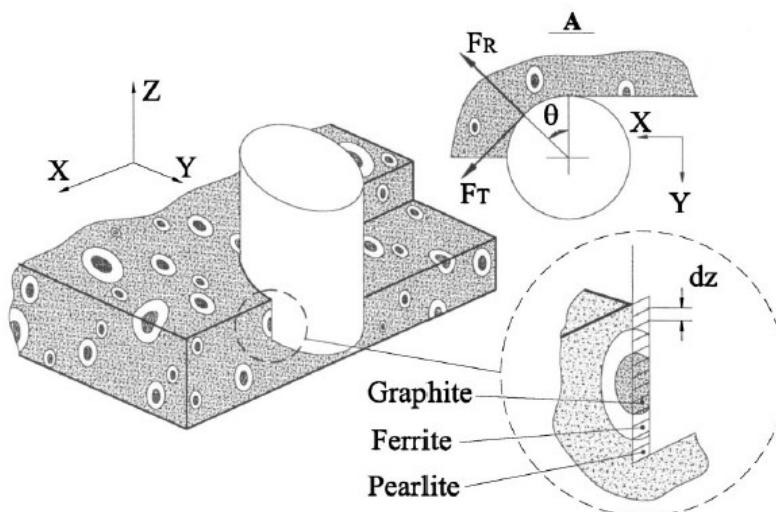


Figure 4. End milling of ductile iron workpiece [7].

2.1.3 “Minimum chip thickness”

The phenomenon of “minimum chip thickness” is fundamental in micromilling, since it has been observed that the chip formation mechanism is different from the conventional milling. Cuttings are greatly influenced by the ratio of the depth of cut to the effective cutting edge radius of the tool. In micromachining, the edge radius of the tool tends to be the same order-of-magnitude as the chip thickness. Thus, a small change in the depth of cut significantly influences the cutting process [8]. As a result, cutting takes place with a highly negative tool rake angle and the relationship between the cutting thickness and tool edge radius will set the chip removal mechanism. Thus, the chip will not form unless the cutting thickness is greater than a critical value called the minimum uncut chip thickness (h_{min}): the material is forced under the tool and then recovers back after the tool passes (elastic-plastic deformation or ploughing), therefore, no material is removed as a chip. As the cutting thickness matches and exceeds h_{min} , ploughing decreases considerably and chips are formed completely [5][9]. Figure 5 well explains these conditions:

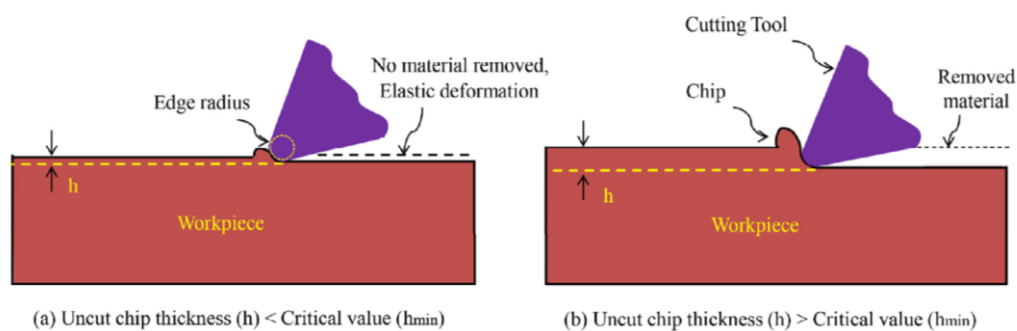


Figure 5. Chip formation mechanism in micro machining [3].

The ratio of minimum chip thickness to the cutting edge radius is essential in micromachining in order to avoid or minimize the ploughing effect and achieve desired material removal. Typical values of the ratio between minimum chip thickness over cutting edge radius are set to 0.2-0.3.

Considering this phenomenon, the cutting could be intermittent: the effect of the minimum chip thickness combined with the low stiffness of the microtools generate

the so-called intermittent cut, a condition in which the tool is not able to remove material during its feed until the threshold value of minimum chip thickness is overcome. The chip is generated and the tool returns in its undeformed condition. The intermittent cut mechanism is shown in Figure 6:

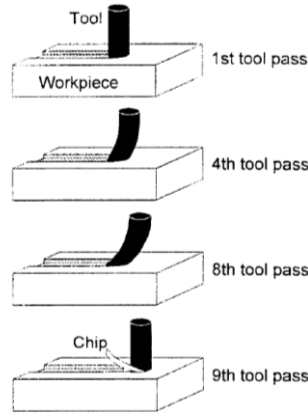


Figure 6. Intermittent cut condition [10].

As shown by the picture, since the cutting is not continuous, the chip thickness is higher than the predicted one, imposed by the feed per tooth parameter and it is confirmed by the trace left on the machined surface of the workpiece.

A way to set the minimum chip thickness is to look at the values of cutting (tangential) and thrust (radial) forces in relation with the chip load: the rate of increase for both the cutting force and the thrust force is much higher for ploughing than the chip formation process. Further, there is an abrupt thrust force change at the minimum chip thickness due to the transition between the ploughing and shearing cutting mechanisms as observed experimentally [11], has shown in Figure 7:

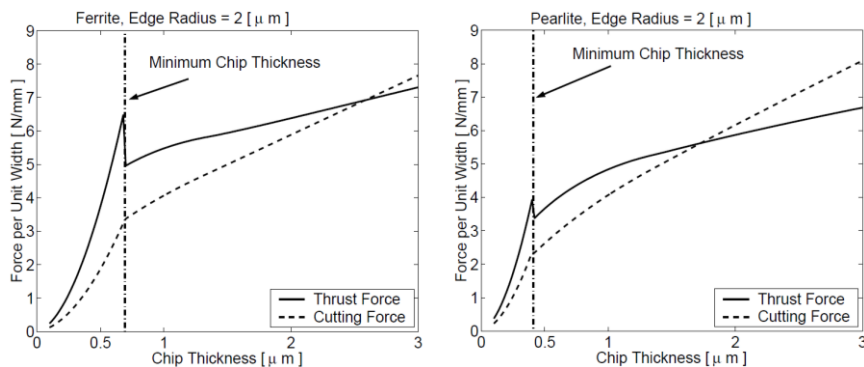


Figure 7. Chip load/force for: (a) ferrite and (b) perlite [11].

2.1.4 Burr formation

Beside surface finish, burr formation is the most critical issue in micromachining, since it affects the capability to meet desirable tolerance and geometry definition. They are not acceptable and further removal is not economically and eventually not technically feasible when the features are in the range of microns. Conventional deburring operations cannot be applied on microcomponents because it will damage the actual dimension of the part. Thus, it is important to eliminate burr formation either by developing strategies for minimization or new post-processing technology for burr removal [1][5].

In micromachining, burrs can be described as entrance, exit and top burrs. The mechanism of burr formation in micromachining has been reported to be dominated by the interaction between cutting edge radius and feed per tooth. When the ratio of undeformed chip thickness to the cutting edge radius decreases, the effective rake angle becomes more negative: material ahead the tool is pushed/compressed, flows away, bent and a portion moved in the axial direction of the tool and deformed plastically into a burr [5].

Thus, it's necessary to optimize the cutting parameters to decrease the burr height as much as possible. It has been shown that the height of the micro-burrs is linearly proportional to the feed rate and very dependent from cutting edge wear. Also, the strategy used for machining results as very influent in the burr formation: a micro-processing performed in down milling produces burrs of reduced dimensions compared to that performed in up milling [12].

2.1.5 Tool wear

Tool wear on the cutting edges of micro end mills is an important issue affecting process outputs such as tool deflections and surface roughness, especially when difficult to cut materials such as titanium alloys, stainless steel, etc. are machined at micro scale. The wear conditions of a micro-tool are different with respect to the

conditions of wear of a standard tool: the depths of cut are low and the edge radii are comparable to the uncut chip thickness during machining, which leads to plowing of the material onto the workpiece surface, instead of cutting: it exists a minimum uncut chip thickness value where continuous chip formation ceases and plowing becomes the dominant cutting mechanism. A micro-tool presents the same geometries as a standard tool, thus the chip has to flow on the rake surface of the tool: in this condition, the tool works in the right condition and the wear is reduced, ensuring a long life to the tool [13][14].

Generally, for the monitoring of the tool wear, some measuring systems based on laser are used: this procedure must be done every time a new operation starts because even a small increase in wear can have a serious impact on the quality of the final processing. In Figure 8, a picture of a sharp new tool and a worn one, on which the length of flank wear zone is indicated as VB:

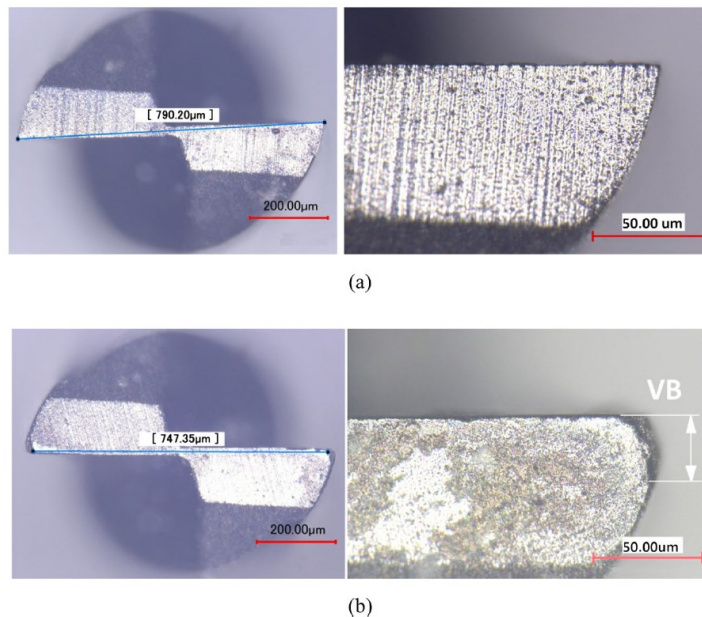


Figure 8. Optical images of tool profiles: (a) sharp new tool and (b) worn tool [13].

2.1.6 Tool and workpiece deformations

Being the milling and therefore also the micro-milling a technology that involves the contact between a tool and the workpiece, in the cutting mechanism forces are

generated and are not negligible during the chip removal process. Although the forces generated in micro-milling are contained, in some cases even lower than 1 N, it could be sufficient to determine the deflections of the tool and of the machined part, given the low stiffness of the system. The consequence of these phenomena is primarily the failure to comply with the geometric and dimensional tolerances imposed on the workpiece; if it was the tool to be deflected under the cutting forces, more serious phenomena could occur such as tool breakage, while in case of deflections in the workpiece, it would become a scrap.

2.2 Surface texture characterization

The surface texture of any part or product is usually constituted by repetitive and/or random sequences of peaks, valleys and gradients. The spatial distribution of these elements forms the entire surface texture, which can be considered to be geometrical deviations of spatial components from a hypothetically ideal, perfectly smooth surface forming a three-dimensional (3D) shape. In a 2D case, this ideal surface will be represented by a flat geometry. The surface texture significantly influences functional performance, physical-mechanical properties and visual appearance of a part or product. Some of these characteristics include wear and corrosion resistance, adhesiveness, tribological, and optical/aesthetic properties of the final product. The importance of such surface attributes is further intensified with product miniaturisation requiring complex 3D and free-form shapes. The texture of such miniature products typically contains micro/nano-scale geometric features with tolerances, accuracy, precision and surface quality having the same order of amplitudes as feature dimensions.

In general surface texture consists in two main components, i.e. roughness and waviness. Roughness refers to a measure of more closely spaced, finer, generally random irregularities of the surface texture attributed to the cutting tool edge marks and other material removal tools. Whereas, waviness is a measure of the widely

spaced repetitive irregularities resulted from the machine tool mechanical structure vibrations, chatter, heat deformations, or warping strains. Figure 9 shows a schematic illustration of the basic components of surface texture [15].

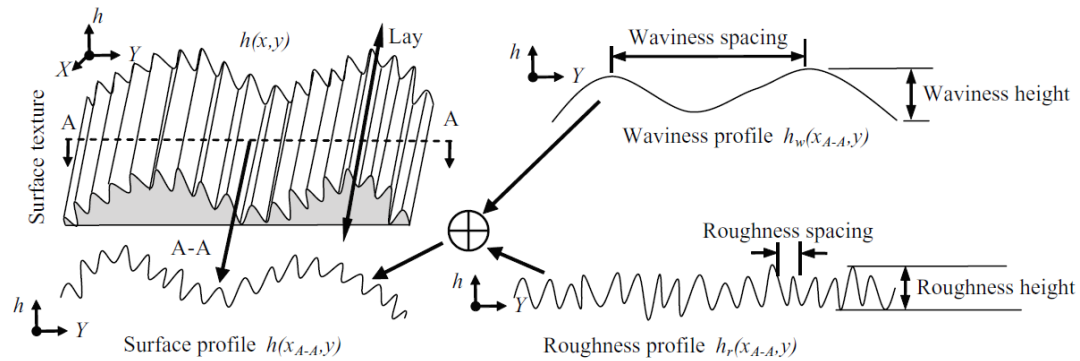


Figure 9. Schematic illustration of the basic components of surface texture [15].

Based on the distribution and nature of the spatial content of the profile surface roughness, three major classes of profile roughness parameters are used for quantitative and qualitative assessments of the surface texture [15][16].

These are:

- height parameters;
- spatial/spacing parameters;
- hybrid parameters.

2.2.1 Height parameters

Height parameters are by far the most widespread parameters. They quantify vertical deviations of the surface respect to the ideal one. S_a and S_q are respectively the Average Roughness and Root Mean Square Roughness. These parameters are evaluated over the complete 3D surface and represent an overall measurement of the texture of the surface. Being S_a and S_q insensitive in differentiating peaks, valleys and the spacing of the various texture features sometimes their application leads to a lack of accuracy. Thus, S_a or S_q may be misleading in that many surfaces with grossly different spatial and height symmetry features (e.g., milled vs. honed) may have the

same Sa or Sq, but function quite differently. Sq is typically used to specify optical surfaces and Sa is used for machined surfaces. Ssk and Sku are the Skewness and Kurtosis of the 3D surface texture respectively. Figuratively, a histogram of the heights of all measured points is established and the symmetry and deviation from an ideal Normal distribution is represented by Ssk and Sku.

Root mean square height, Sq

The root mean square height or Sq parameter is defined as the root mean square value of the surface departures, $z(x,y)$, within the sampling area, A.

$$Sq = \sqrt{\frac{1}{A} \iint_A z(x,y) dx dy}$$

Provide insufficient information on shape, presence/absence of infrequent high peaks and deep valleys in roughness profile. Sensitive to surface peak and valley [16].

Arithmetic mean height, Sa

The arithmetic mean height or Sa parameter is defined as the arithmetic mean of the absolute value of the height within a sampling area, A.

$$Sa = \frac{1}{A} \iint_A |z(x,y)| dx dy$$

Provide insufficient information on shape, presence/absence of infrequent high peaks and deep valleys in roughness profile. Sensitive to surface peak and valley [16].

Skewness, Ssk

Skewness is the ratio of the mean of the height values cubed and the cube of Sq within a sampling area, Ssk represents the degree of symmetry of the surface heights about the mean plane.

$$Ssk = \frac{1}{Sq^3} \frac{1}{A} \iint_A z^3(x,y) dx dy$$

This parameter can be positive, negative or zero, and is unit-less since it is normalized by Sq . The sign of Ssk indicates the predominance of peaks (i.e. Ssk greater than 0) or valley structures (Ssk less than 0) comprising the surface. If the surface heights are randomly distributed, so follow a Normal Gaussian distribution, then the skewness Ssk is equal to zero. This parameter cannot distinguish if the profile spikes are evenly distributed above or below the mean plane and is strongly influenced by isolated peaks or isolated valleys [16][17].

Figure 10 shows an example of positive and negative Skewness:

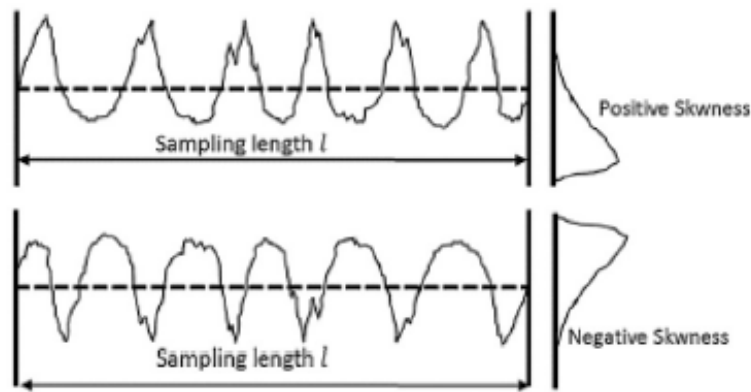


Figure 10. Example of positive and negative Skewness [17].

Kurtosis, Sku

The Sku parameter is a measure of the sharpness of the surface height distribution and is the ratio of the mean of the fourth power of the height values and the fourth power of Sq within the sampling area.

$$Sku = \frac{1}{Sq^4} \frac{1}{A} \iint_A z^4(x, y) dx dy$$

Kurtosis is strictly positive and unit-less and characterizes the spread of the height distribution. A surface with a Gaussian height distribution has a kurtosis value of three. Unlike Ssk , use of this parameter not only detects whether the profile spikes are evenly distributed but also provides a measure of the spikiness of the area. A spiky surface will have a high kurtosis value and a bumpy surface will have a low kurtosis value. The Ssk and Sku parameters can be less mathematically stable than

other parameters since they use high order powers in their equations, leading to faster error propagation [16][17].

Figure 11 shows an example of Kurtosis higher and lower than 3:

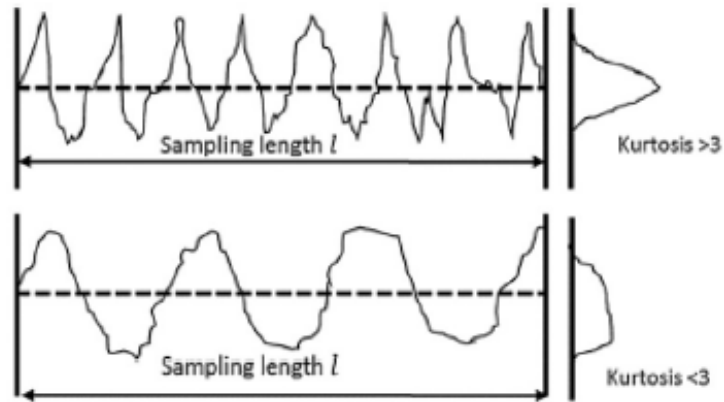


Figure 11. Example of Kurtosis >3 and <3 [17].

Maximum peak height, S_p

The S_p parameter represents the maximum peak height, that is to say the height of the highest point of the surface. As heights are counted from the mean plane and are signed, S_p is always positive [16].

Maximum valley height, S_v

The S_v parameter represents the maximum valley height, i.e. the height of the lowest point of the surface. As heights are counted from the mean plane and are signed, S_v is always negative [16].

Maximum height of the surface, S_z

The S_z parameter is the maximum height of the surface, i.e. is sum of the absolute values of S_p and S_v .

$$S_z = S_p - |S_v| = S_p + S_v$$

The maximum height parameters are to be used with caution as they are sensitive to isolated peaks and pits which may not be significant [16].

2.2.2 Spatial/spacing parameters

A surface is called isotropic when its features are independent from the direction along which are measured. Unfortunately, it is tough to get this random texture when the surface is machined because machining processes usually leave a periodic mark on the face. Anisotropy is investigated by means of techniques like the Fourier transform and autocorrelation function-based comparison.

Autocorrelation length, Sal

Sal, the Auto-Correlation Length, is a measure of the distance over the surface such that the new location will have minimal correlation with the original location. The direction over the surface chosen to find Sal is the direction which yields the lowest Sal value. The autocorrelation length, Sal, is defined as the horizontal distance of the autocorrelation function ACF (tx, ty) which has the fastest decay to a specified value s, with $0 < s < 1$. The Sal parameter is given by:

$$Sal = \min \sqrt{tx^2 + ty^2}$$

Figure 12 shows the autocorrelation of a textured surface. The white part on the central lobe is above the threshold s [16].

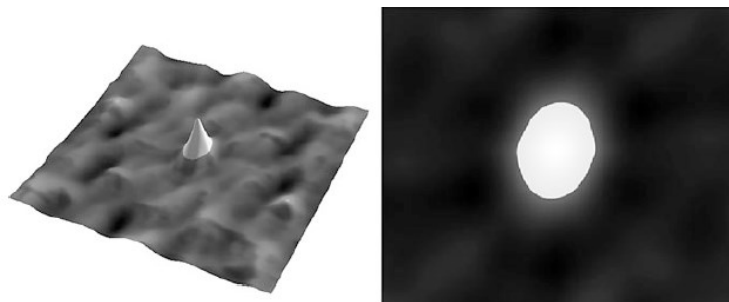


Figure 12. Autocorrelation peak with applied threshold of 0.2 (white part above the threshold) [16].

A radius is calculated from the center to the perimeter of the lobe and the shortest radius is kept for Sal. For all practical applications involving relatively smooth surfaces, the value for s can be taken as 0.2, although other values can be used and will be subject to forthcoming areal specification standards. A large value of Sal

denotes that that surface is dominated by low spatial frequency components, while a small value for Sal denotes the opposite case. The Sal parameter is a quantitative measure of the distance along the surface by which a texture that is statistically different from the one at the original location would be found. The contour of the central lobe is measured from the center and the shortest radius is identified. This radius gives the value of the Sal parameter, as shown in Figure 13 [16].

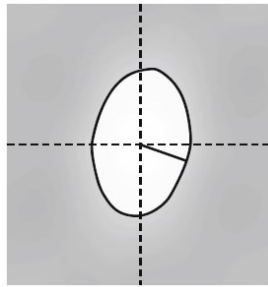


Figure 13. Shortest radius measured from the centre to the contour of the thresholded lobe on the autocorrelation plot [16].

Texture aspect ratio, Str

Str, the Texture Aspect Ratio, is an indicator of the spatial isotropy or directionality of the surface texture. The Str parameter is unit-less and its values lies between 0 and 1. It can also be expressed as a percentage between 0 and 100%. For a surface with a dominant lay, the Str parameter will tend towards zero, whereas a spatially isotropic texture (i.e. having the same properties regardless of the direction) will result in a Str of one. The texture aspect ratio parameter, Str is one of the most important parameters when characterizing a surface in an areal manner as it characterizes the isotropy of the surface texture. Str can be expressed as the ratio between the length of fastest decay of ACF in any direction and the length of slowest decay ACF in any direction.

$$Str = \frac{r_{\min}}{r_{\max}}$$

While the Sal parameter is calculated from the minimum radius on the central lobe of the ACF, the Str parameter is calculated from the minimum, r_{\min} , and maximum

radii, r_{max} , found under the same conditions, on the autocorrelation plot after applying a threshold of 0.2, as shown in Figure 14 [16].

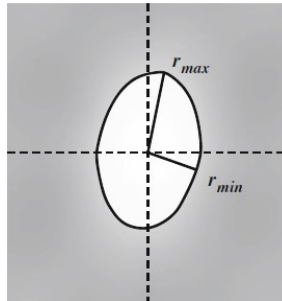


Figure 14. Minimum and maximum radii measured on the central lobe of the autocorrelation plot [16].

On an isotropic surface it is far more significant an assessment of the surface texture using a 2D (profile) surface texture measuring instrument (faster, simpler, cheaper) than on a surface presenting a low Str. As mentioned above, if Str is close to 0, then the surface is anisotropic, i.e. it has a dominant texture direction. In this case, the parameter Std will give the direction of the texture.

Texture direction, Std

The texture direction parameter, Std, is assessed from the Fourier spectrum of the surface. Moving from the centre to an edge of the spectrum in a given direction, the spatial frequencies go from the lowest to the highest value. The frequency at the centre corresponds to the continuous value in z (frequency of zero or infinite wavelength). When the surface is centred, this offset is zero. Frequency amplitudes along the radius at a given direction "h" can be integrated between two selected spatial frequencies, f_{min} and f_{max} , in order to calculate a value $A(\theta)$ that represents the spatial frequency content in that direction. By repeating this integration for all angles between 0° and 180° , a polar spectrum is obtained that can be represented with a semi-circular graph, Figure 15. The maximum value of the graph is called the main texture direction, or Std. The Std parameter is given in degrees 0° and 180° and should be considered as insignificant if the isotropy factor Str is below 0.6 and 0.8

(depending on the application). The definition of Std specifies that the angle can be given from a reference angle s . The Std parameter is a convenient parameter on surfaces showing scratches and oriented texture [16].

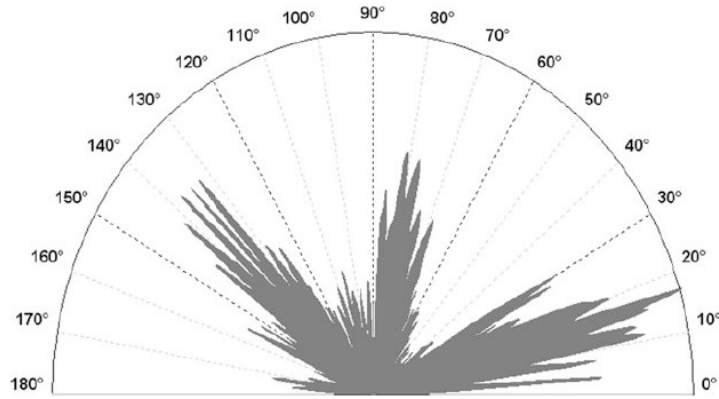


Figure 15. Polar spectrum graph representing the texture directions [16].

2.2.3 Hybrid parameters

Hybrid parameters are nothing, but a combination of height and spatial parameters. Considerable properties are the capability to detect surfaces slope and curvature, they are rated to be useful for tribological evaluation of the surfaces.

Root mean square gradient, Sdq

Sdq is the root mean square (RMS) surface slope including the surface, evaluated over all directions. The root mean square gradient is then calculated on the whole surface where A is the projected area of the surface.

$$Sdq = \sqrt{\frac{1}{A} \iint_A \left(\frac{\partial z^2}{\partial x} + \frac{\partial z^2}{\partial y} \right) dx dy}$$

Sdq is a general measurement of the slopes which comprise the surface and may be used to differentiate surfaces with similar average roughness, Sa . Sdq is affected both by texture amplitude and spacing. Thus, for a given Sa , a wider spaced texture may indicate a lower Sdq value than a surface with the same Sa but finer spaced features. The Sdq parameter has a unit-less positive value [16].

2.3 Process parameters

In the manufacturing process, there are two main reasons that influence the surface roughness of the workpiece. The first one due to the cutting of the residual area from the relative motion of the tool and of the workpiece. The other reason is related to the property of the material and the principle of the cut as plastic deformation, friction, build up edge (BUE) and vibrations of the process system and so on in the cutting process. In particular, the first reason relating to the movement between the tool and the workpiece is related to processing parameters such as cutting speed, feed rate, axial depth of cut, radial cutting immersion and so on. In order to optimize the various parameters to improve the quality of the mould, much research has been conducted on this topic. In the following are recorded some studies that make up the current state of the art regarding the characterization of the surface quality of pieces machined by conventional milling and micro-milling.

S.N.B. Oliaei et Al. [18] investigated the influence of process input parameters such as cutting speed, depth of cut, feed per tooth, radial immersion percentage, and plunging method on process outputs during circular pocketing operation which allows conducting uninterrupted micro milling experiments with longer tool path compared to slot milling operation, Figure 16. Tool wear, machining forces and surface roughness measurements were considered to identify the relationships between process inputs and outputs.

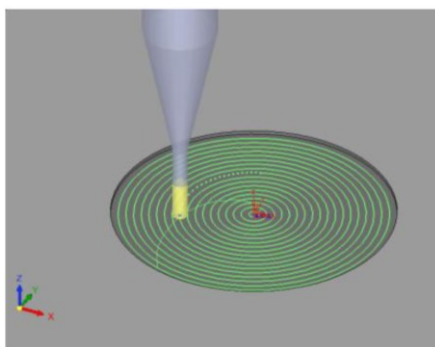


Figure 16. CAM simulation of circular pocket milling operation [18].

The tool used in this study was micro end mill (NS tools, 2 teeth, 30° helix angle) having diameter of 0.8 mm and the workpiece was Stavax ESR. Cutting speed ($N=15000$ rpm) and depth of cut ($a_p=0.16$ mm) were fixed, while feed rate (0.5, 2, 4, 6 μm) and radial immersion (20, 60, 80 %) was varied and areal topography surface roughness was measured.

Surface roughness is the most important process output yet the most difficult to analyze in micro scale. In the current research, a contactless method of surface roughness measurement method was used to analyze the machined surfaces. In Figure 17 it is shown an acquisition of a machined surface.

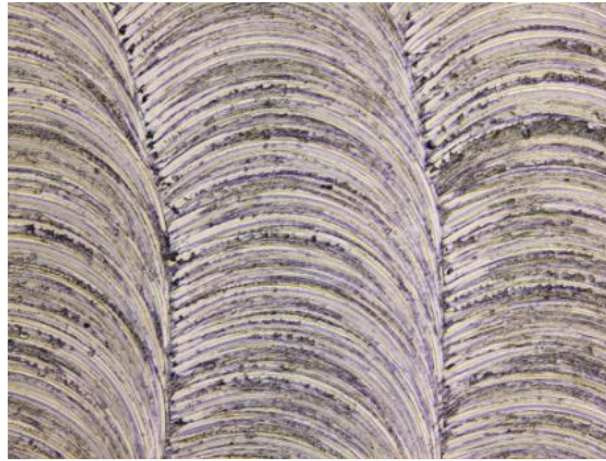


Figure 17. Surface of micro milled circular pocket [18].

It is observed that low radial immersion experiments yield low surface roughness than high radial immersion tests. At high radial immersion, increasing feed yields better surface roughness. Based on measurements, 20% radial immersion and 4 $\mu\text{m}/\text{tooth}$ feed combination gave the best areal surface, Figure 18, while small and discontinuous type of chips formed at very low feeds is shown to have an adverse effect on surface roughness measurements.

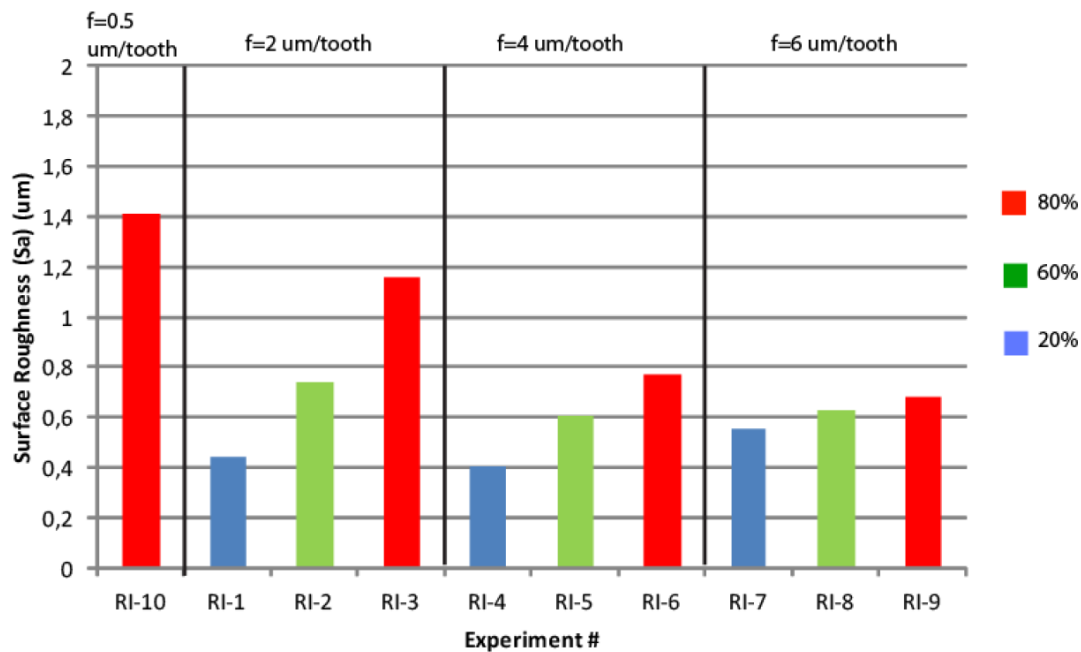


Figure 18. Surface roughness as a function of experimental conditions [18].

K.S.Neo et Al. [19] explored the feasibility of using PCBN tools for direct ultra-precision machining of Stavax, a type of alloy steel from ASSAB. The performance characteristics in terms of surface roughness of an ultra-precision machine using tool in PCBN (99% of cubic boron nitride or CBN) and conventional CBN (85-90% of CBN and cobalt as binder) under different machining conditions were studied and their results were compared. The parameters considered are rotational cutting speed, feed rate, depth of cut and tool materials. At one time, one parameter was varied and while others were fixed.

The surface roughness of the workpieces machined by both the PCBN and CBN tools exhibit similar decreasing trend with increase in the rotational cutting speed. However, at higher cutting speed, the PCBN tool can give better surface finish compared to the CBN tool.

For both the PCBN and CBN tools, as the depth of cut is increased, there is a highly correlated increase in surface roughness. When the depth of cut is increased, there is a corresponding increase in cutting forces with result in increased self-excited

vibration and accelerated tool wear. Both these factors are responsible for the increase in surface roughness.

Surface roughness increases rapidly for high feed rates for both PCBN and CBN cutting tools. To maintain a low value of surface roughness, the feed rate should be kept low. In Figure 19, all the graphs are shown the graphs for each of the related factors are shown.

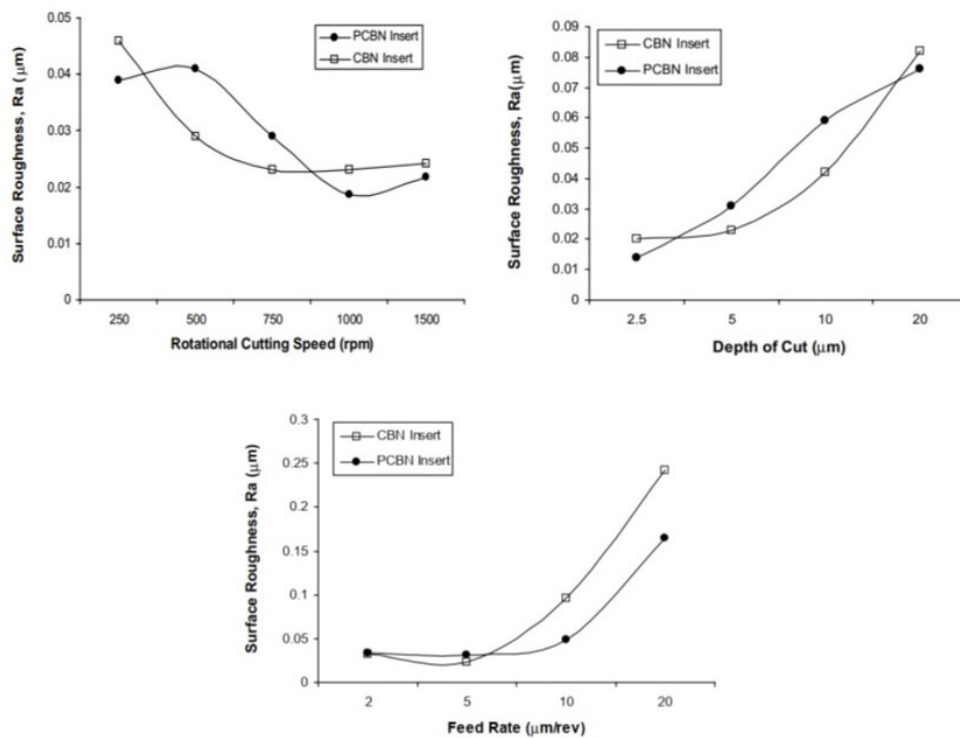


Figure 19. Surface roughness as function of (a) rotational cutting speed, (b) depth of cut, (c) feed rate [19].

D. Li et Al. [20][21] discusses a new micro milling strategy for manufacturing microstructured surfaces with optical function on steel. These microstructures, a combination of arrays of micro-ridges, has been developed to maximize the contrast of the reflected light from orthogonally patterned features. The burr formation and insufficient material removal, influenced by the tool wear and the machine accuracy, were the main challenges in this process. In a first research, it has been studied the impact of different cutting parameters, i.e. different tool diameters, the rotational

cutting speed, the cooling condition and the feed rate by machining a workpiece in Orvar Supreme (Uddeholm), with hardness of 48-50 HRC. The contrast values are used as the response of the DoE to evaluate the influence of the parameters on the functionality of the surfaces. The conclusion was that the cooling condition and the feed rate affected the contrast significantly: “oil+air” and higher feed rate were preferred since the optical functionality was linearly decreasing with the burr height. In the following work, the cutting strategy was investigated in order to reduce the burr formation during the process. An explanation of the two strategies is reported in Figure 20:

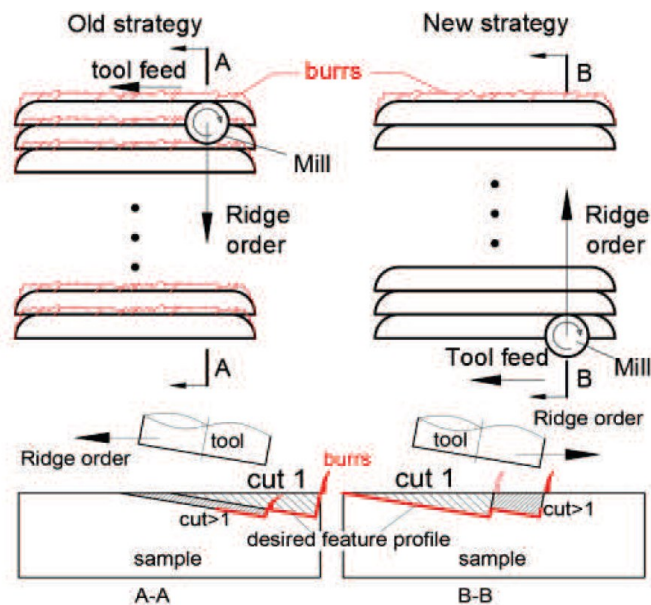


Figure 20. (a) the old strategy, (b) the new strategy [21].

Figure 21(a) shows lot of burrs left on the features produced by the old strategy. Figure 21(b) shows no burrs were left on the features by new machining strategy. Further measurements proved that no burrs formed even after machining 1000 pixels. As expected, the burrs were only observed on the last ridge of each pixel.

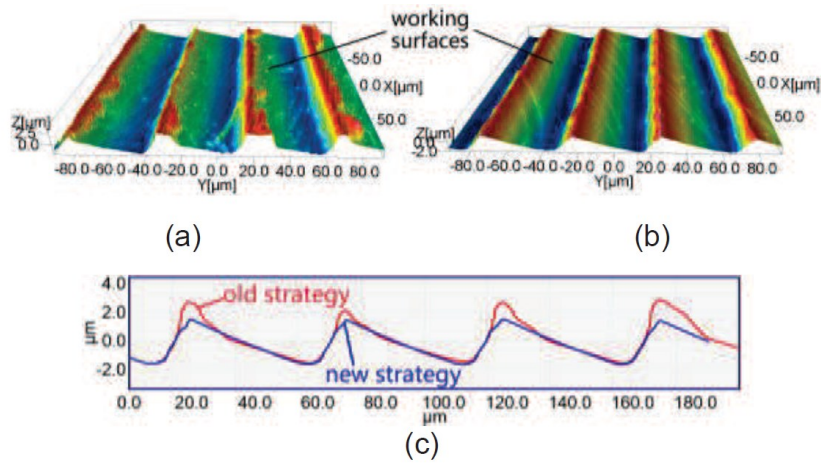


Figure 21. The comparison of the geometries of (a) features by old strategy and (b) features by new strategy, (c) the comparison of the average profiles [21].

Surface roughness increases during cutting over 1000 pixels. The roughness was relatively stable among the first 400 pixels and fluctuations emerged after that. The trend can be associated with the tool wear, which will be verified by further tool wear tests. A graph of this phenomenon is reported in Figure 22:

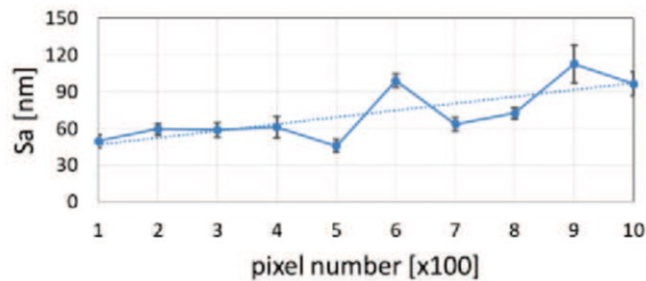


Figure 22. Surface roughness as a function of pixel number [21].

Xuefeng et Al. [22] studied the relationship between the process parameters and surface roughness. The type of workpiece is Cr12MoV die steel, while two different tools is used during the experiments. The flat mill is a diamond integrated carbide flat end mill, with a diameter of 10 mm, 4 flutes, the ball mill is a ball end vertical mill, with a diameter of 6 mm and 2 flutes. The aim of the study is to analyse which are the main parameters affecting the surface roughness, i.e. spindle speed, feed rate, axial depth of cut and radial depth of cut.

For both cases, the bigger spindle speed is, the smaller surface roughness is and also the smaller the feed rate, the smaller the roughness. Instead, both the axial depth of cut and the radial depth of cut generates small changes in surface roughness by changing their values. Figures 23 and 24 show the impact of each factor under test on surface roughness:

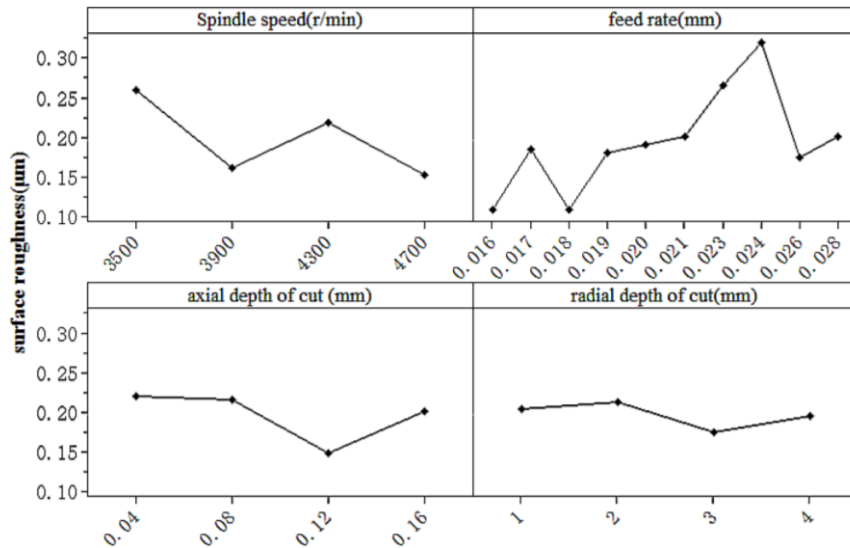


Figure 23. Surface roughness as a function of different cutting parameters using a flat end mill [22].

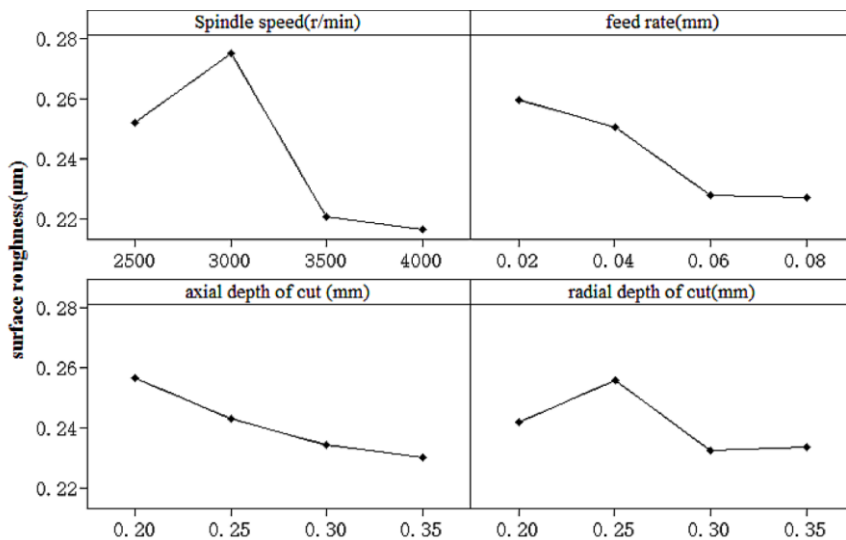


Figure 24. Surface roughness as a function of different cutting parameters using a ball end mill [22].

The three-dimensional surface topography of the plane machined by the flat end mill is shown in Figure 25(a), while the surface machined by a ball-end mill is shown in Figure 25(b).

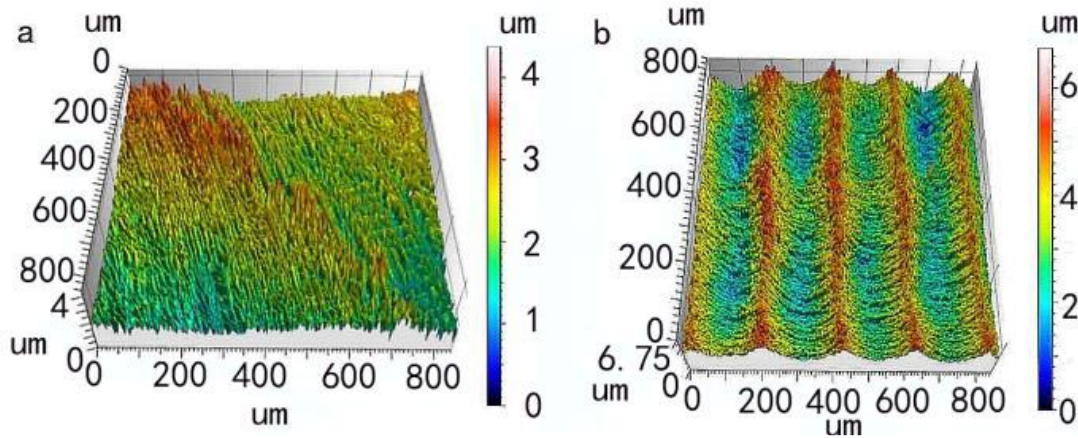


Figure 25. 3D topography of machined surface using (a) a flat end mill, (b) a ball end mill [22].

The effect of milling parameters on surface integrity in high speed milling of ultrahigh strength steel is studied by Zhenchao et Al. [23]. The results show that the influence of milling speed and feed per tooth on two-dimensional (in x and y directions) and three-dimensional surface roughness (mean, RMS and maximum peak height) is significant, but the milling depth of cut has little effect. Workpiece material used in the experiments is 16Co14Ni10Cr2Mo steel. In Figures 26, 27, 28, it is shown the impact of different cutting parameters on 2D and 3D surface roughness:

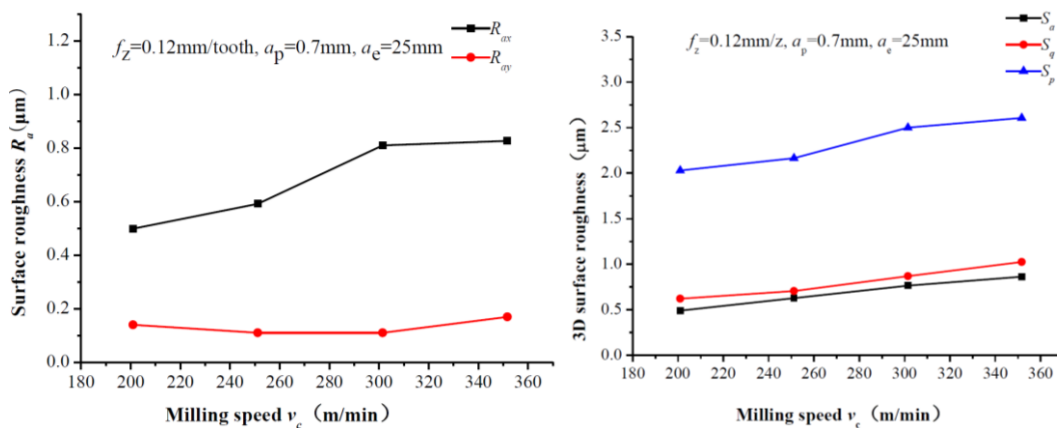


Figure 26. Effect of milling speed on (a) 2D surface roughness and (b) 3D surface roughness [23].

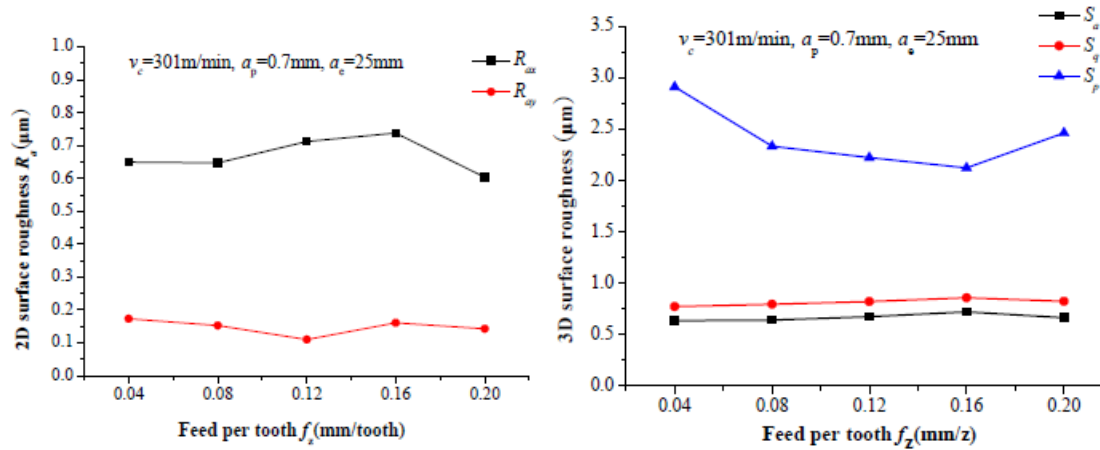


Figure 27. Effect of feed per tooth on (a) 2D surface roughness and (b) 3D surface roughness [23].

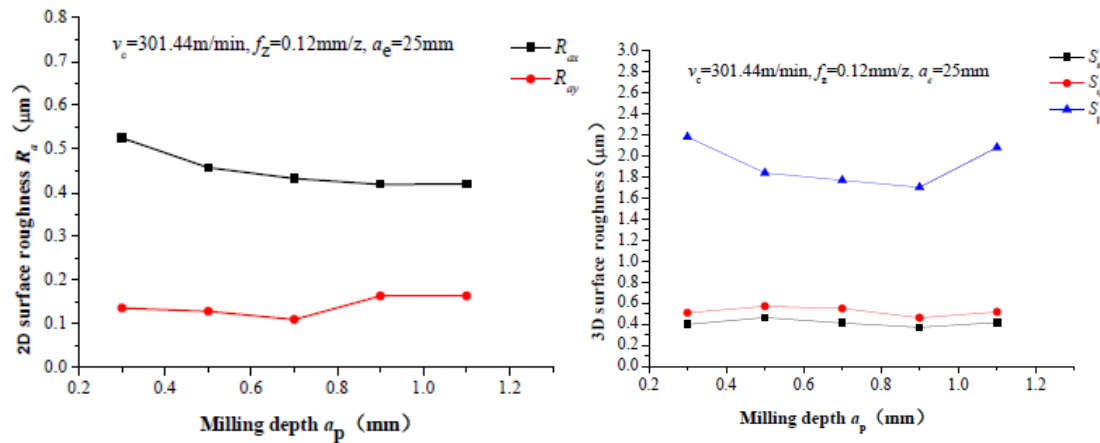


Figure 28. Effect of depth of cut on (a) 2D surface roughness and (b) 3D surface roughness [23].

From the graphs, it is possible to conclude that the 2D surface roughness increases with milling speed and feed per tooth, but decreases with milling depth; the maximum peak value S_p decreases with all milling parameters, but 3D arithmetical mean deviation of the profile S_a and 3D RMS height value S_q have no evident changes with milling parameters.

Felho et Al. [24] studied the influence of feed per tooth on the calculated theoretical and the real measured surface roughness of a machined surface, considering different insert shapes. The material used as a sample is 42CrMo4 alloyed heat

treated steel. Tests, keeping constant some cutting parameters, i.e. cutting speed, depth of cut and radial engagement of the tool, were carried out changing the values of feed per tooth and the shape of the inserts. In Figure 29, a picture of a theoretical surface machined with three different inserts is shown:

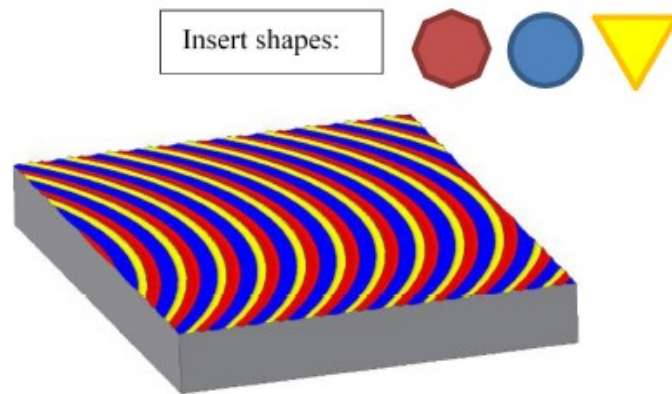


Figure 29. Theoretical surface with three different inserts [24].

The theoretical and measured results demonstrate a similarity, just as can be seen from the comparison between the extracted profiles in Figure 30; from the study made, an increase of the surface roughness value is highlighted to the increase of the feed per tooth, that therefore turns out to be a significant factor. In Figure 31, the theoretical and measured roughness trend is shown as a function of progress.

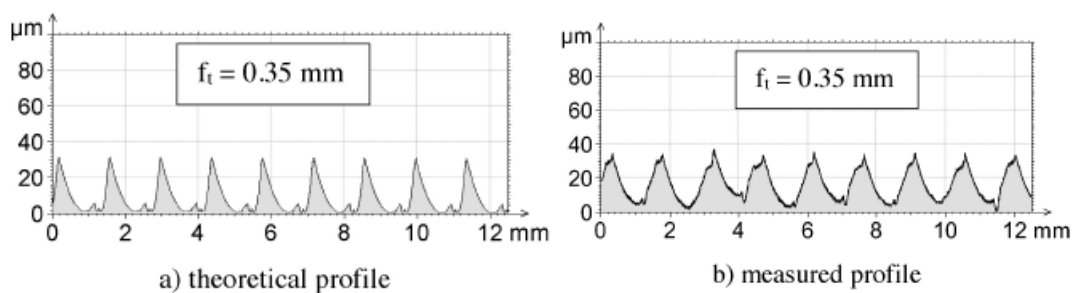


Figure 30. (a) theoretical and (b) measured profile at constant feed per tooth [24].

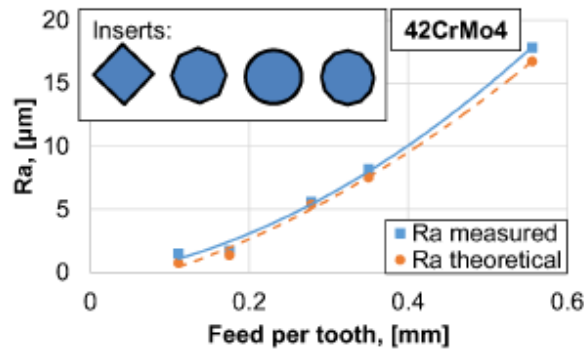


Figure 31. Theoretical and measured surface roughness as a function of feed per tooth [24].

2.4 Techniques for machining optical moulds

2.4.1 Diamond engraving

These mould inserts were manufactured for Bradford university by the precision optics laboratory of Durham University Centre for advance instrumentation [25]. The inserts were made of amorphous aluminum and were diamond engraved to produce a regular structure. Amorphous aluminum was selected because of its diamond machining characteristics, amorphous aluminum machines well and does not have a grain structure so very high-quality surface can be achieved.

The sample presents three different zones, the inner one presents a groove density of 200 lines/mm, while the others present a density of 30 and 100 lines/mm. In Figures 32 and 33 are reported a drawing of the insert and a picture of the machined insert:

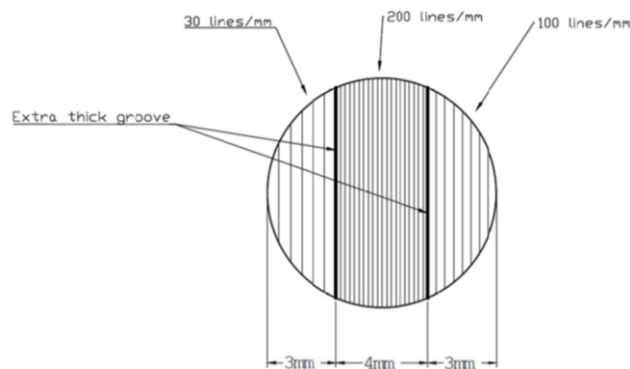


Figure 32. Drawing of the mould insert [25].



Figure 33. Machined mould insert [25].

Figure 34 shows the diamond engraved insert at 200, 100 and 30 lines/mm:

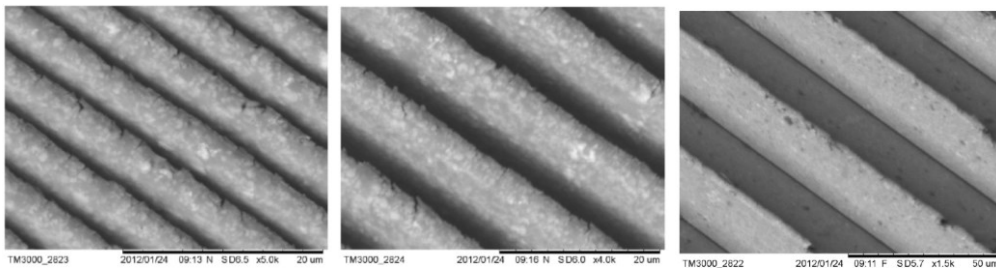


Figure 34. Diamond engraved mould insert (a) 200 lines/mm, (b) 100 lines/mm, (c) 30 lines/mm, magnification x1500 [25].

Before choosing this method of fabrication several other engraving techniques were investigated, including photolithography and direct laser engraving. These techniques have potential but are considerably more expensive to use than diamond engraving for small production runs.

Chabum Lee et Al. [26] fabricated a mould for polymer based by diamond engraving on the electroless Ni-coated surface on Stavax steel.

The feasibility of an engraving process with a rectangular formed diamond tool is studied. Cutting depths of about 0.2 μm on the flat metal surface is quite difficult because the tool wear caused by stress concentration is severe and the size of a diamond tool in dimensions is much bigger than that of the cutting area. Furthermore, while fabricating the blazed gratings, it is of importance to keep the blazed facets smooth and the edges sharp. Micro fracturing, such as potential micro cracks and dislocations on the substrate, is a key problem in micro optics machining.

In order to provide tool wear-free, spring-back effect-free and a small period of the blazed gratings, a diamond tool is inserted with a larger depth of cut along the thrust direction. The cutting processes repeat the first tool path, the second tool path, the third tool path, until the last tool path in order along the cutting direction while the diamond tool moves of one step along the feed direction. In Figure 35, it is shown the scheme of the cutting process:

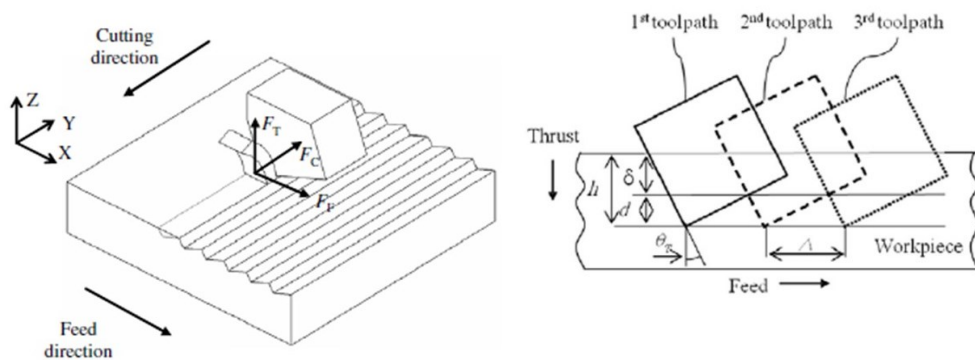


Figure 35. (a) scheme of tool path cutting operation, (b) detail of cutting operation [26].

Under the machining conditions, the blazed gratings with a step of $2.0 \mu\text{m}$ and a depth of $0.2 \mu\text{m}$ were successfully fabricated on the electroless Ni-coated surface. The electroless Ni is a well-known material for diamond-based machining. The atomic microscope photograph, Figure 36, shows a sharp edge and a regular machined surface required for high performance optical applications.

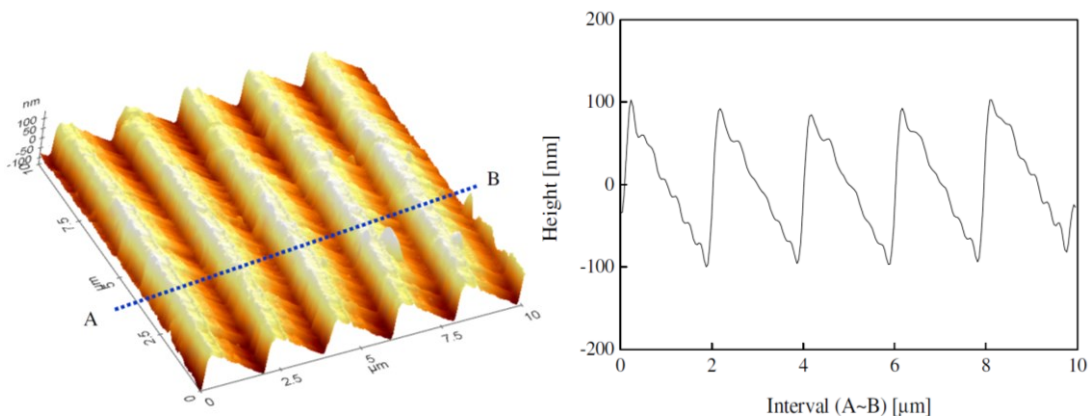


Figure 36. (a) atomic microscope image of machined surface, (b) an extracted profile [26].

2.4.2 Diamond turning

As another fabricating method, ultra-precision diamond turning has been successfully used in the fabrication of microstructures on nonferrous material with high form accuracy and surface finish quality. Before machining, the workpiece is reacted with nitrogen to avoid chemical reactions between the iron in the workpiece and the carbon in the diamond tool by modifying the chemical composition of the workpiece subsurface; as a result, diamond tool wear was reduced.

For the current work done by Wang et Al. [27], nitrided AISI 4140 die steel specimens with a diameter of 50 mm and thickness of 5 mm were used in the experiment. Single crystal diamond tool with the same crystal orientation but different geometries were used in the preliminary cutting test and Fresnel microstructure machining. For the preliminary cutting test, a round-shaped diamond tool was used, while for the Fresnel microstructure machining, a V-shaped diamond tool was used. The cutting experiments were carried out on a two axis ultra-precision lathe. Figure 37 shows a picture of the experimental setup:

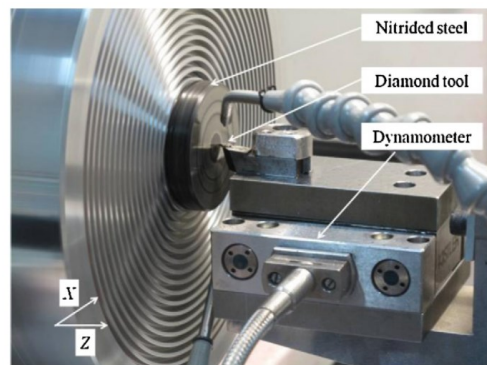


Figure 37. Diamond turning machining setup [27].

Preliminary cutting test was carried out to verify and estimate the effect of plasma nitriding treatment with rare earth addition on the tool wear before the Fresnel microstructure machining. Figure 38 shows a SEM photograph of the Fresnel microstructure generated by the proposed machining method. It is evident that the Fresnel annulus was generated sequentially to form a Fresnel microstructure on the

nitrided specimen. The annulus as well as the zone step can be identified clearly as concentric rings with no defects.

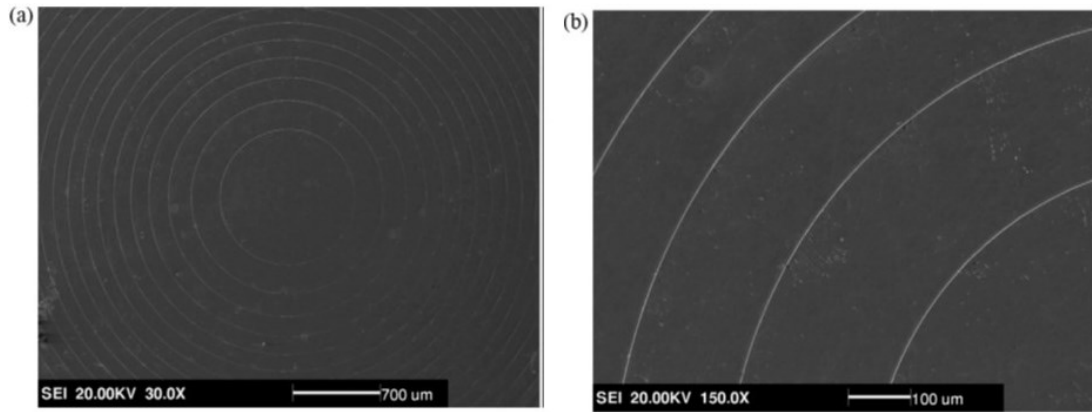


Figure 38. SEM photographs of the Fresnel microstructure: (a) general view and (b) detailed view [27].

Figure 39(a) and (b) shows the interferometer images of a part of the Fresnel microstructure. The annulus as well as the zone step could be fabricated precisely. Figure 39(c) shows the cross-sectional profile of the diamond-turned Fresnel microstructure. It is evident that the machined microgrooves are almost uniform and that no visible roundness or microfracture occurred at the corner or the edge of the microgroove, although some random submicron-scale defects were observed.

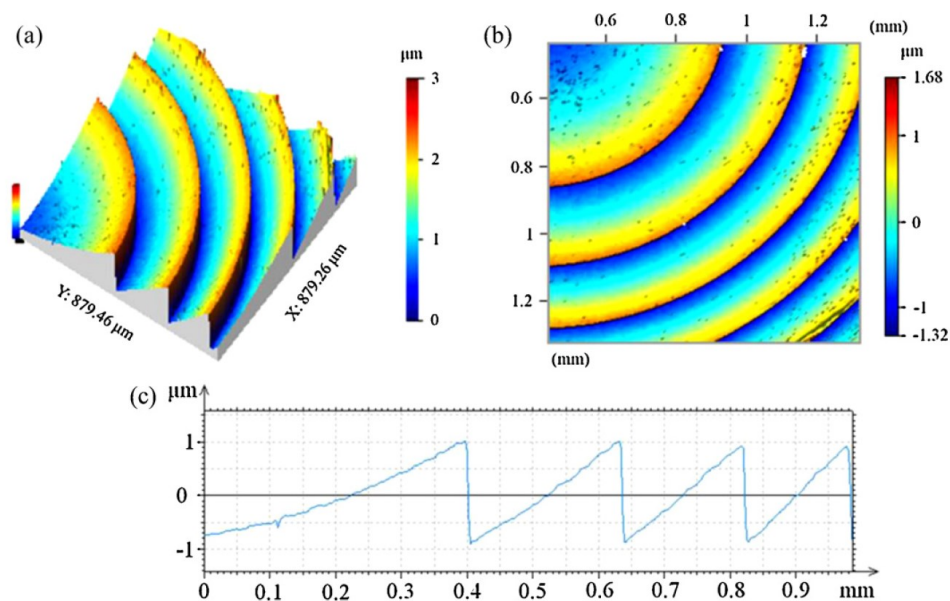


Figure 39. Measurement results of the Fresnel microstructure: (a) 3D interferometer image, (b) 2D interferometer image, and (c) 2D cross-sectional profile [27].

Holthusen et Al. [28] investigate the replicability of diamond turned blaze gratings for injection moulding. Testing different optical polymers.

For the experiments, the material of the specimens was CuNi8Zn42Pb4Mn1, while a single crystal diamond tool with wedge-shaped geometry in the cutting test. For the assessment of the replication process, continuous blaze structures without height modulation were diamond turned on an ultra-precision machine.

In Figure 40(a) and (b) the mould insert and the surface topography of the blaze structure are shown. A white light interferometer was used to measure and evaluate the geometry of the blaze structure, which will be compared with the moulded surfaces using different polymers, Figure 40(c) and 41.

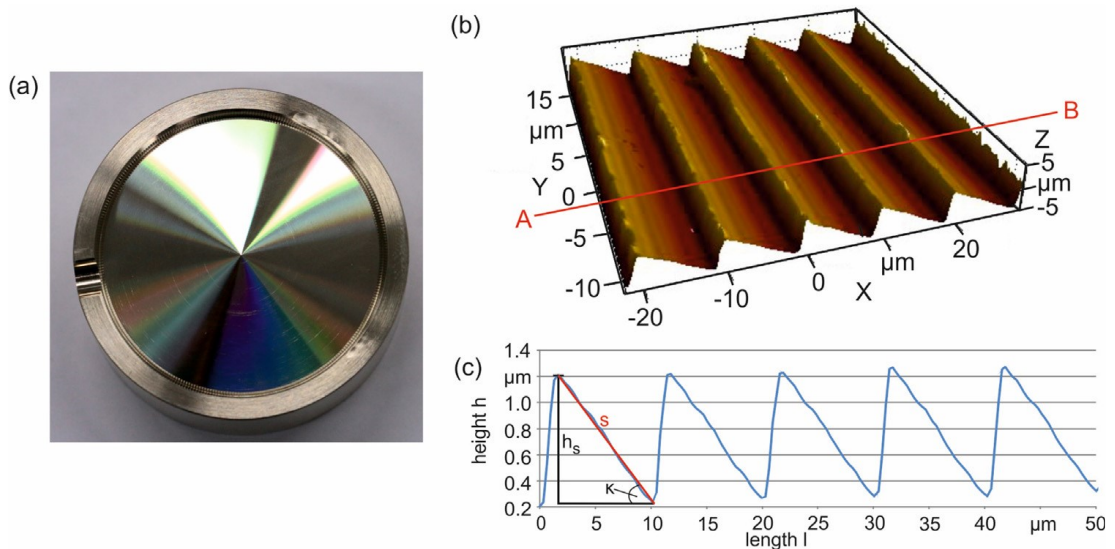


Figure 40. (a) diamond turned mould insert, (b) surface topography measured with a white light interferometer and (c) extracted surface profile A-B [28].

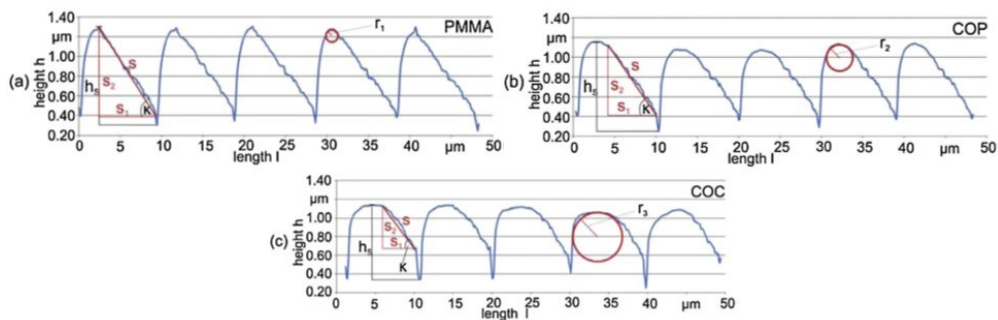


Figure 41. Surface profile of the injection moulded (a) PMMA surface, (b) COC surface, (c) COP surface [28].

3. AIMS OF THE WORK

The aim of this research work is to study and then apply micromilling technology to recreate regular optical profiles on mould materials. The idea is to study in depth, through various experiments, the mechanism of generation of this regular texture on the surface of the material under examination and understand the influence of different factors on it, to obtain a strategy to process specimens that will then be used to machine inserts for injection moulding.

Two case studies were addressed during this work.

3.1 Case study 1: machining of Stavax ESR steel

The first research is conducted in collaboration with the University of Bradford. A low-cost inspection system for microneedle patches was required. These microneedles are used in the biomedical field, they are replicated on patches in order to be applied to the patient's skin to administer the right amount of drug for the cure. For this reason, it is essential that the moulding of these microneedles is successfully filled. The goal of this project requires machining of diffractive (preferably blazed) gratings on mould surfaces, placed at the backside of the part, using Stavax ESR steel. In Figure 42 is reported a conceptual drawing of the moulded parts containing the microneedles and the diffraction area on the back:

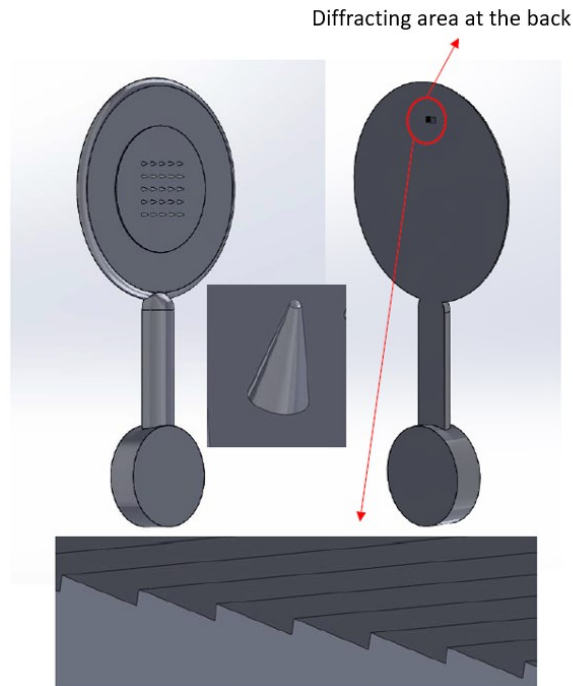


Figure 42. Drawing of the moulded part containing the microneedles.

The diffractive area should be at least around 10-15 mm² (4 mm x 4 mm) because of the laser spot size that is used for monitoring. The idea is that if the grating replicates well, most probably the needles will be filled too. Thus, the quality of the grating (or the intensity of the first order diffraction) will tell that the needle is filling. This strategy has the goal to avoid checking the quality of each needle with a direct investigation method, i.e. looking all the needle with a microscope, that should be a very time-consuming method, but allows a quick inspection, through the use of a laser light that is diffracted by the texture generated on the back of the patch.

To do this, various experiments, varying different cutting factors and tools, will be carried out in order to better understand the mechanism of cutting and generating a regular diffraction grating on the material. Once this is done, the objective will be to process three inserts for injection moulding using the optimal parameters obtained from the various cutting tests. In Figure 43 is reported a drawing of the insert that will be machined:

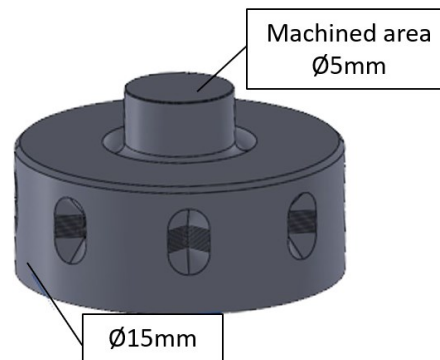


Figure 43. Insert for injection moulding to be machined.

3.2 Case study 2: machining of NiP coating

The second research is in collaboration with the University of Padua. Automotive lighting market increasingly required three-dimensional mould micro features, such as micro grooves, micro lenses and micro prisms, with polished surfaces. In particular, retroreflectors (RRs) are optical devices made of transparent plastics and normally utilized in automotive lighting devices to return incoming light and to make the vehicle visible while driving in low light conditions. Their functionality is based on the inverted corner cube (ICC) geometry. This particular geometry enables the incident light to be retroreflected after three internal consecutive reflections, according to the optical principle called total internal reflection (TIR). In Figure 44, a drawing of the mould and the reflex insert for injection moulding of the RRs:

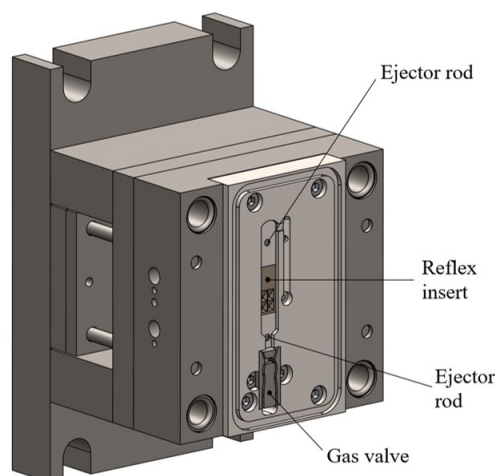


Figure 44. Drawing of the mould and the reflex insert for injection moulding of the RRs.

Therefore, micromilling of electroless-plated NiP is a viable manufacturing option for the fabrication of moulds for RRs: cutting parameters effects on mould surface topography were experimentally characterized and optimized. Moreover, the mould surface texture was replicated by injection moulding on polycarbonate RRs and its effects on their retroreflective performance was characterized.

In the current study, it is requested to continue the research work already started previously, deepening the study of micro-milling on NiP coating.

The aim of this research will be to understand the mechanism of generating regular saw-tooth surfaces obtained using a flat end mill and to compare them with those obtained previously from a ball end mill, used for machining the RRs. Through various experiments, it will be possible to understand the influence of different factors on the quality and on the regularity of the profiles obtained. The goal will be to optimize the various parameters to recreate the best regular saw-tooth surfaces in order to replicate them on the injection moulding insert and finally observe the optical quality of the moulded sample.

4. MATERIALS AND METHOD

4.1 Used materials

4.1.1 Uddeholm Stavax ESR steel (Case study 1)

Uddeholm Stavax ESR is a premium stainless mould steel for small and medium inserts and cores. It combines corrosion and wear resistance with excellent polishability, good machinability and stability in hardening. Stavax ESR is mainly used to produce moulds and dies. The presence of chromium in the material confers high corrosion resistance in presence of water, chlorides and organic substances, that are usually dangerous for carbon steels and in some cases also for austenitic stainless steel. After the hardening heat treatment, the high achieved surface hardness is 56 HRC.

Chemical composition

The chemical composition of this material is shown in the table below, Table 1:

Chemical composition of Stavax ESR steel (%)				
Carbon	Chromium	Silicon	Vanadium	Manganese
0.38	13.6	0.9	0.3	0.5

Table 1. Chemical composition of Stavax ESR steel.

General properties

Uddeholm Stavax ESR is a premium grade stainless tool steel with the following properties:

- good corrosion resistance
- excellent polishability
- good wear resistance
- good machinability
- good stability in hardening

The combination of these properties gives a steel with outstanding production performance. The practical benefits of good corrosion resistance in a plastics mould can be summarized as follows:

- Lower mould maintenance costs: the surfaces of the moulds retain their original finish over extended running periods; moulds stored or operated in humid conditions require no special protection.
- Lower production costs: since water cooling channels are unaffected by corrosion (unlike conventional mould steel), heat transfer characteristics, and therefore cooling efficiency, are constant throughout the mould life, ensuring consistent cycle times.

These benefits, coupled with the high wear resistance of the material, offer low-maintenance, long-life moulds for the overall moulding economy.

Applications

Uddeholm Stavax ESR is recommended for all types of moulding tools and its special properties make it particularly suitable for moulds with the following demands:

- Corrosion resistance, i.e. for moulding of corrosive materials and for moulds subjected to humid working/storage conditions.
- Wear resistance, i.e. for moulding abrasive materials. Uddeholm Stavax ESR is recommended for moulds with long production runs.

-
- High surface finish, i.e. for the production of optical parts, such as camera and sunglasses lenses, and for medical containers, e.g. syringes, analysis phials.

4.1.2 H13 steel (Case study 1)

H13 tool steel is a versatile chromium-molybdenum hot work steel. It combines good hardness and abrasion resistance with the ability to resist heat checking. It is an AISI H13 hot work tool steel, the most widely used steel for aluminum and zinc die casting dies. It is also widely used for extrusion press tooling because of its ability to withstand drastic cooling from high operating temperatures.

Chemical composition

The chemical composition of this material is shown in the Table 2:

Chemical composition of H13 steel (%)							
C	Cr	Mn	Mo	P	Si	S	V
0.32-0.45	4.75-5.5	0.2-0.5	1.1-1.8	0.03	0.8-1.2	0.03	0.8-1.2

Table 2. Chemical composition of H13 steel.

General properties

H13 steel is a chromium-molybdenum steel that presents the following properties:

- Uniform and high level of machinability and Polishability
- Good high temperature strength and resistance
- Excellent through hardening properties
- Good resistance to abrasion at both low and high temperatures

Applications

- Inserts
- Cores
- Cavities for die casting dies

-
- Hot forging dies
 - Extrusion dies
 - Plastic mould cavities
 - Components that require high toughness and excellent polishability.

4.1.3 Electroless-plated NiP steel (Case study 2)

NiP electroless-plating is a kind of coating that consists on covering the surface of a material, such as steel, with an amorphous alloy of Nickel (Ni) and Phosphorous (P) to confer protection against corrosion and wear. Generally, the deposit can have a thickness lower than 500 μm .

The considered coating, used in this research, presents a phosphorous content of around 10% and this amorphous layer has a hardness of around 49-55 HRC.

General properties

NiP electroless-plating presents the following properties:

- Good mechanical properties
- High wear resistance
- High corrosion resistance
- Favourable tribological properties

Applications

- Protective and functional coatings for automotive, aerospace and general engineering industries
- Decorative coatings for automotive industry
- Fabrication of high precision components

4.2 Manufacturing systems

4.2.1 Kern EVO 5-axis CNC machining centre

The MI_crolab laboratory of the Politecnico di Milano owns the Kern EVO 5-axis CNC machining centre, Figure 45, on which all the cutting operations have been performed.



Figure 45. Kern EVO 5-axis CNC machining centre.

The X, Y and Z axes are used for movements in the plan, while the machine is also equipped with two axes B and C which constitute two additional degrees of freedom of rotation. The machine is manufactured by the German manufacturer Kern for use in precision machining and is therefore used for all research in the field of the micro-milling that the laboratory is supporting. The main feature that distinguishes a machine like this from a traditional machining centre is the higher spindle rotation speed (N) reachable equal to 50000 rpm. This property of the machine is fundamental to be able to work with micro-tools, because the speed of the spindle is linked to the cutting speed parameter that must be high enough to permit the cutting of the

material. It is equipped with the numerical control Heidenhain iTNC 530. The data sheet of the Kern EVO is reported in the Appendix B.

4.3 Tool selection

Here is a list of 3 tools, the first two were used for the tests on mould steel, while the last one was used for various tests on NiP coating.

4.3.1 Mitsubishi D015MS2SS0

- Tool from Mitsubishi;
- Solid carbide short length flat end mill;
- Number of flutes: 2;
- Cutting diameter: 1.5 mm
- Cutting length: 2.3 mm;
- Uncoated;

4.3.2 BFT TDMG 31 040 KA60

- Tool from BFT;
- Solid carbide flat end mill;
- Number of flutes: 3;
- Cutting diameter: 4 mm
- Cutting length: 9 mm;
- Coated;

4.3.3 Zecha 481.030

- Tool from Zecha;
- Solid carbide flat end mill;

-
- Number of flutes: 2;
 - Cutting diameter: 0.3 mm
 - Cutting length: 0.3 mm;
 - Uncoated;

4.4 Measurement equipments

4.4.1 Mahr MarSurf CWM 100

The MarSurf CWM 100 is a precise optical measuring instrument with sub-nanometer resolution combining a confocal microscope with a white light interferometer, sold by the company Mahr. In Figure 46 there is a picture of the Mahr MarSurf CWM 100.



Figure 46. Mahr MarSurf CWM 100.

The main features of this device are summarized as follow:

- High precision with sub-nanometer resolution
- Universal suitability for technical, optical and reflective surfaces; also for surfaces of printed circuit boards and semiconductor products as well as biological tissues
- 2D surface analysis and measuring evaluations
- Topographic 3D surface analysis and measuring evaluations
- Intelligent measuring strategies, fast measurements in short measuring times
- Microscope image field sizes, easily expandable by fully automatic stitching
- Automatic table or object positioning: 100 mm x 100 mm, longer distances on request
- A wide range of lenses allows for an ideal adaptation to the measurement object
- Solid construction with granite base plate and granite column for the best possible vibration damping

This device finds some applications in different fields:

- Mechanical Engineering, to qualify and quantify roughness, geometry and wear volume
- Electronics and semiconductors, component inspection down to the sub-micrometer range for defect-free products
- Medical Technology, quality assurance of medical surfaces in production and laboratory
- Material Science, optimization of functional properties of new surfaces and products
- Microsystems Technology, measure complex surface geometries of smallest components with nanometer precision

4.5 Sensors and acquisition chain

4.5.1 Kistler Microdynamometer 9317b

The first device for the acquisition of the forces is composed by a microdynamometer – Kistler 9317b (see Appendix C), on which the samples have been screwed. The dynamometer is able to measure forces up to 2 kN. The core of the dynamometer is composed of three piezoelectric quartz crystal layers oriented in the three orthogonal directions. The core is protected by a shell and separated by the plates by mean of two ceramic rings, which provide electrical insulation. The dynamometer is connected to three different charge amplifiers – Kistler 5015 A1000, that are independent and represent the three Cartesian directions x, y and z of the forces. Through 3 BNC cables, the three channels are linked to an acquisition board NI-9234, with 4 synchronous channels, $\pm 5V$. Finally, the acquisition board is connected to a PC with a USB cable, on which the software NI Experire Data is used to set properly the parameters required by the dynamometer and to acquire the forces. All these devices are showed in Figure 47:



Figure 47. Forces acquisition set up: (a) load cell, (b) channel x, y and z.

This is the simplified scheme of the acquisition procedure, Figure 48:

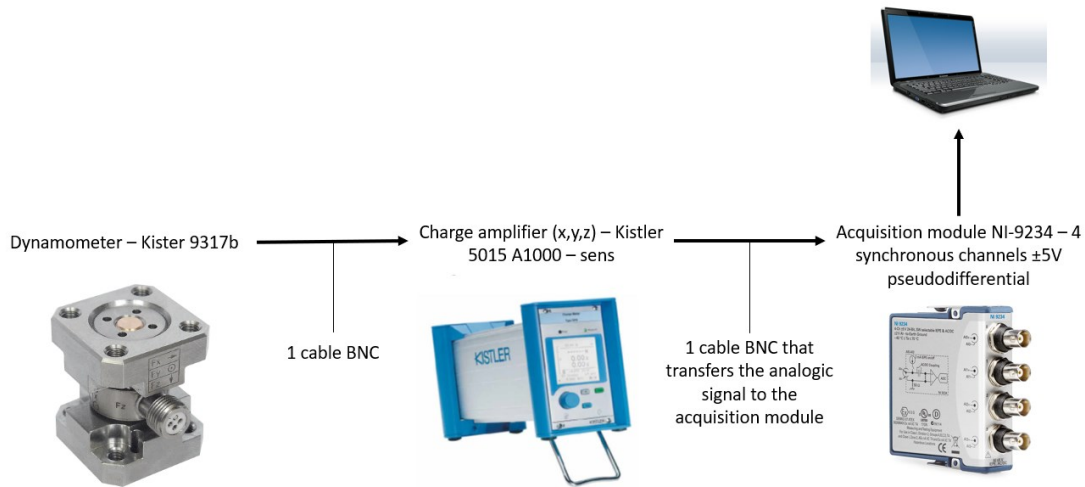


Figure 48. Acquisition system scheme for Kistler 9317b.

4.5.2 Kistler MicroDyn type 9109AA

The second system for the acquisition of the forces is composed by the Kistler MicroDyn type 9109AA (see Appendix D), on which the samples have been screwed. In Figure 49, a picture of the dynamometer is presented:



Figure 49. Kistler MicroDyn type 9109AA.

This dynamometer has been borrowed by Kistler Germany to Politecnico di Milano for only one week, thus it has been used only for the measurements of few force signals. The multicomponent dynamometer is used for dynamic and quasistatic measurement of the 3 orthogonal components of any force acting on the cover plate of 30x30 mm (forces in x, y and z directions). It is able to measure forces up to 500 N. The dynamometer is extremely rigid and therefore has a high natural frequency ≥ 15

kHz. The samples have been fixed on the plate of the dynamometer with 4 screws M4x25, with 3 Nm of tightening torque as suggested by the Kistler instruction manual. To fix the device on the working table 8 screws M4x25 have been used. The dynamometer is linked to the charge amplifier and data acquisition device - Kistler LabAmp type 5167Ax1, by an 8-channel high resistant connecting cable type 1677A5 with 9 pins. The software used for the force acquisition is DynoWare type 2825A, given by Kistler. The acquisition scheme is reported in Figure 50:

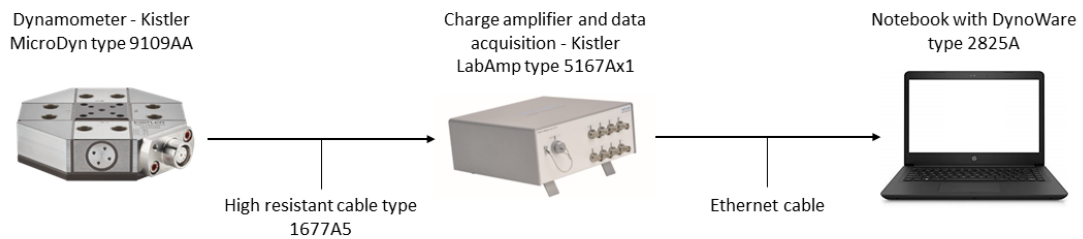


Figure 50. Acquisition system scheme for Kistler 9109AA.

4.6 Softwares

Since the outputs given by the entire forces measurement system are text files containing the values of the three components of the force acquired by the load cell, the software MATLAB has been used: the script used to analyze all the data to perform the experimental analysis is reported in the Appendix E.

The part programs for performing milling operations on Kern have been written directly on the machine or using the Heidenhain iTNC530 simulator, when the program contains less the 100 rows or using a generic text file program, depending if the machine was free or used for other operations. All the part programs are in the Appendix A.

Minitab software has been used to carry out the statistical analysis of the data acquired.

Mountains Map is the software used for the surfaces analysis of the machined surfaces extracted by using the Mahr MarSurf CWM 100. It has been used to evaluate the surface roughness and extract the surface texture parameters.

4.7 Setup

4.7.1 Setup for case study 1

For the screening operation, two samples of H13 steel (size 42x42x12 mm) cut from a block of the same material have been prepared to be screwed to the Kistler MicroDyn type 9109AA in order to both test the device and to acquire the forces of the slotting operations.

The microdynamometer has been screwed on the Kern EVO plane using 8 screws (M4), as suggested by the instruction manual, and a sample has been placed on it to measure the forces during cutting test.

In Figure 51, the pictures of the two samples are reported:

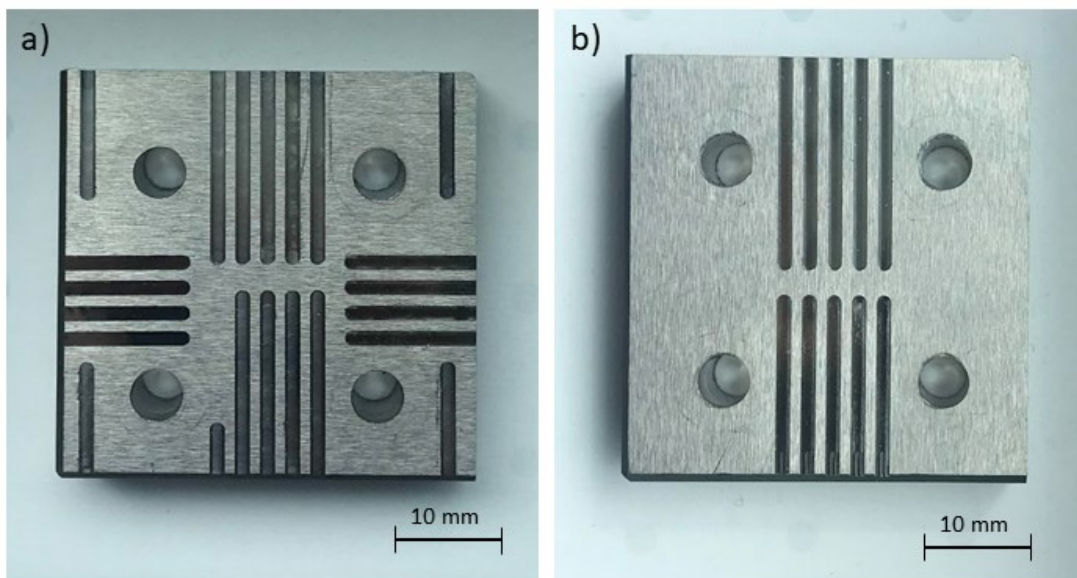


Figure 51. (a) sample 1 and (b) sample 2 in H13 steel for screening operations.

To acquire the forces in x, y and z directions, the Kistler MicroDyn type 9109AA has been used, set at a sampling frequency of 100 kHz. The software used for the acquisition is DynoWare Type 2825D-03 downloaded from Kistler website.

When the forces in all the three components have been acquired, they have been processed using a Matlab code (Appendix E), to extract the values of the planar, vertical and total force. For the acquisition of the surface parameters, the Mahr MarSurf CWM 100 has been used.

For the extended evaluation on H13 steel, the setup is quite similar to the previous case, but in this case the samples have a dimension of 25x25x12 mm and, instead of using the MicroDyn type 9109AA, the Kistler microdynamometer 9317b has been used. The sampling frequency used for this experiment is set to 51.2 kHz, that is the maximum value allowed by the acquisition board.

Regarding the setup for machining the inserts, they have been machined on the Kern EVO 5-axis CNC machining centre. The main problem is due to the gripping of the workpiece due to its circular shape and to the fact that it is impossible to screw it to some support. Therefore, as regards the setup, a clamp was placed on the Kern EVO plane and a support was realized that worked as a clamp to hold the insert. The image of this aluminum support is shown in Figure 52:

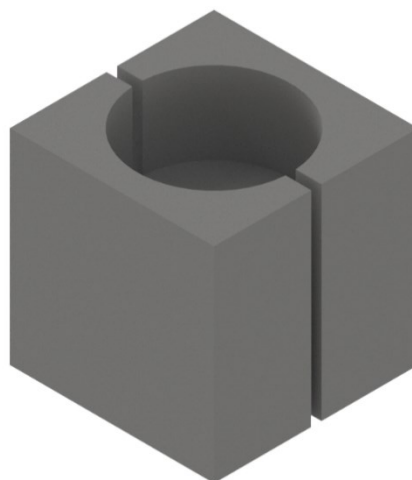


Figure 52. 3D view of the aluminum support.

The support is made from an aluminum cube measuring 20x20x20 mm, in which a circular hole of 15 mm diameter was made, just like the size of the central body of the insert, and 8 mm deep. Finally, the support was cut in half and divided into two equal parts to allow the workpiece to be gripped when tightened in the clamp, positioning it so that the cutting plane is parallel to the contact surfaces of the clamp. The fact of starting from a cube is due to the need to have two flat surfaces to ensure contact with the surfaces of the clamp. In this way it was possible to solve the problem of gripping, but this solution does not allow the acquisition of cutting forces during processing, a compromise that can however be accepted as they have already been acquired during the various previous experiments.

Therefore, the setup is composed by the clamp positioned on the Kern EVO plane, by the aluminum support that is tightened in the clamp, inside which the insert to be machined is positioned. To have the maximum possible flatness, the insert is mounted using a Johansson gauge block that comes in contact with the surface of the clamp, as a reference surface, and the surface of the workpiece to be machined. With this method, using the touch probe of the machine in various points of the insert, the lack of planarity was at most 1 μm , therefore negligible.

4.7.2 Setup for case study 2

The cutting experiments were performed on the Kern EVO 5-axis CNC machining centre, using the $\varnothing 0.3$ Zecha 481.030 uncoated tool. The test workpiece has a rectangular shape, Figure 53, and has a NiP coating of 500 μm . The fact of having two parallel flat surfaces allows to grab the piece directly in the clamp, without having to design a support to for it. The main problem arises from the need to keep the workpiece in the clamp with a certain inclination, a problem generated by the fact that the machine no longer has the fourth and fifth axis. To overcome this problem, the procedure is rather simple, but this generates a loss of precision in positioning because it's done manually: the piece is grabbed in the clamp with a certain unknown inclination, then the height in z is measured with the touch probe in two points so as

to know this inclination and finally rotated manually in order to obtain the desired position, always proceeding with the method just described. The procedure is quite long, so the error, within which the inclination has been defined acceptable, is 0.1° . Once the piece is in position and has been tightened in the clamp, no other setup operations are required and the experimentation can begin.

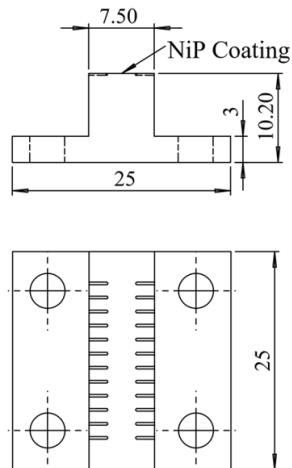


Figure 53. Design of the flat insert for cutting tests on NiP.

5. MODELLING AND CALCULATIONS

5.1 Modelling of cutting operations

The modelling of the cutting operations is proposed starting from simulations and experimental face milling tests [29]. Observing what happens in the simulation and comparing this with the experimental results, it is noted that during slotting if the tool overruns the workpiece with small or no static/dynamic deflection of the tool, the cutting edges will engage on the rear side of the tool in the already machined surface after the main cut. Based on the superposition of the feed and cutting movements, a trochoidal-like mark pattern resulted on the surface. The influence of back cuts on the resulting surface pattern is shown in Figure 54, with a comparison of idealized and modelled cutting edges in relation to experimental measurements:

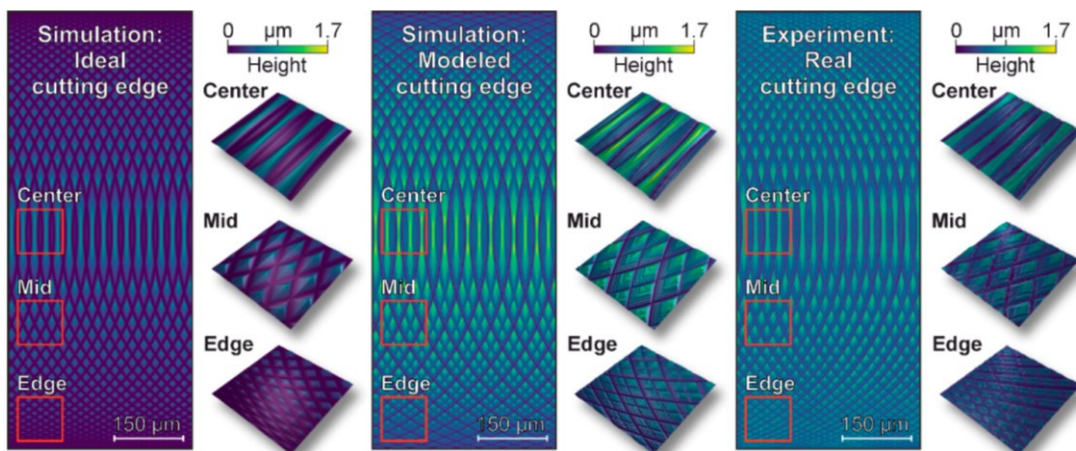


Figure 54. Influence of the back cut on the surface topography [29].

The additional engagements of the tool result in a significant reduction of the average roughness depth, which is attributed to a reduction of the depth of the marks. As shown in Figure 55, the surface obtained by considering a tool without defects is very different from that obtained from a tool with micro defects: in the first case there is a surface whose profile is ideal characterized by straight lines following the cut, while in the second such defects are clearly evident from the fact that these lines are undulating, following the geometry of the tool that is no longer ideal.

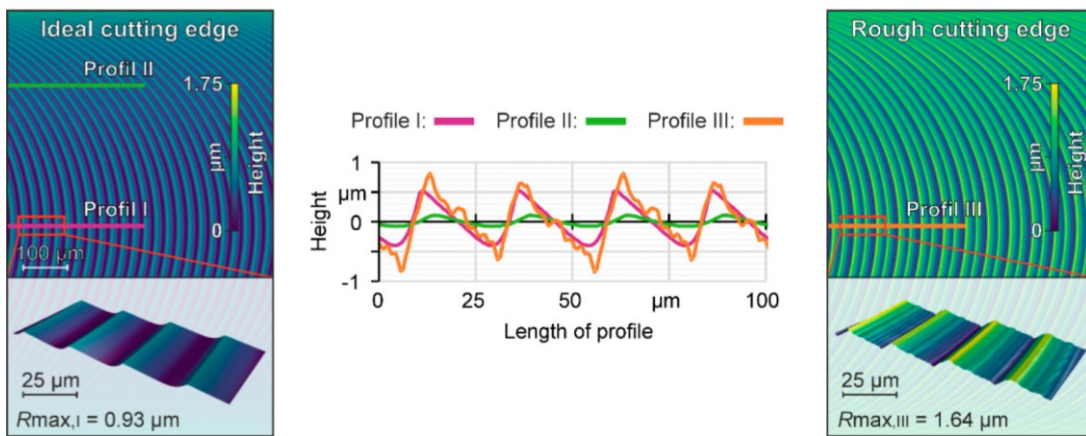


Figure 55. Influence of the microgeometric properties of cutting edges on the surface roughness, comparing an ideal shape with a detailed representation [29].

The aim of the slotting operations is to use the geometry of the tool and its deflection during cutting to reproduce a regular pattern on the workpiece to recreate a diffraction grating for the light. Let's consider a tool with two flutes, with an orientation of 180° one to the other (typical case for a tool for micromilling). When the tool hits the workpiece and starts to cut, a force opposite to the direction of the feed is generated, Figure 56:

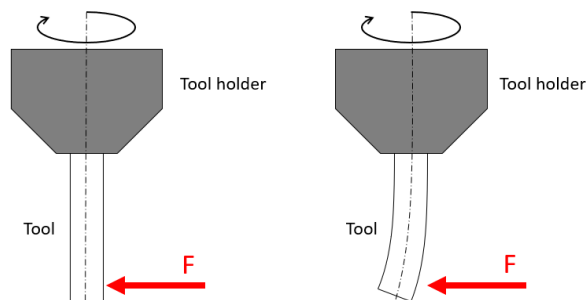


Figure 56. (a) undeformed tool, (b) bended tool.

That force, whose value is equal to the value of the force in the feed direction, deflects the tool depending on the stiffness of it; the force (cutting force) depends on three parameters:

- The feed per tooth, i.e. f_z ;
- The depth of cut, i.e. a_p ;
- The properties of the material to be cut.

$$F_{c,i} \cong k_{cs} \cdot (f_z \cdot \sin \theta_i)^{1-x} \cdot a_p$$

Depending on the stiffness of the tool, its dimension and the force applied on it, two models have been proposed, the first one the represents an ideal case in which the force is low and the tool is so rigid that it is possible to assume that the tool does not deflects during cutting operations (tool with infinite stiffness). This situation well describes a tool for macro cuttings; in the second one, the force is high and the tool is not enough rigid, thus it bends and during cutting it works in a deflected mode (tool with finite stiffness). This situation well describes a tool for micromachining.

A third model is proposed, regarding the cutting mechanism using the rotation of the head of the machine.

Tool with infinite stiffness (ideal case)

This case well represents the situation in which the tool is subjected to a force that is too low to generate a notable deflection, thus it's possible to assume that the tool doesn't bend and it is completely straight. This situation occurs when the cutting parameters, i.e. f_z and a_p are too low to generate a great value of force on the tool or the diameter of the tool is too big to generate a certain deflection.

In Figure 57 is reported a scheme of this situation:

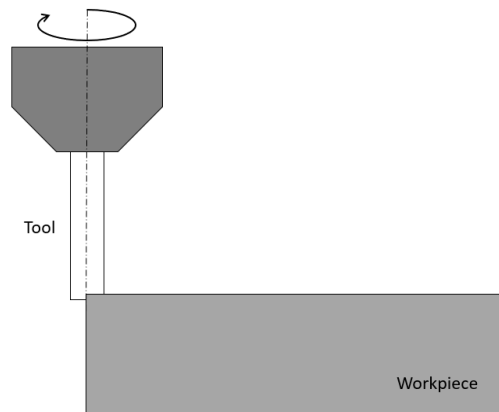


Figure 57. Tool with infinite stiffness cutting scheme.

Considering a tool with two flutes, the front tooth cuts the material generating the chip and a regular pattern, while the rear one, as no deflection is generated, damages the surface already created. The peaks thus created by the passage of the front tooth are cut by the action of the rear tooth upset and the regular pattern is no more present. In Figure 58 the trajectory done by the two teeth of the mill is reported:

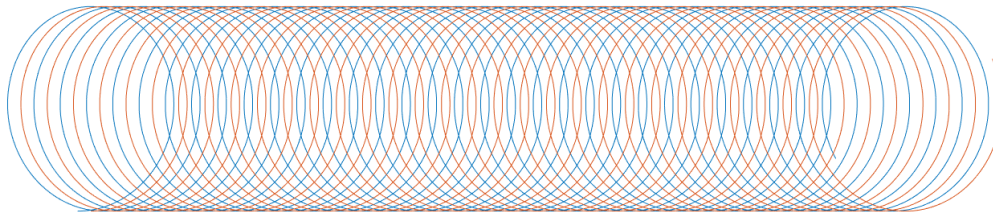


Figure 58. Trajectory done by the two teeth of a mill.

As shown by Figure 58, if the tool doesn't bend, the effect of the rear tooth is very marked in the entire slot.

Tool with finite stiffness (real case)

This case well represents what happens during the slotting operation on H13 steel using the tool with 1.5 mm as diameter. The forces acting on the tool are in the order of magnitude of 10 N and combined with the low moment of inertia of the tool (the value is proportional to the diameter at the forth power) generates the desired

deflection necessary to realize a regular pattern on the surface of the samples. Figure 59 shows the condition in which the tool works in a bend condition: only the front tooth working, while the rear one is not in contact with the sample and doesn't damage the already machined surface.

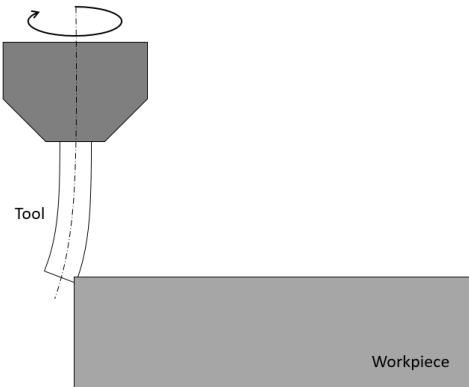


Figure 59. Tool with finite stiffness cutting scheme.

As results of this deflection, the pattern realized on the sample would be different from that obtained previously, Figure 58; the passage of only one tooth would generate a regular surface like that shown in Figure 60:

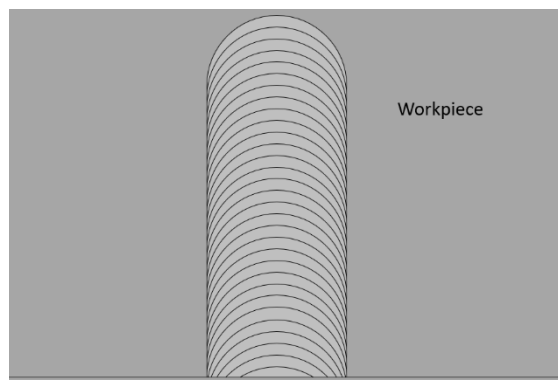


Figure 60. Regular structure generated by the passage of the tool.

As shown, the distance between two consecutive traces is equal to the feed per tooth, considering an ideal tool without considering a possible run-out error.

Inclined head machining

A method for machining and producing regular traces on the surface of a material consists in inclining the head of the mill in order to permit only to the front tooth to do the cutting. In this way, by imposing a certain rotation on the head, the tool can work with its own axis not parallel to the normal of the plane of the workpiece, allowing only the front tooth to cut the material. In Figure 61, a scheme to better clarify this mechanism:

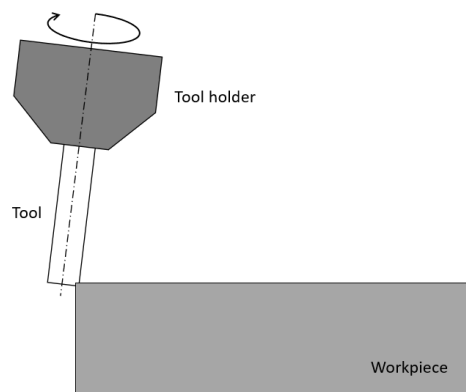


Figure 61. Scheme of the inclined tool (rotation of the B-axis).

This method is similar to the case of tool with finite stiffness, but in this case instead of using the deflection, it is used a real rotation of it, because of its high stiffness that not allow to deflect this tool.

5.2 Modelling of the run-out on surface regularity

The effect of the run out is however to be considered when dealing with micrometric processes: the presence of this phenomenon is therefore evident in the case of machined surfaces in which the alternation of peaks and valleys with the same height is not equal to the advancement to tooth. It is possible that three scenarios occur:

- Case 1) run-out = 0 (ideal case); in this case the two teeth work in the same way and the peaks will all have the same height, with a period equal to the feed per tooth.

-
- Case 2) run-out < feed per tooth; in this case both the teeth work during the cut, but in a different way and the generated profile will see the alternation of peaks at different heights with a period equal to twice the feed per tooth.
 - Case 3) run-out > feed per tooth; in this case only one of the two teeth is working, while the other does not cut material. The result of this is the presence of only one peak per revolution of the tool distant from the following of a period equal to twice the feed per tooth.

5.3 Calculations on cutting parameters for Stavax steel

For the calculation of the value of the cutting force during the slotting operations, the formula for the cutting force for conventional milling is used. The formula for calculating the cutting force is:

$$F_{c,i} \cong k_{cs} \cdot (f_z \cdot \sin \theta_i)^{1-x} \cdot a_p$$

Considering this formula and considering the case in which the material to be cut is the same, it is possible to rewrite that:

$$f_z^{1-x} \cdot a_p = \text{constant}$$

Through the last formula it's possible to extract the value of a_p or f_z keeping constant the cutting force, by imposing one of the two variables. This method has been used for the calculation of the cutting parameter for machining the inserts (case study 1).

5.4 Calculations on NiP coating radial depth of cut

Considering the experimentation on the inclined sample of NiP coated steel, each test of cutting consists of 10 slots realized in parallel, with different radial depth of cut, determined by the desired z-step and the inclination of the workpiece, Figure 62.

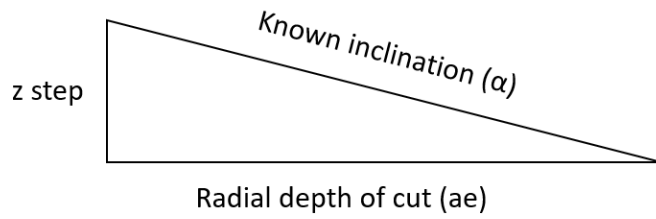


Figure 62. Scheme to calculate the radial depth of cut.

In this way the radial depth of cut, i.e. a_e , that is the same value for the displacement in x direction at each passage of the tool, that is necessary to know for writing the part program for machining, is calculated using a simple trigonometric formula and it is function of two parameters:

$$a_e = z_{step} \cdot \cot(\alpha)$$

In the previous formula, α is the inclination angle from the plane of the clamp (parallel to the plane of the Kern EVO) and the top surface of the sample.

6. CASE STUDY 1: EXPERIMENTS

6.1 Screening operations on H13 steel

The first operation to be done is to understand which cutting parameters influence the regularity on the surfaces considering H13 steel as material to be cut.

To realize the diffraction gratings, different factors, i.e. cutting speed (V_c), depth of cut (a_p) and feed per tooth (f_z), have been considered and varied on different level not following a complete design of experiments, but in a random way, aimed to understand if the required structure would have been obtained or not.

The selected values of the parameters are:

- Cutting speed: 47.1 – 94.2 – 141.4 – 188.5 m/min
- Feed per tooth: 5 – 7 – 15 – 30 $\mu\text{m}/\text{tooth}$
- Depth of cut: 0.04 – 0.08 mm

The two samples have been flattened on both the upper and lower surface and then have been pierced to permit the link with the dynamometer using 4 screws (M4). One side of the first sample (sample1) have been used entirely, cutting a total of 22 slots, while the second one (sample2) have been used only for 10 slots, to leave some other space for future tests. A total of 32 slots have been cut using the $\varnothing 1.5$ mm tool from Mitsubishi.

Here is reported the tables, Tables 3 and 4, containing all the values of the factors for each test and the values of the output variables; as output variables, it has been used

the RMS value of planar force F_{xy} , the RMS value of vertical force F_z , the RMS value of the resultant force F_{tot} and the surface roughness S_a .

Test n.	S [rpm]	Vc [m/min]	fz [$\mu\text{m}/\text{t}$]	ap [mm]	F_{xy} [N]	F_z [N]	F_{tot} [N]	S_a [μm]
1	30000	141.4	30	0.08	8.80	0.73	8.83	0.593
2	30000	141.4	30	0.08	9.76	0.86	9.79	0.552
3	30000	141.4	15	0.08	7.20	1.01	7.27	0.24
4	30000	141.4	5	0.08	4.81	0.92	4.90	0.21
5	20000	94.2	30	0.08	11.18	1.50	11.28	0.317
6	30000	141.4	30	0.04	6.64	1.98	6.93	0.179
7	30000	141.4	30	0.04	6.50	2.48	6.96	0.177
8	30000	141.4	15	0.04	4.91	1.19	5.05	0.109
9	30000	141.4	5	0.04	3.27	1.86	3.77	0.0846
10	20000	94.2	30	0.04	6.66	2.45	7.10	0.202
11	10000	47.1	5	0.08	-	-	-	0.202
12	10000	47.1	5	0.04	4.18	1.00	4.30	0.058
13	10000	47.1	7	0.08	7.63	1.37	7.75	0.0672
14	10000	47.1	7	0.04	-	-	-	0.089
15	40000	188.5	5	0.08	6.11	2.24	6.51	0.114
16	40000	188.5	5	0.04	3.31	2.89	4.40	0.132
17	40000	188.5	7	0.08	7.11	2.83	7.66	0.0727
18	40000	188.5	7	0.04	3.45	1.71	3.86	0.137
19	30000	141.4	5	0.08	7.78	2.96	8.32	0.104
20	20000	94.2	30	0.08	12.12	4.30	12.86	0.159
21	20000	94.2	30	0.04	9.70	4.36	10.64	0.132
22	30000	141.4	15	0.04	-	-	-	0.09

Table 3. Factors and outputs for screening operation on H13, sample 1.

Test n.	S [rpm]	Vc [m/min]	fz [$\mu\text{m}/\text{t}$]	ap [mm]	F_{xy} [N]	F_z [N]	F_{tot} [N]	S_a [μm]
23	30000	141.4	15	0.08	9.07	2.40	9.38	0.0846
24	30000	141.4	15	0.12	11.54	3.67	12.11	0.107
25	30000	141.4	15	0.16	14.05	3.55	14.49	0.106
26	30000	141.4	15	0.20	16.09	3.13	16.40	0.0972
27	30000	141.4	15	0.24	18.73	3.04	18.98	0.100
28	40000	188.5	15	0.08	8.51	4.21	9.50	0.0911
29	40000	188.5	15	0.12	13.63	1.89	13.76	0.101
30	40000	188.5	15	0.16	16.72	5.51	17.61	0.0899
31	40000	188.5	15	0.20	19.85	3.85	20.22	0.103
32	40000	188.5	15	0.24	22.85	6.95	23.88	0.0586

Table 4. Factors and outputs for screening operation on H13, sample 2.

In the table is also reported the values of the spindle rotation in revolute per minute; the aim of this column is that in the part program, it has been set these values and not the values of cutting speed, but the two factors are linked by the following formula:

$$V_c = \pi \cdot d \cdot S$$

6.1.1 Response variable: Fxy

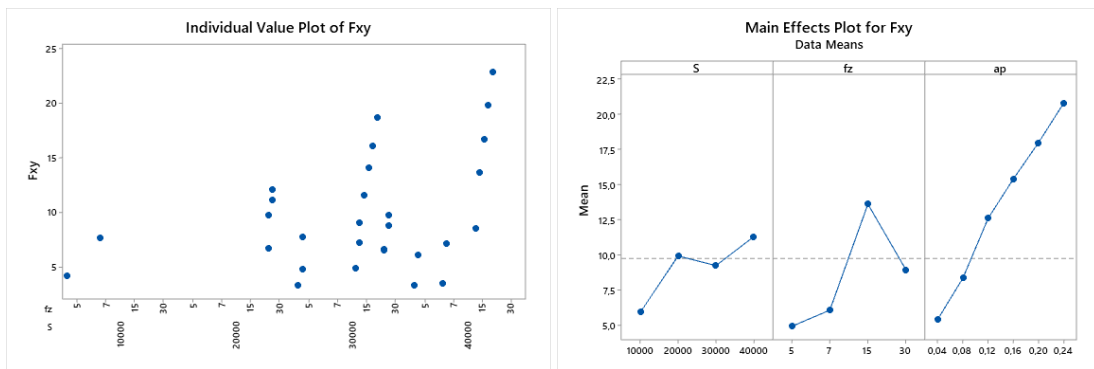


Figure 63. (a) individual value plot for Fxy, (b) main effect plot for Fxy, screening on H13.

Individual value plot shows no outliers, Figure 63(a). Experiments were not completely randomized or designed and that's why for cutting speed of 10000 and 20000 there are not lot of experiments. The main effects plot displays the response means for each factor level in sorted order, Figure 63(b). A horizontal line is drawn at the grand mean. The interaction plot it's not considered because there are not any replicates.

General linear model

Factor Information

Factor	Type	Levels Values
S	Fixed	4 10000; 20000; 30000; 40000
fz	Fixed	4 5; 7; 15; 30
ap	Fixed	6 0.04; 0.08; 0.12; 0.16; 0.20; 0.24

Analysis of Variance

Source	DF	Adj SS	Adj MS	F-Value	P-Value
S	3	19.84	6.614	4.92	0.012
fz	3	34.61	11.536	8.58	0.001
ap	5	326.60	65.320	48.58	0.000
Error	17	22.86	1.345		
Lack-of-Fit	11	11.19	1.018	0.52	0.833
Pure Error	6	11.66	1.944		
Total	28	756.89			

Model Summary

S	R-sq	R-sq(adj)	R-sq(pred)
1.15959	96.98%	95.03%	91.16%

From the ANOVA table all the factors have p values lower than 0.05. But before concluding it's necessary to check the assumptions for standardized residuals and normality first.

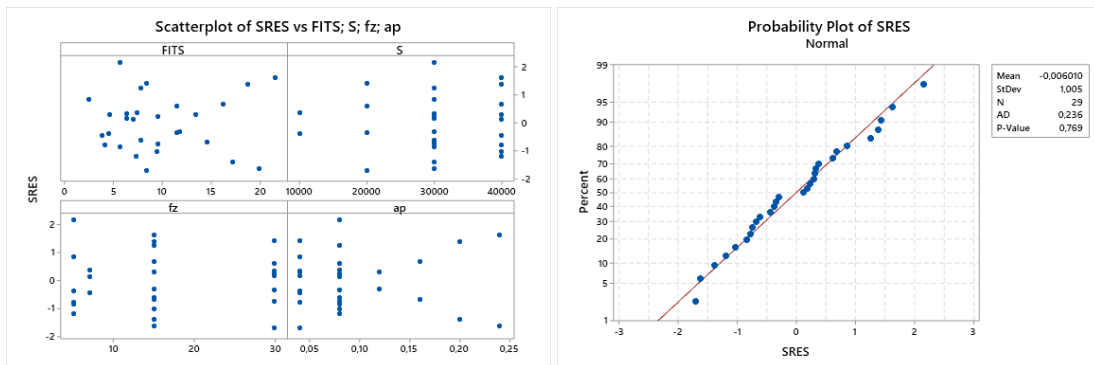


Figure 64. (a) scatterplot for Fxy of SRES vs FITS; S; fz; ap, (b) probability plot of SRES, screening on H13.

There are not any outliers. The hypothesis of normality cannot be refused, Figure 64. It's possible to conclude that all the three factors are significant on the RMS of the planar force.

6.1.2 Response variable: Fz

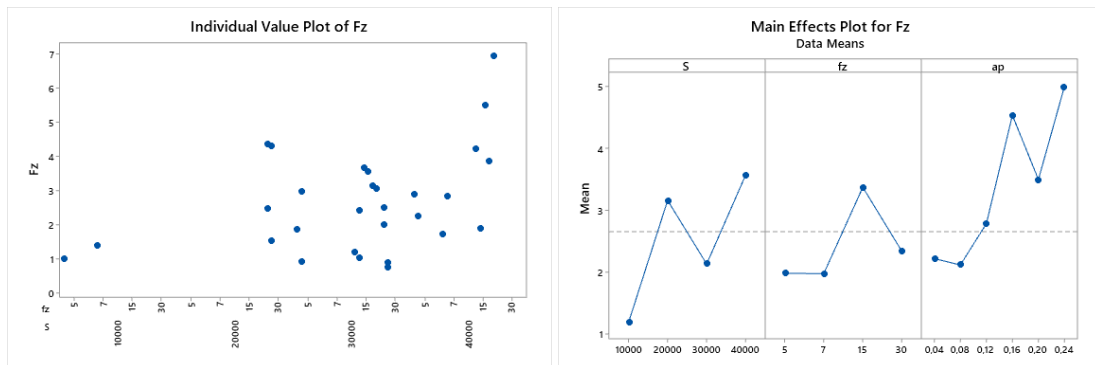


Figure 65. (a) individual value plot for Fz, (b) main effect plot for Fz.

Individual value plot shows no outliers, Figure 65. The interaction plot it's not considered because there are not any replicates.

General linear model

Factor Information

Factor	Type	Levels	Values
S	Fixed	4	10000; 20000; 30000; 40000
fz	Fixed	4	5; 7; 15; 30
ap	Fixed	6	0.04; 0.08; 0.12; 0.16; 0.20; 0.24

Analysis of Variance

Source	DF	Adj SS	Adj MS	F-Value	P-Value
S	3	13.5189	4.5063	3.32	0.045
fz	3	0.7214	0.2405	0.18	0.910
ap	5	11.2961	2.2592	1.67	0.197
Error	17	23.0561	1.3562		
Lack-of-Fit	11	14.1445	1.2859	0.87	0.605
Pure Error	6	8.9115	1.4853		
Total	28	61.8275			

Model Summary

S	R-sq	R-sq(adj)	R-sq(pred)
1.16458	62.71%	38.58%	0.00%

From the ANOVA table only the factor S has p values lower than 0.05. But before concluding it's necessary to check the assumptions for standardized residuals and normality first.

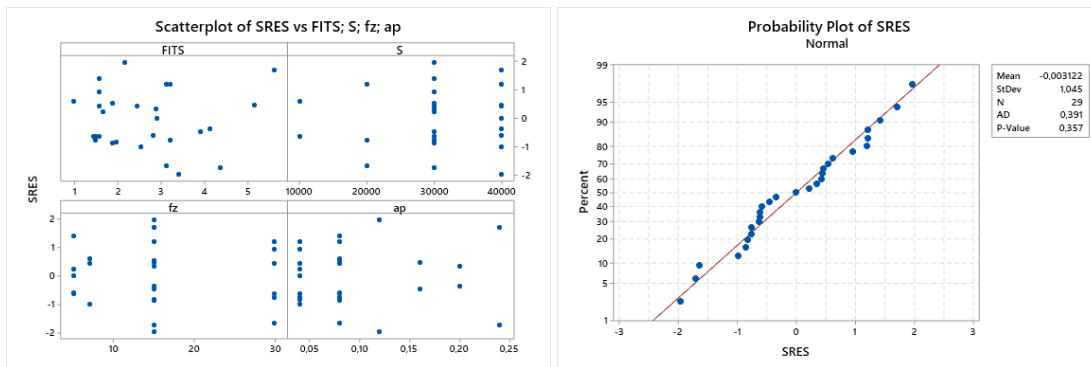


Figure 66. (a) scatterplot for Fz of SRES vs FITS; S; fz; ap, (b) probability plot of SRES.

There are not any outliers. The hypothesis of normality cannot be refused, Figure 66. It's possible to conclude that only the cutting speed is significant on the RMS of the vertical force.

6.1.3 Response variable: Ftot

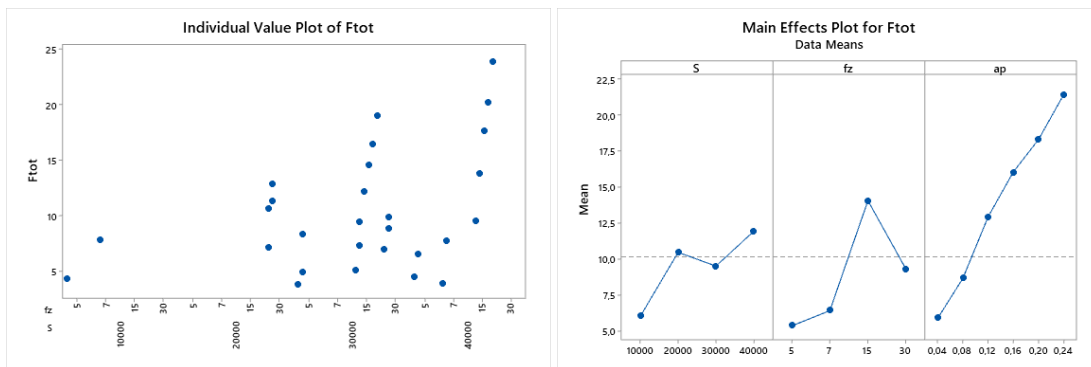


Figure 67. (a) individual value plot for Ftot, (b) main effect plot for Ftot.

Individual value plot shows no outliers, Figure 67. The interaction plot it's not considered because there are not any replicates.

General linear model

Factor Information

Factor	Type	Levels Values
S	Fixed	4 10000; 20000; 30000; 40000
fz	Fixed	4 5; 7; 15; 30
ap	Fixed	6 0.04; 0.08; 0.12; 0.16; 0.20; 0.24

Analysis of Variance

Source	DF	Adj SS	Adj MS	F-Value	P-Value
S	3	27.21	9.071	5.46	0.008
fz	3	32.85	10.949	6.59	0.004
ap	5	326.53	65.306	39.32	0.000
Error	17	28.23	1.661		
Lack-of-Fit	11	12.18	1.108	0.41	0.903
Pure Error	6	16.05	2.675		
Total	28	777.75			

Model Summary

S	R-sq	R-sq(adj)	R-sq(pred)
1.28872	96.37%	94.02%	89.55%

From the ANOVA table all the factors have p values lower than 0.05. But before concluding it's necessary to check the assumptions for standardized residuals and normality first.

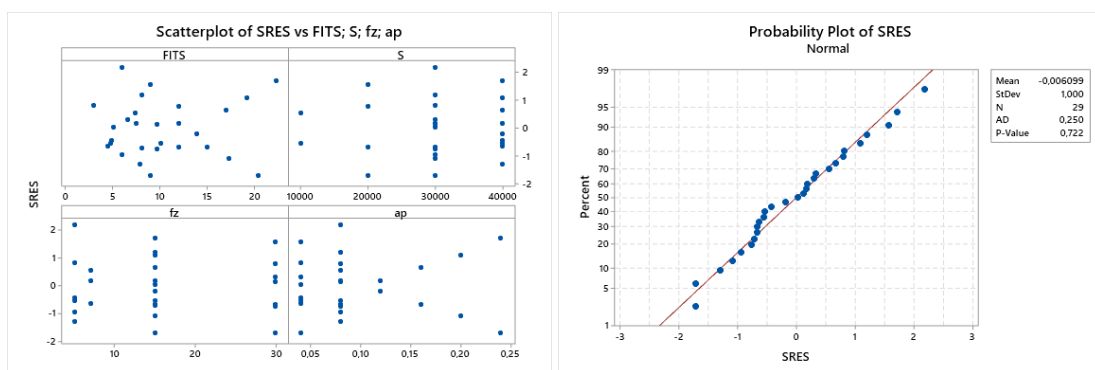


Figure 68. (a) scatterplot for Ftot of SRES vs FITS; S; fz; ap, (b) probability plot of SRES.

There are not any outliers. The hypothesis of normality cannot be refused, Figure 68. It's possible to conclude that all the three factors are significant on the RMS of the total force.

6.1.4 Response variable: Sa

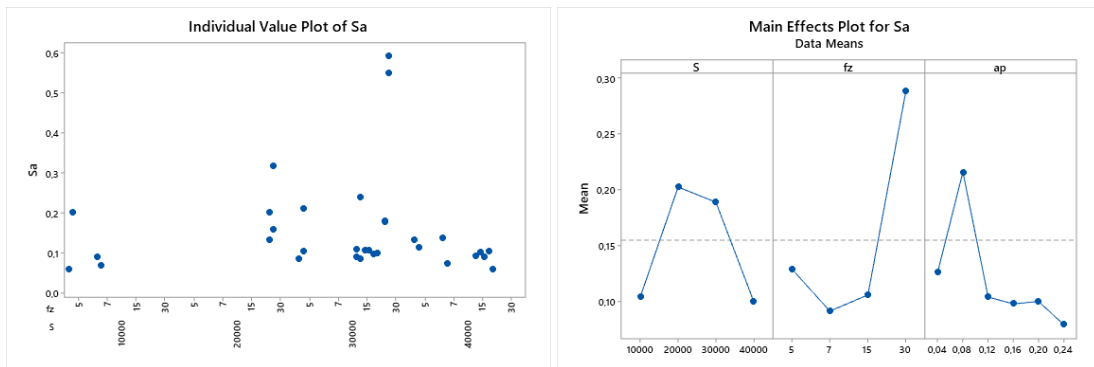


Figure 69. (a) individual value plot for Sa, (b) main effect plot for Sa.

Individual value plot shows two possible outliers, but a deeper analysis has to be done to understand if they are outliers or not, Figure 69. The interaction plot it's not considered because there are not any replicates.

General linear model

Factor Information

Factor	Type	Levels	Values
S	Fixed	4	10000; 20000; 30000; 40000
fz	Fixed	4	5; 7; 15; 30
ap	Fixed	6	0.04; 0.08; 0.12; 0.16; 0.20; 0.24

Analysis of Variance

Source	DF	Adj SS	Adj MS	F-Value	P-Value
S	3	0.06122	0.020405	2.57	0.083
fz	3	0.17390	0.057967	7.30	0.002
ap	5	0.05996	0.011992	1.51	0.231
Error	20	0.15883	0.007941		
Lack-of-Fit	13	0.12518	0.009629	2.00	0.181
Pure Error	7	0.03365	0.004807		
Total	31	0.47591			

Model Summary

S	R-sq	R-sq(adj)	R-sq(pred)
0.0891150	66.63%	48.27%	29.57%

From the ANOVA table only the factor fz has p values lower than 0.05. But before concluding it's necessary to check the assumptions for standardized residuals and normality first.

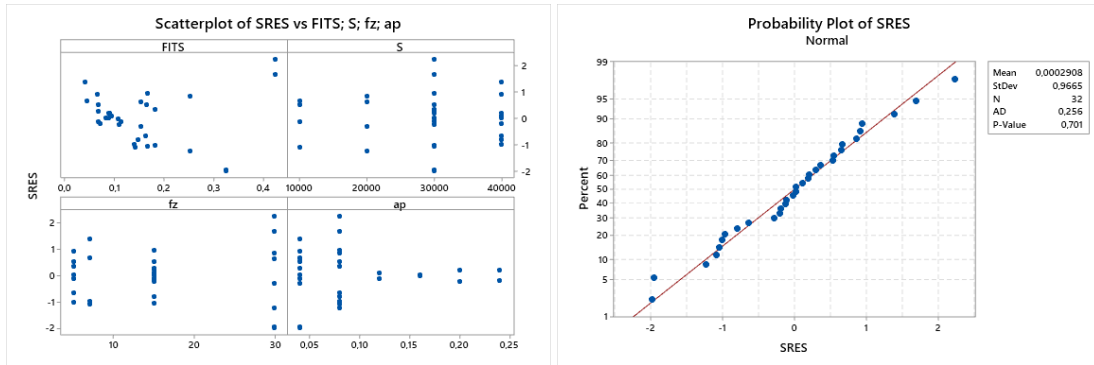


Figure 70. (a) scatterplot for Sa of SRES vs FITS; S; fz; ap, (b) probability plot of SRES.

There are not any outliers. The hypothesis of normality cannot be refused, Figure 70. It's possible to conclude that only feed per tooth is significant on the surface roughness.

6.1.5 Effect of the cutting parameters on regularity

Once all the tests have been done on the two samples of H13, it's necessary to characterize the regularity of the profiles obtained by the passage of the tool, understanding the phenomenon that generates the texture. Here are reported some profiles extracted using the Mahr MarSurf CWM 100 (magnification 50X, NA 0.60) with the corresponding cutting parameters:

- Cutting speed: 141.4 m/min (30000 rpm);
- Feed per tooth: 30 $\mu\text{m}/\text{tooth}$;
- Depth of cut: 0.08 mm

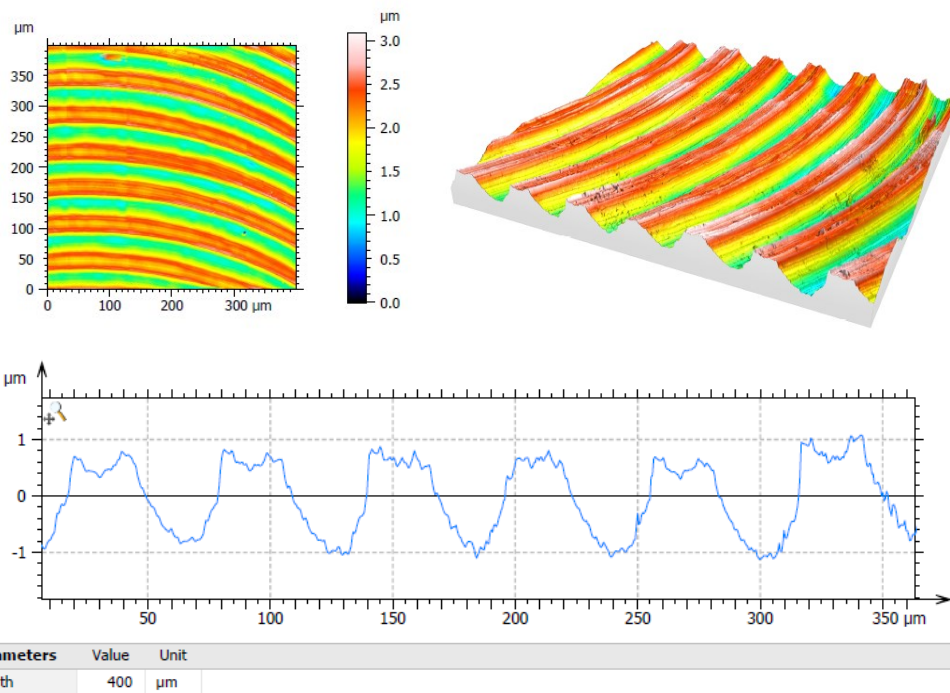
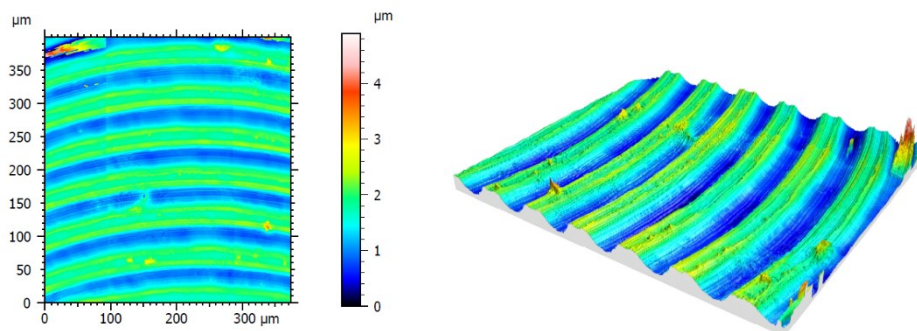


Figure 71. (a) extracted area, (b) 3D extracted area, (c) extracted profile at $V_c=141.4$ m/min, $f_z=30$ $\mu\text{m}/\text{tooth}$, $a_p=0.08$ mm (replica 1).

- Cutting speed: 141.4 m/min (30000 rpm);
- Feed per tooth: 30 $\mu\text{m}/\text{tooth}$;
- Depth of cut: 0.08 mm



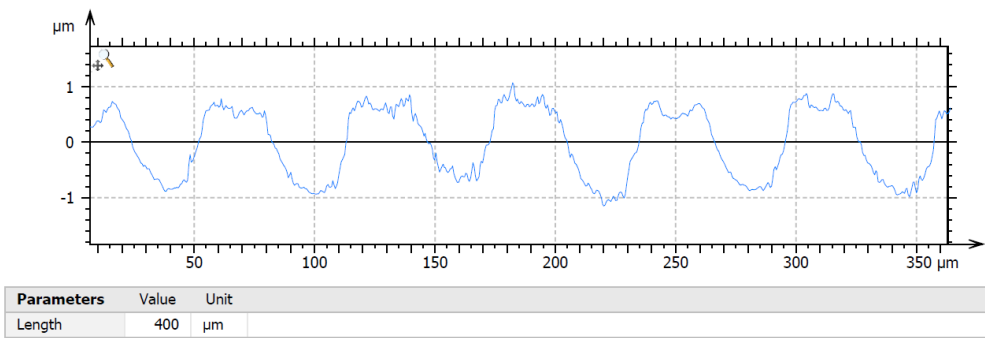


Figure 72. (a) extracted area, (b) 3D extracted area, (c) extracted profile at $V_c=141.4$ m/min, $f_z=30$ μm/tooth, $a_p=0.08$ mm (replica 2).

- Cutting speed: 141.4 m/min (30000 rpm);
- Feed per tooth: 15 μm/tooth;
- Depth of cut: 0.08 mm

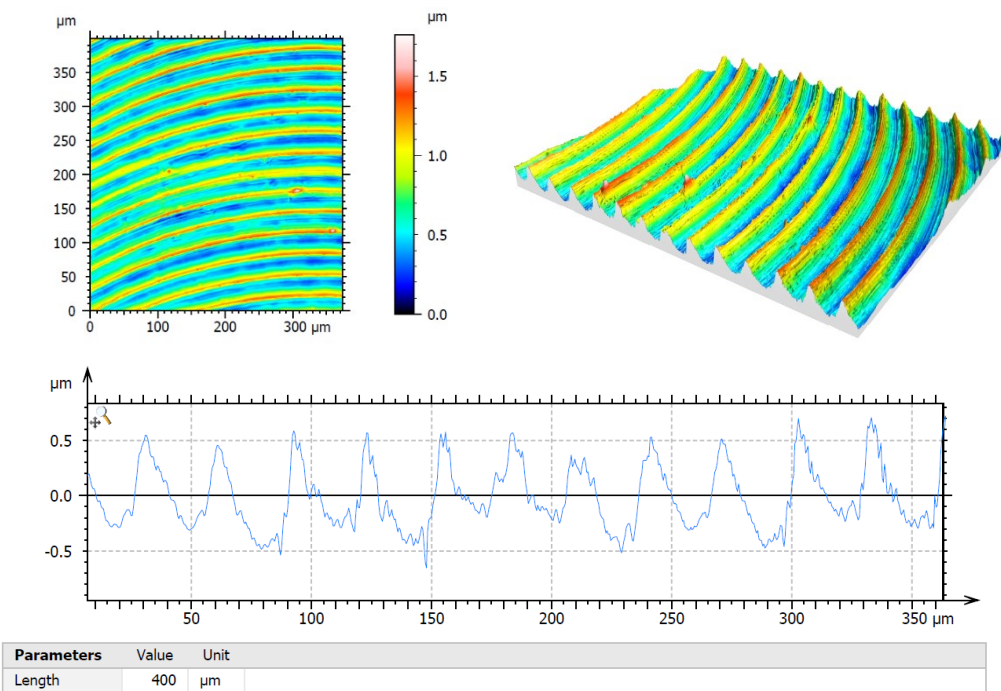


Figure 73. (a) extracted area, (b) 3D extracted area, (c) extracted profile at $V_c=141.4$ m/min, $f_z=15$ μm/tooth, $a_p=0.08$ mm.

- Cutting speed: 94.2 m/min (20000 rpm);
- Feed per tooth: 30 μm/tooth;
- Depth of cut: 0.04 mm

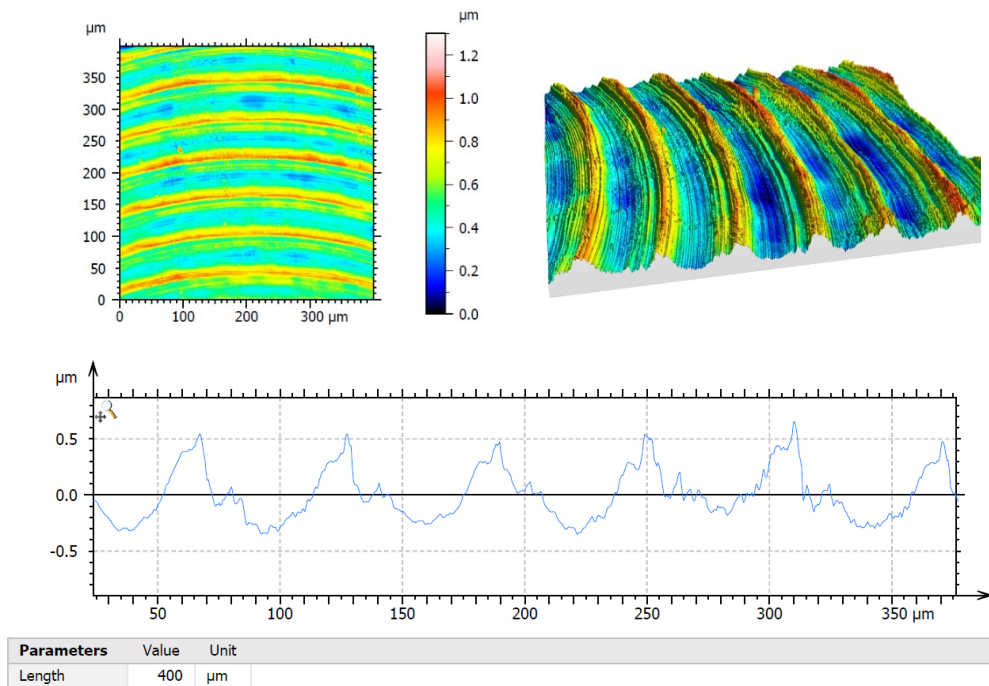
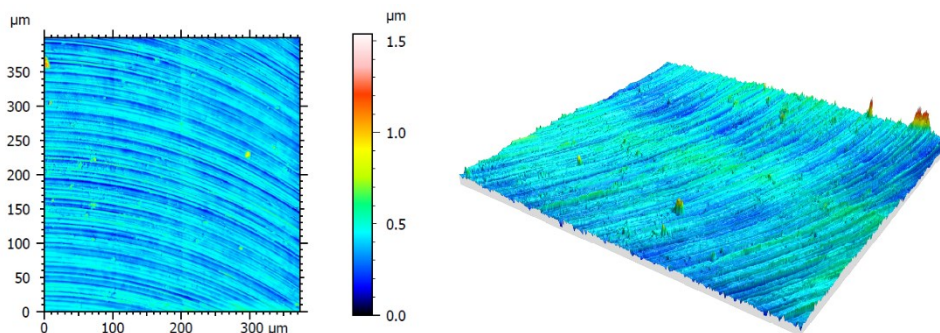


Figure 74. (a) extracted area, (b) 3D extracted area, (c) extracted profile at $V_c=94.2$ m/min, $f_z=30$ $\mu\text{m}/\text{tooth}$, $a_p=0.04$ mm.

These are examples of extracted profiles that present a regular pattern due to the passage of the tool during cutting operations.

- Cutting speed: 188.5 m/min (40000 rpm);
- Feed per tooth: 7 $\mu\text{m}/\text{tooth}$;
- Depth of cut: 0.08 mm



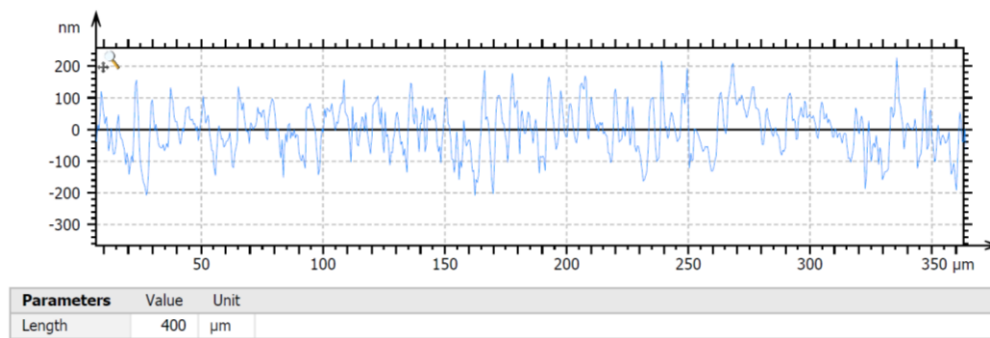


Figure 75. (a) extracted area, (b) 3D extracted area, (c) extracted profile at $V_c=188.5$ m/min, $f_z=7$ $\mu\text{m}/\text{tooth}$, $a_p=0.08$ mm.

This is an example of extracted profile that does not present a regular pattern due to the passage of the tool during cutting operations.

In the preliminary tests, desired results are obtained at following combination of parameters.

- $V_c=141.4$ m/min, $f_z=30$ $\mu\text{m}/\text{tooth}$, $a_p=0.08$ mm
- $V_c=141.4$ m/min, $f_z=15$ $\mu\text{m}/\text{tooth}$, $a_p=0.08$ mm
- $V_c=94.2$ m/min, $f_z=30$ $\mu\text{m}/\text{tooth}$, $a_p=0.08$ mm

Looking at all the extracted profiles, for the regularity of surface, the most significant factor is the feed rate: by decreasing it the regularity of surface decreases. The second important parameter is the depth of cut (a_p): higher values of it generated a more regular profile.

All these considerations are confirmed by the model of the tool with finite stiffness (paragraph 5.1). The cutting force therefore leads to the deflection of this tool during cutting, allowing the tool to work only with the front tooth and therefore leave a regular trace on the surface being machined.

6.2 Extended evaluation on H13 steel

Before starting with the realization of the diffraction grating on the inserts for injection moulding, it's necessary to perform a deeper analysis on the parameters

that influence the regularity of the profile, selecting the best value for each factor. From the screening experiment, an idea of what are the significant parameters and what are the values around which to conduct an experiment is obtained.

A 2k factorial design with 3 replicates has been performed, for a total of 24 cutting tests, using the $\varnothing 1.5$ mm flat end mill from Mitsubishi as tool. Three factors, i.e. cutting speed, feed per tooth and depth of cut, have been varied on two levels each in a random order. In Table 5 are presented all the test conditions and the corresponding outputs of the experimentation:

Test n.	S [rpm]	Vc [m/min]	fz [$\mu\text{m}/\text{t}$]	ap [mm]	Fxy [N]	Ftot [N]	Sa [μm]
1	30000	141.4	15	0.07	4.62	5.16	0.158
2	30000	141.4	30	0.07	5.73	6.35	0.396
3	30000	141.4	15	0.10	7.36	7.56	0.243
4	30000	141.4	30	0.10	8.29	8.61	0.445
5	40000	188.5	15	0.07	10.94	11.19	0.442
6	40000	188.5	30	0.07	10.27	10.70	0.413
7	40000	188.5	15	0.10	12.26	12.48	0.157
8	40000	188.5	30	0.10	18.10	18.23	0.170
9	30000	141.4	15	0.07	5.27	5.64	0.179
10	30000	141.4	30	0.07	6.85	7.51	0.262
11	30000	141.4	15	0.10	7.76	8.01	0.130
12	30000	141.4	30	0.10	9.50	9.67	0.472
13	40000	188.5	15	0.07	15.57	15.85	0.136
14	40000	188.5	30	0.07	12.54	12.97	0.373
15	40000	188.5	15	0.10	13.47	13.70	0.157
16	40000	188.5	30	0.10	23.11	23.20	0.461
17	30000	141.4	15	0.07	5.70	6.23	0.184
18	30000	141.4	30	0.07	6.98	7.01	0.373
19	30000	141.4	15	0.10	7.38	7.67	0.135
20	30000	141.4	30	0.10	10.18	10.46	0.414
21	40000	188.5	15	0.07	18.72	18.94	0.121
22	40000	188.5	30	0.07	19.10	19.41	0.281
23	40000	188.5	15	0.10	23.19	23.31	0.139
24	40000	188.5	30	0.10	25.05	25.16	0.339

Table 5. Design of experiments on H13 and outputs.

For the tests, two samples of H13 steel (size 25x25x12 mm) have been screwed on the Kistler Microdynamometer 9317b in order to acquire the forces during the cutting

operations. Each sample has been flattened before doing the test; 12 tests have been performed on each sample for a total of 24 (the part program is in the Appendix A). The aim of this experimentation is to investigate which are the best values of each parameter to guarantee the best regular structure; the replicates could also help in understanding if the interactions between the factors are significant or not. As output, it has been considered the RMS planar force F_{xy} , the RMS of the total force F_{tot} and the surface roughness S_a . At the end of this campaign the value of each parameter will be selected for machining the inserts for injection moulding.

6.2.1 Response variable: F_{xy}

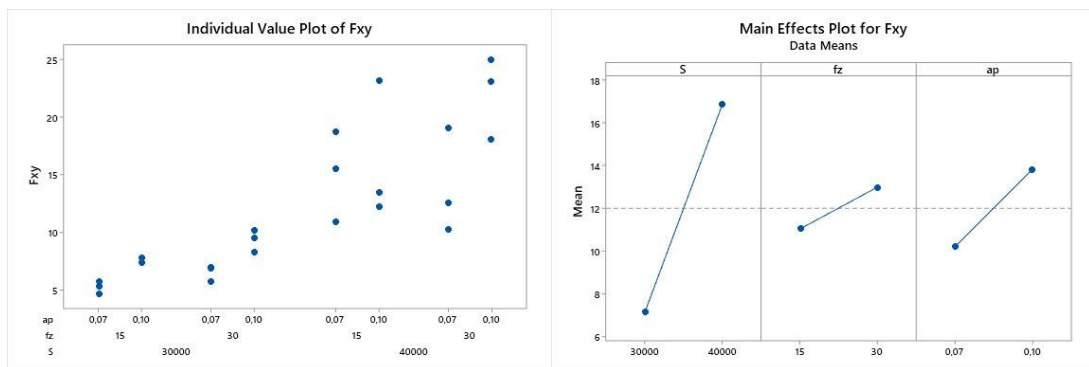


Figure 76. (a) individual value plot for F_{xy} , (b) main effect plot for F_{xy} , extended tests on H13.

The individual value plot indicates that no evident outliers appear and the variability among the factor levels appears uniform, Figure 76(a). The factors cutting speed and depth of cut seem to be more relevant than feed per tooth, Figure 76(b).

Now, since there are 3 replicas for each condition, it's possible to consider also the interactions between factors, Figure 77.

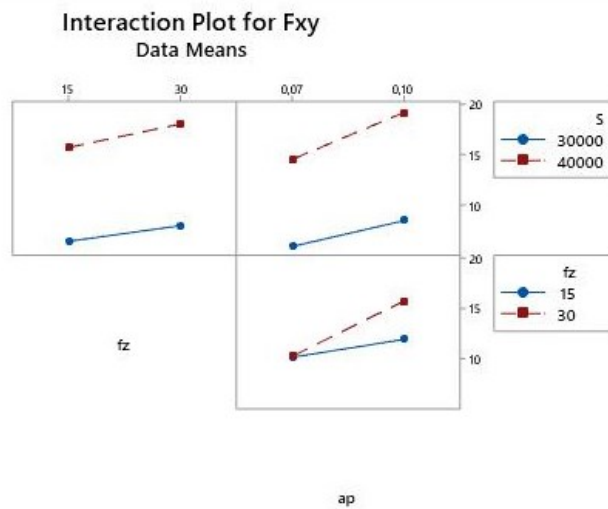


Figure 77. Interaction plot for Fxy, extended tests on H13.

The interaction plot for Fxy shows that the interactions between the cutting speed and the other two factors is not significant, since the lines are parallel one to each other, while the interaction between fz and ap seems to be significant, but a deeper analysis is necessary to bring some conclusions.

General linear model

Factor Information

Factor	Type	Levels	Values
S	Fixed	2	30000; 40000
fz	Fixed	2	15; 30
ap	Fixed	2	0.07; 0.10

Analysis of Variance

Source	DF	Adj SS	Adj MS	F-Value	P-Value
S	1	568.032	568.032	52.35	0.000
fz	1	22.807	22.807	2.10	0.166
ap	1	78.650	78.650	7.25	0.016
S*fz	1	0.901	0.901	0.08	0.777
S*ap	1	6.675	6.675	0.62	0.444
fz*ap	1	20.576	20.576	1.90	0.187
S*fz*ap	1	15.144	15.144	1.40	0.255
Error	16	173.609	10.851		
Total	23	886.393			

Model Summary

S	R-sq	R-sq(adj)	R-sq(pred)
3.29402	80.41%	71.85%	55.93%

From the ANOVA table the factors cutting speed and depth of cut have p values lower than 0.05, while feed per tooth has a low p-value, but higher than 0.05. Also, the interactions are not significant, but the interaction $fz*ap$ has a low p-value and this fact should be kept in consideration. But before concluding it's necessary to check the assumptions for standardized residuals and normality first.

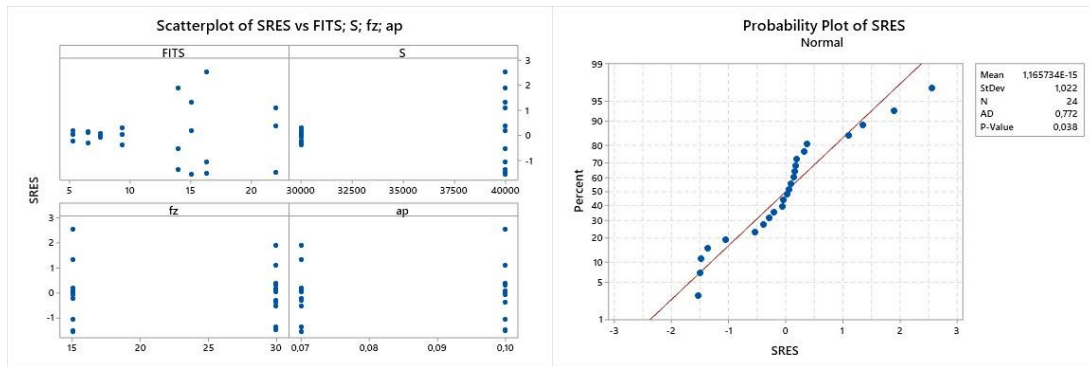


Figure 78. (a) scatterplot for F_{xy} of SRES vs FITS; S; fz; ap, (b) probability plot of SRES, extended tests on H13.

The scatterplots indicate that no evident outliers appear, all the standardized residuals in fact belong to the interval $(-3; +3)$. The normality hypothesis cannot be rejected (even with a very small p-value), Figure 78. If the model is reduced not considering the interactions between factors, the normality assumption would not be rejected with a higher p-value, Figure 79.

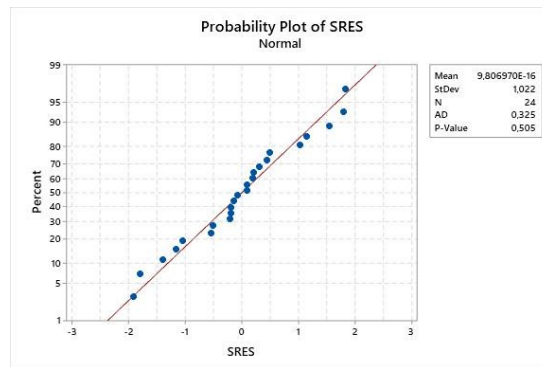


Figure 79. Probability plot of SRES of the reduced model, extended tests on H13.

Comparisons

- Tukey Pairwise Comparisons: cutting speed

Grouping Information Using the Tukey Method and 95% Confidence

S	N	Mean	Grouping
40000	12	16.8652	A
30000	12	7.1353	B

- Tukey Pairwise Comparisons: depth of cut

Grouping Information Using the Tukey Method and 95% Confidence

ap	N	Mean	Grouping
0.10	12	13.8105	A
0.07	12	10.1900	B

Through this deeper analysis on the RMS of the planar force F_{xy} , it's possible to conclude that the factors that have influence on its value are the cutting speed and the depth of cut, but also the feed per tooth and the interaction between feed and depth of cut should be taken under control, because presents a p-value not so far from 0.05. From the comparisons it's possible to see that higher values of planar forces are generated when cutting is done considering the highest level of cutting speed and depth of cut. By looking at the model of tool with finite stiffness, it is important to increase the cutting force in order to generate a deflection able to guarantee that the rear tooth doesn't touch the already machined surface, avoiding the damaging of it.

6.2.2 Response variable: Ftot

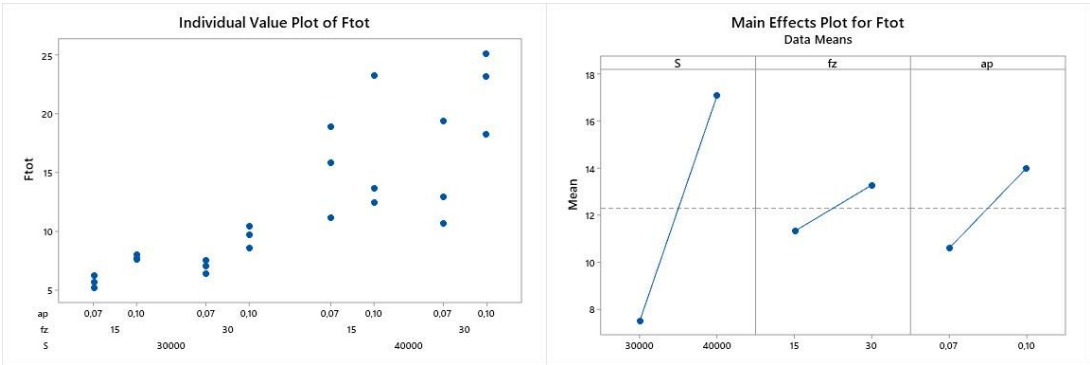


Figure 80. (a) individual value plot for Ftot, (b) main effect plot for Ftot, extended tests on H13.

The individual value plot indicates that no evident outliers appear and the variability among the factor levels appears uniform, Figure 80(a). The factors cutting speed and depth of cut seem to be more relevant than feed per tooth, Figure 80(b).

Now, since there are 3 replicas for each condition, it's possible to consider also the interactions between factors, Figure 81.

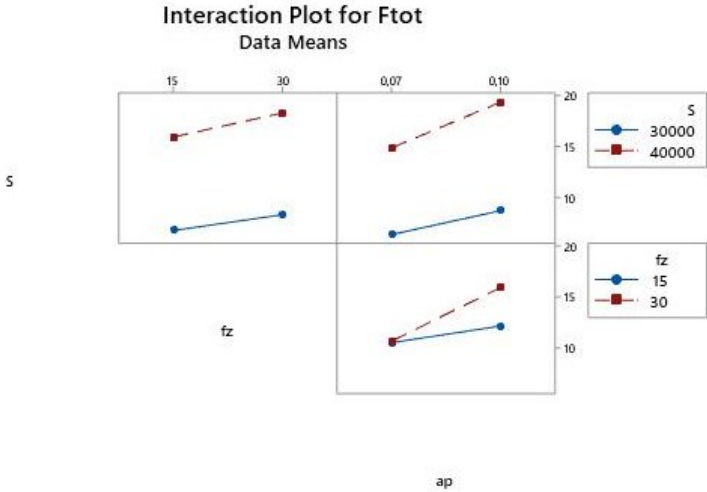


Figure 81. Interaction plot for Ftot, extended tests on H13.

The interaction plot for Ftot shows the same results obtained for Fxy.

General linear model

Factor Information

Factor	Type	Levels	Values
S	Fixed	2	30000; 40000
fz	Fixed	2	15; 30
ap	Fixed	2	0.07; 0.10

Analysis of Variance

Source	DF	Adj SS	Adj MS	F-Value	P-Value
S	1	553.526	553.526	52.05	0.000
fz	1	23.089	23.089	2.17	0.160
ap	1	70.383	70.383	6.62	0.020
S*fz	1	0.991	0.991	0.09	0.764
S*ap	1	6.968	6.968	0.66	0.430
fz*ap	1	19.552	19.552	1.84	0.194
S*fz*ap	1	14.021	14.021	1.32	0.268
Error	16	170.151	10.634		
Total	23	858.680			

Model Summary

S	R-sq	R-sq(adj)	R-sq(pred)
3.26105	80.18%	71.52%	55.42%

From the ANOVA table the factors cutting speed and depth of cut have p values lower than 0.05, while feed per tooth has a low p-value, but higher than 0.05. Also, the interactions are not significant, but the interaction fz*ap has a low p-value and this fact should be kept in consideration. But before concluding it's necessary to check the assumptions for standardized residuals and normality first.

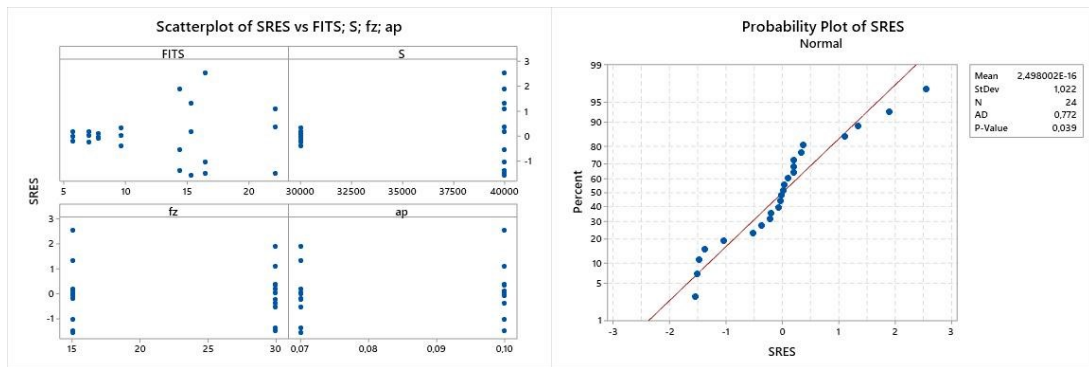


Figure 82. (a) scatterplot for Ftot of SRES vs FITS; S; fz; ap, (b) probability plot of SRES, extended tests on H13.

The scatterplots indicate that no evident outliers appear, all the standardized residuals in fact belong to the interval (-3; +3). The normality hypothesis cannot be rejected (even with a very small p-value), Figure 82. If the model is reduced not considering the interactions between factors, the normality assumption would not be rejected with a higher p-value, Figure 83.

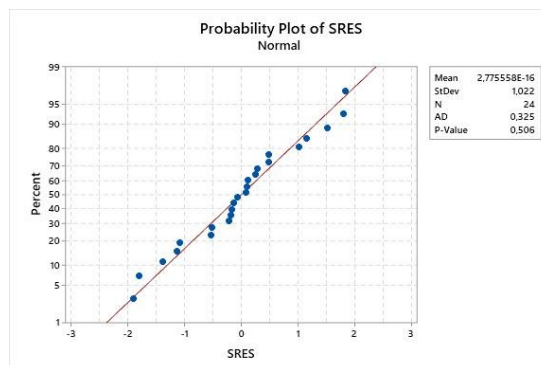


Figure 83. Probability plot of SRES of the reduced model, extended tests on H13.

Comparisons

- Tukey Pairwise Comparisons: cutting speed

Grouping Information Using the Tukey Method and 95% Confidence

S	N	Mean	Grouping
40000	12	17.0988	A
30000	12	7.4939	B

- Tukey Pairwise Comparisons: depth of cut

Grouping Information Using the Tukey Method and 95% Confidence

ap	N	Mean	Grouping
0,10	12	14.0089	A
0,07	12	10.5839	B

Through this deeper analysis on the RMS of the total force F_{tot} , it's possible to conclude that the factors that have influence on its value are the cutting speed and the depth of cut, but also the feed per tooth and the interaction between feed and depth of cut should be taken under control, because presents a p-value not so far from 0.05. From the comparisons it's possible to see that higher values of total forces are generated when cutting is done considering the highest level of cutting speed and depth of cut. The same considerations and the same results of the planar force case were obtained, since the contribution of the force in z is very small when compared with the forces in the other two directions.

6.2.3 Response variable: S_a

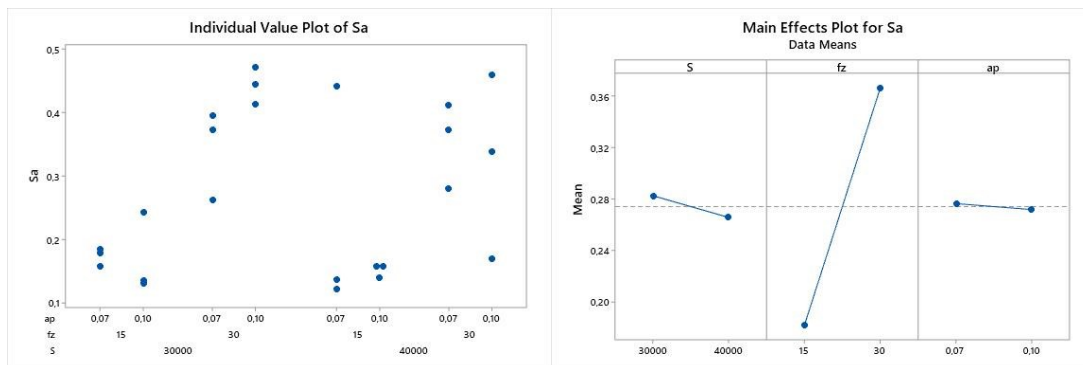


Figure 84. (a) individual value plot for S_a , (b) main effect plot for S_a , extended tests on H13.

The individual value plot indicates that no evident outliers appear and the variability among the factor levels appears uniform, Figure 84(a). The factor feed per tooth seems to be more relevant than the other two, Figure 84(b).

Now, since there are 3 replicas for each condition, it's possible to consider also the interactions between factors, Figure 85.

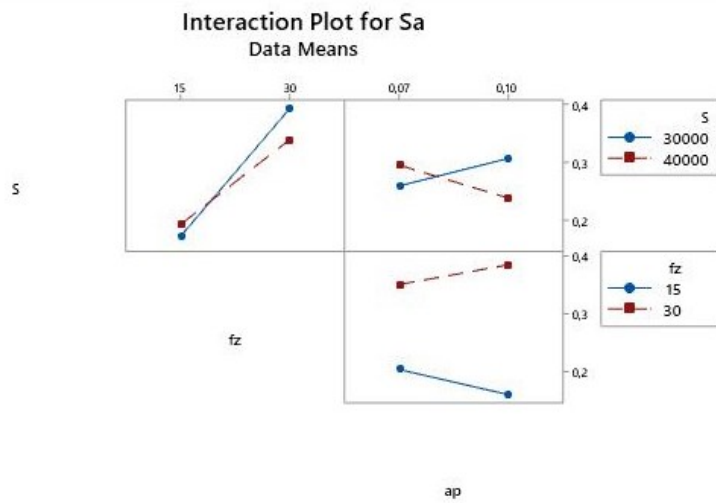


Figure 85. Interaction plot for Sa, extended tests on H13.

The interaction plot for Sa shows that the interactions between the cutting speed and the other two factors seem to be significant, since the lines cross each other, while the interaction between fz and ap is not significant, but a deeper analysis is necessary to bring some conclusions.

General linear model

Factor Information

Factor	Type	Levels Values
S	Fixed	2 30000; 40000
fz	Fixed	2 15; 30
ap	Fixed	2 0.07; 0.10

Analysis of Variance

Source	DF	Adj SS	Adj MS	F-Value	P-Value
S	1	0.001700	0.001700	0.20	0.663
fz	1	0.204980	0.204980	23.73	0.000
ap	1	0.000131	0.000131	0.02	0.904
S*fz	1	0.008363	0.008363	0.97	0.340
S*ap	1	0.016537	0.016537	1.91	0.185
fz*ap	1	0.008894	0.008894	1.03	0.325
S*fz*ap	1	0.001121	0.001121	0.13	0.723
Error	16	0.138208	0.008638		
Total	23	0.379933			

Model Summary

S	R-sq	R-sq(adj)	R-sq(pred)
0.0929408	63.62%	47.71%	18.15%

From the ANOVA table the only factor with a p values lower than 0.05 is feed per tooth. Also, the interactions are not significant, since all the p values are higher than 0.05. But before concluding it's necessary to check the assumptions for standardized residuals and normality first.

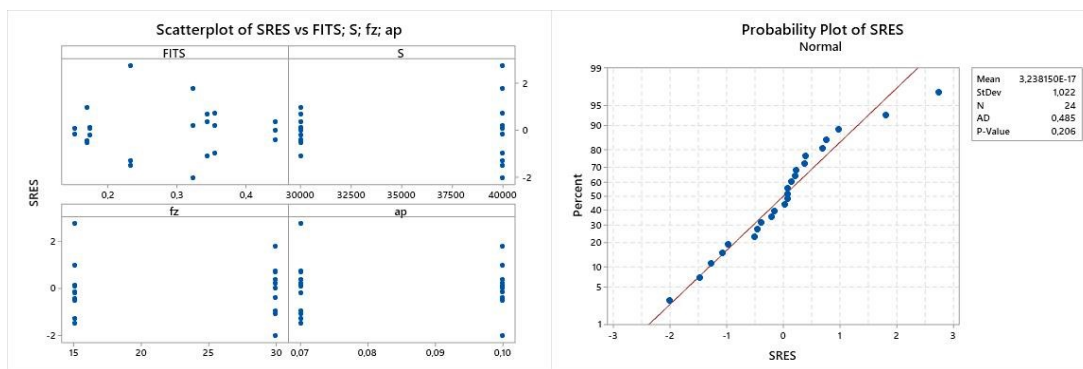


Figure 86. (a) scatterplot for Sa of SRES vs FITS; S; fz; ap, (b) probability plot of SRES, extended tests on H13.

The scatterplots indicate that no evident outliers appear, all the standardized residuals in fact belong to the interval (-3; +3). The normality hypothesis cannot be rejected, Figure 86.

Comparisons

- Tukey Pairwise Comparisons: feed per tooth

Grouping Information Using the Tukey Method and 95% Confidence

fz	N	Mean	Grouping
30	12	0.366583	A
15	12	0.181750	B

Through this deeper analysis on the surface roughness Sa, it's possible to conclude that the factor that has influence on its value is the feed per tooth. From the

comparisons it's possible to see that higher values of surface roughness are generated when cutting is done considering the highest level of feed.

6.2.4 Effect of the cutting parameters on regularity

After machining all the slots, each generated surface has been acquired using the Mahr MarSurf CWM 100 (magnification 50X, NA 0.60) to check the regularity of the profiles obtained and looking if the replicas present the same pattern, otherwise some troubles like tool wear or differences in the two samples could be present. Here is a summary with all the profiles obtained and the corresponding processing parameters:

- Cutting speed: 141.4 m/min (30000 rpm);
- Feed per tooth: 15 $\mu\text{m}/\text{tooth}$;
- Depth of cut: 0.07 mm

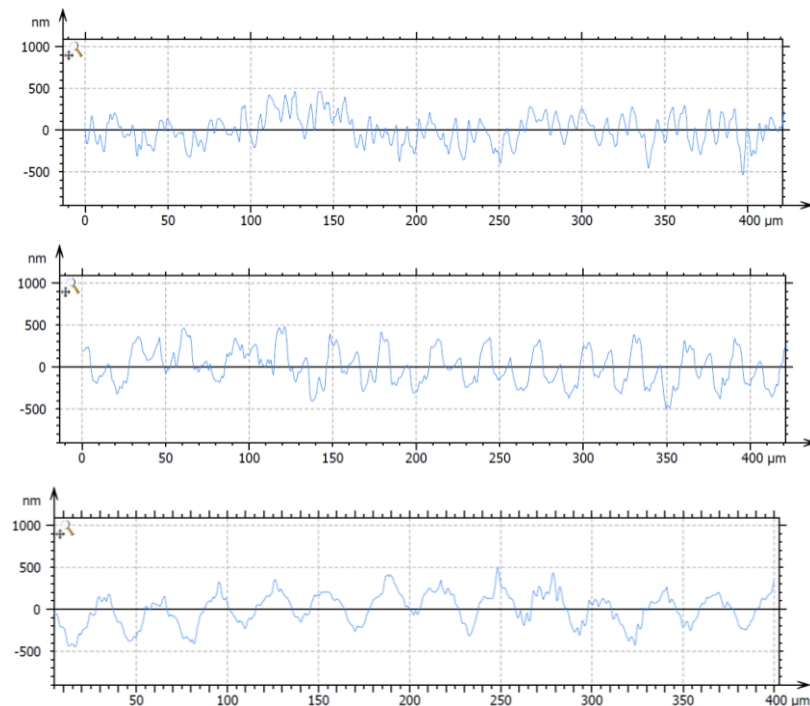


Figure 87. Extracted profile at $V_c=141.4$ m/min, $f_z= 15$ $\mu\text{m}/\text{tooth}$, $a_p=0.07$ mm (a) replica 1, (b) replica 2, (c) replica 3.

- Cutting speed: 141.4 m/min (30000 rpm);

- Feed per tooth: $30 \mu\text{m}/\text{tooth}$;
- Depth of cut: 0.07 mm

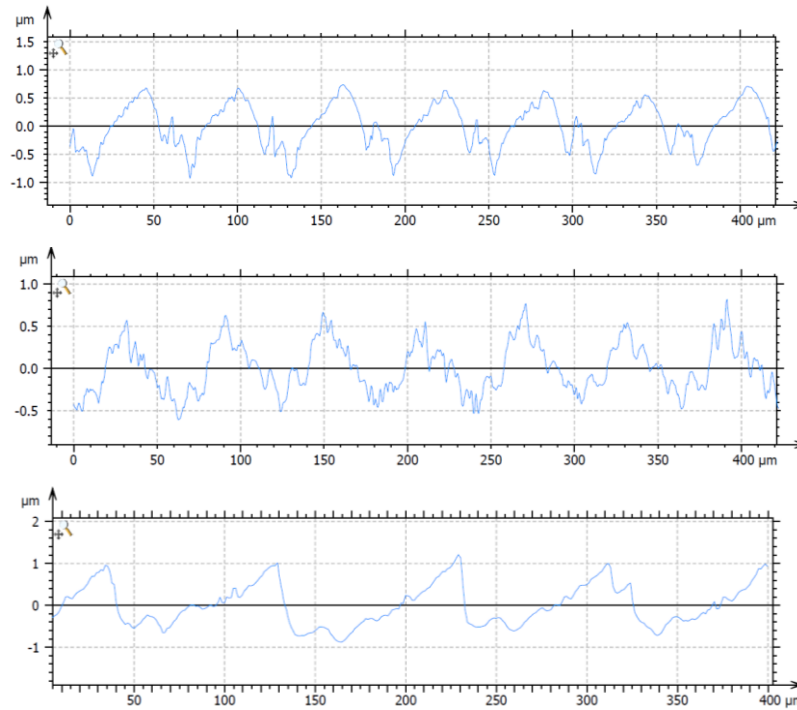
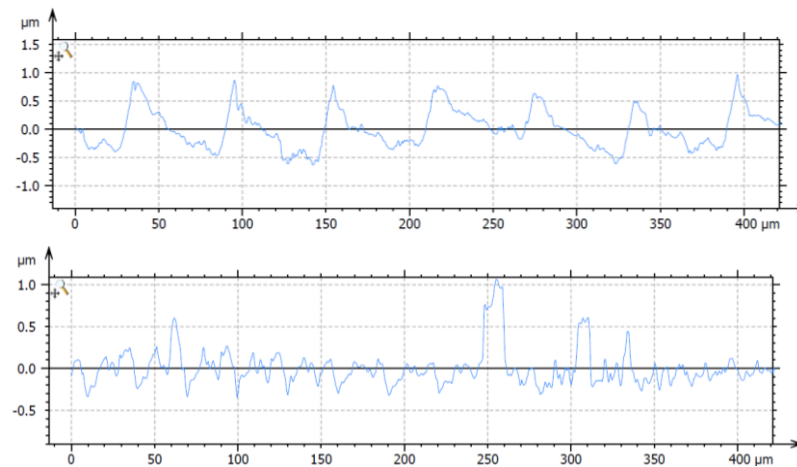


Figure 88. Extracted profile at $V_c=141.4 \text{ m/min}$, $f_z= 30 \mu\text{m}/\text{tooth}$, $a_p=0.07 \text{ mm}$ (a) replica 1, (b) replica 2, (c) replica 3.

- Cutting speed: 141.4 m/min (30000 rpm);
- Feed per tooth: $15 \mu\text{m}/\text{tooth}$;
- Depth of cut: 0.10 mm



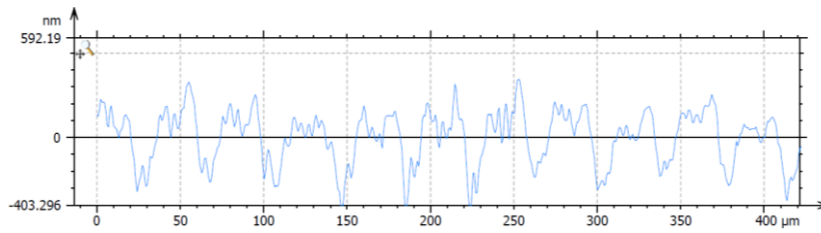


Figure 89. Extracted profile at $V_c=141.4$ m/min, $f_z= 15$ $\mu\text{m}/\text{tooth}$, $a_p=0.10$ mm (a) replica 1, (b) replica 2, (c) replica 3.

- Cutting speed: 141.4 m/min (30000 rpm);
- Feed per tooth: 30 $\mu\text{m}/\text{tooth}$;
- Depth of cut: 0.10 mm

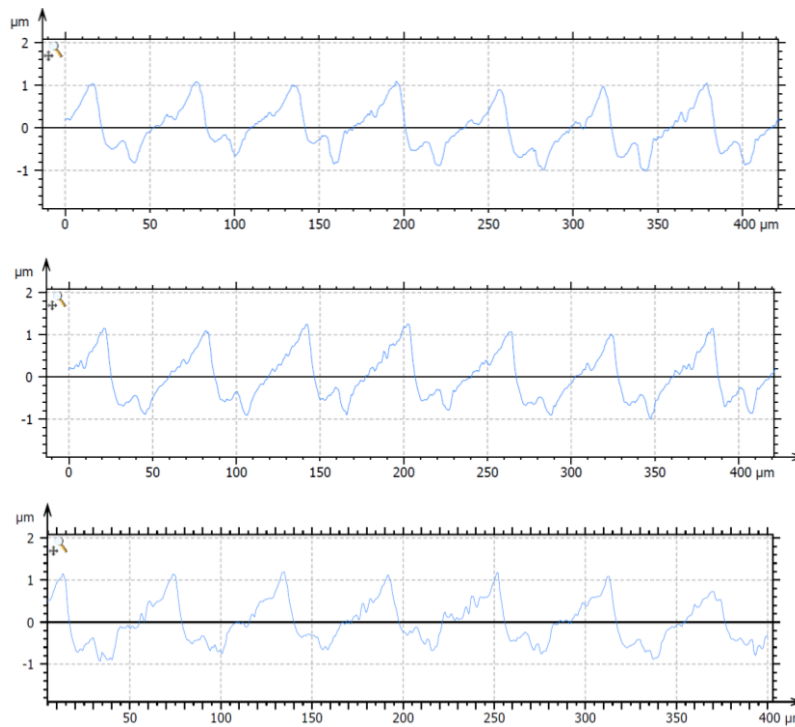


Figure 90. Extracted profile at $V_c=141.4$ m/min, $f_z= 30$ $\mu\text{m}/\text{tooth}$, $a_p=0.10$ mm (a) replica 1, (b) replica 2, (c) replica 3.

- Cutting speed: 188.5 m/min (40000 rpm);
- Feed per tooth: 15 $\mu\text{m}/\text{tooth}$;
- Depth of cut: 0.07 mm

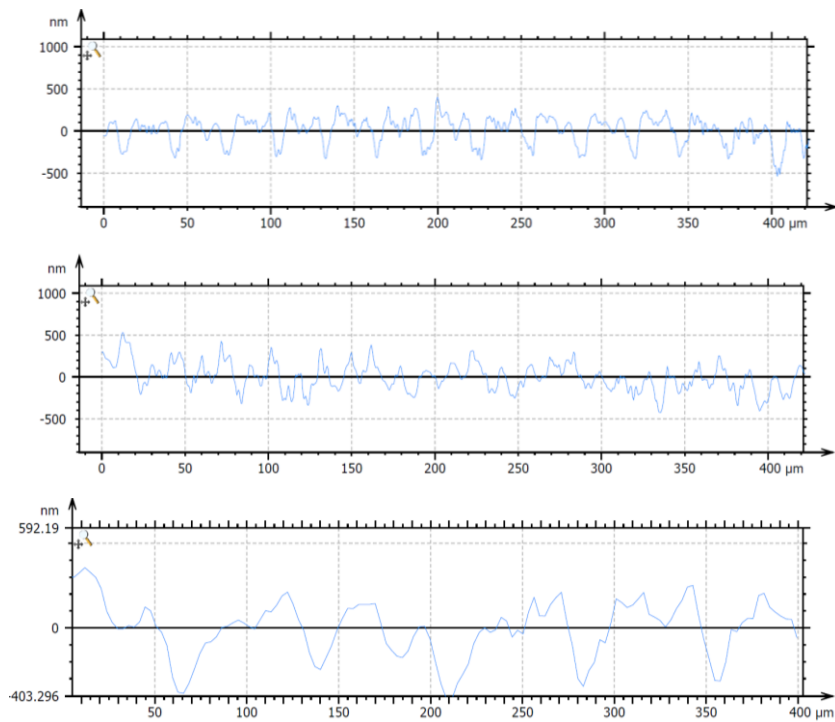
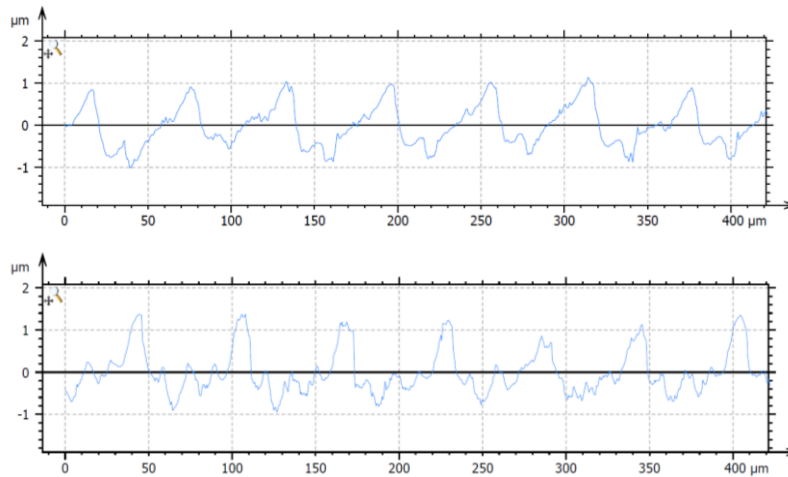


Figure 91. Extracted profile at $V_c=188.5$ m/min, $f_z= 15$ $\mu\text{m}/\text{tooth}$, $a_p=0.07$ mm (a) replica 1, (b) replica 2, (c) replica 3.

- Cutting speed: 188.5 m/min (40000 rpm);
- Feed per tooth: 30 $\mu\text{m}/\text{tooth}$;
- Depth of cut: 0.07 mm



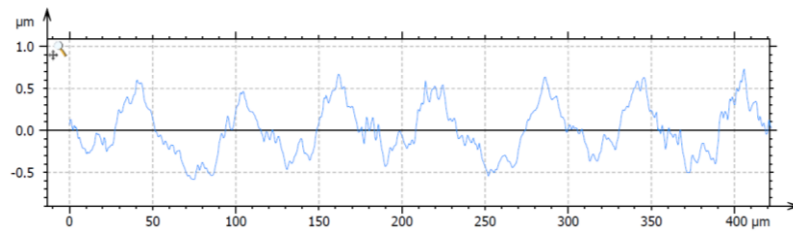


Figure 92. Extracted profile at $V_c=188.5$ m/min, $f_z= 30$ $\mu\text{m}/\text{tooth}$, $a_p=0.07$ mm (a) replica 1, (b) replica 2, (c) replica 3.

- Cutting speed: 188.5 m/min (40000 rpm);
- Feed per tooth: 15 $\mu\text{m}/\text{tooth}$;
- Depth of cut: 0.10 mm

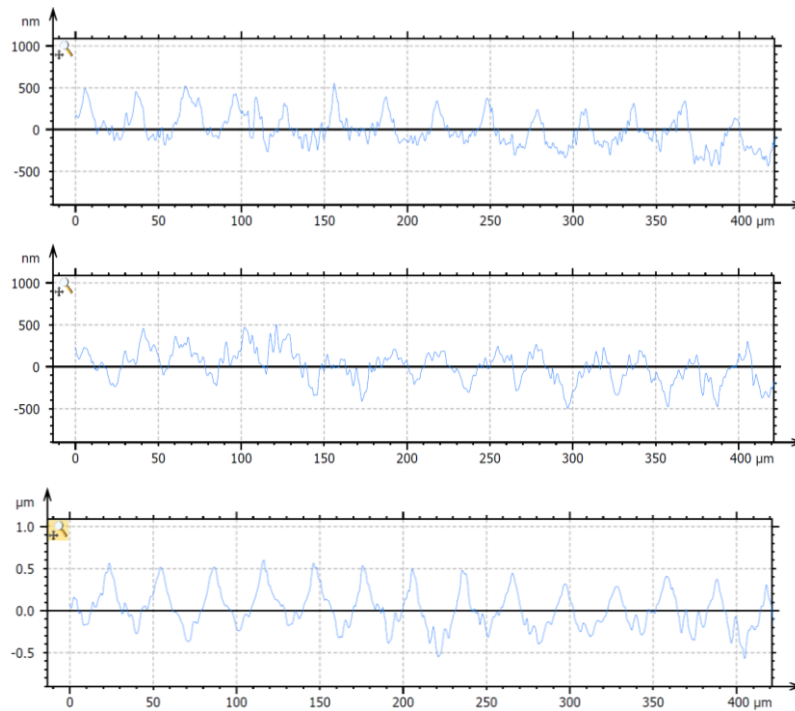


Figure 93. Extracted profile at $V_c=188.5$ m/min, $f_z= 15$ $\mu\text{m}/\text{tooth}$, $a_p=0.10$ mm (a) replica 1, (b) replica 2, (c) replica 3.

- Cutting speed: 188.5 m/min (40000 rpm);
- Feed per tooth: 30 $\mu\text{m}/\text{tooth}$;
- Depth of cut: 0.10 mm

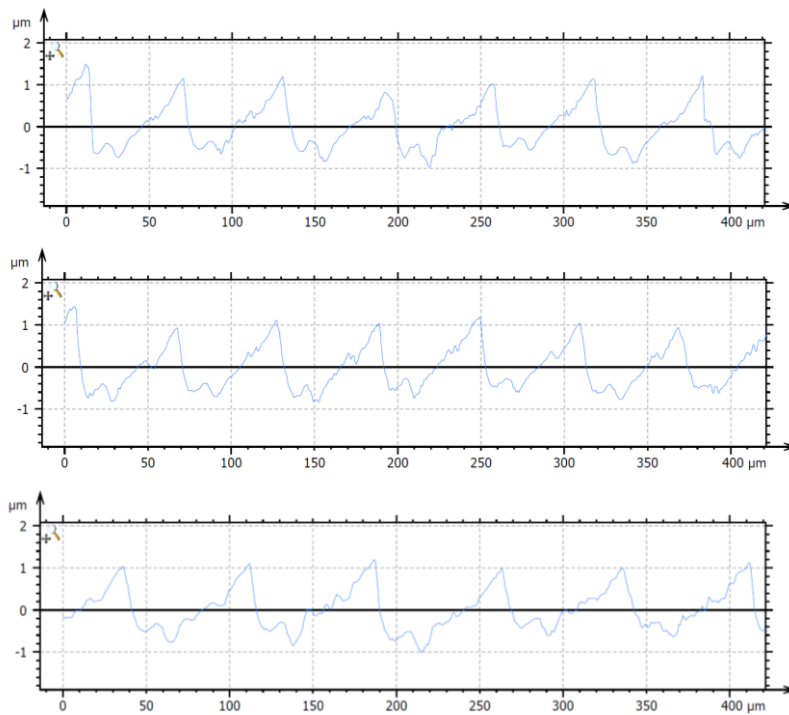


Figure 94. Extracted profile at $V_c=188.5$ m/min, $f_z= 30$ $\mu\text{m}/\text{tooth}$, $a_p=0.10$ mm (a) replica 1, (b) replica 2, (c) replica 3.

It is possible to note that lower the feed per tooth values lead to lower values of surface roughness, but having to study the regularity of the surface, the cases with the feed per tooth equal to $30 \mu\text{m}$ are those able to generate more regular surfaces. This is related to the phenomenon of tool deflection, in turn linked to the value of the cutting force during slotting operation. In order to guarantee a deflection and therefore a greater force, the higher feed was able to do this. Looking at the various profiles, it is also possible to observe the run-out phenomenon: the alternation of a higher peak and a lower one within a period (i.e. a tool revolution) is clearly evident. The case in which the run-out is less than the feed has occurred (case 2 paragraph 5.2), so both teeth of the tool are able to cut, but in different ways, leaving different traces on the surface of the workpiece.

6.2.5 Selection of the values for each working parameter

Once the experimental campaign has completed and having analyzed the impact of factors on forces, surface roughness and regularity of the profiles obtained, it is possible to select the values to be attributed to each parameter in order to machine the surface of the insert from injection moulding, to obtain a regular structure that acts as a diffraction grating for the light, as requested. These values will be used in the part program as process values, since they have been the best to obtain the most regular profile:

- Cutting speed: 188.5 m/min (40000 rpm);
- Feed per tooth: 30 μm /tooth;
- Depth of cut: 0.100 mm

6.3 Evaluation of the overlap on H13 steel

Before starting to machine the surface of the inserts for injection moulding, another short experiment was performed in order to test the quality of the profiles obtained through the overlapping of the slots obtained during the passage of the tool, a method already tested by Baruffi et Al. [30]. Since the tool used has a diameter of 1.5 mm, the width of each cut is fixed by this parameter, therefore the only way to increase this width is to proceed through the parallel overlapping of the slots. These tests are done because the request is to obtain a diffraction grating at least 4 mm wide on the inserts. Using a sample of H13 of 25x25x12 mm size, different percentage of overlap was tested, using the same 1.5 mm tool, with the optimal values of the process parameters obtained from the previous experimentation.

The four conditions that have been tested are:

- 0% (no overlap condition)
- 10%
- 40%
- 70%

The part program for generating the overlap is reported in the Appendix A.

6.3.1 Overlap: 0%

For this test, 4 slots have been realized in parallel. Since the overlap is 0%, so an extreme case in which there is no overlap, the distance between one cut and the next is 1.5 mm, for a total width of 6 mm. The following images are taken from the Mahr MarSurf CWM 100 (magnification 50X, NA 0.60), the surface and an extracted profile are shown, in which the regularity can be analysed, Figure 95.

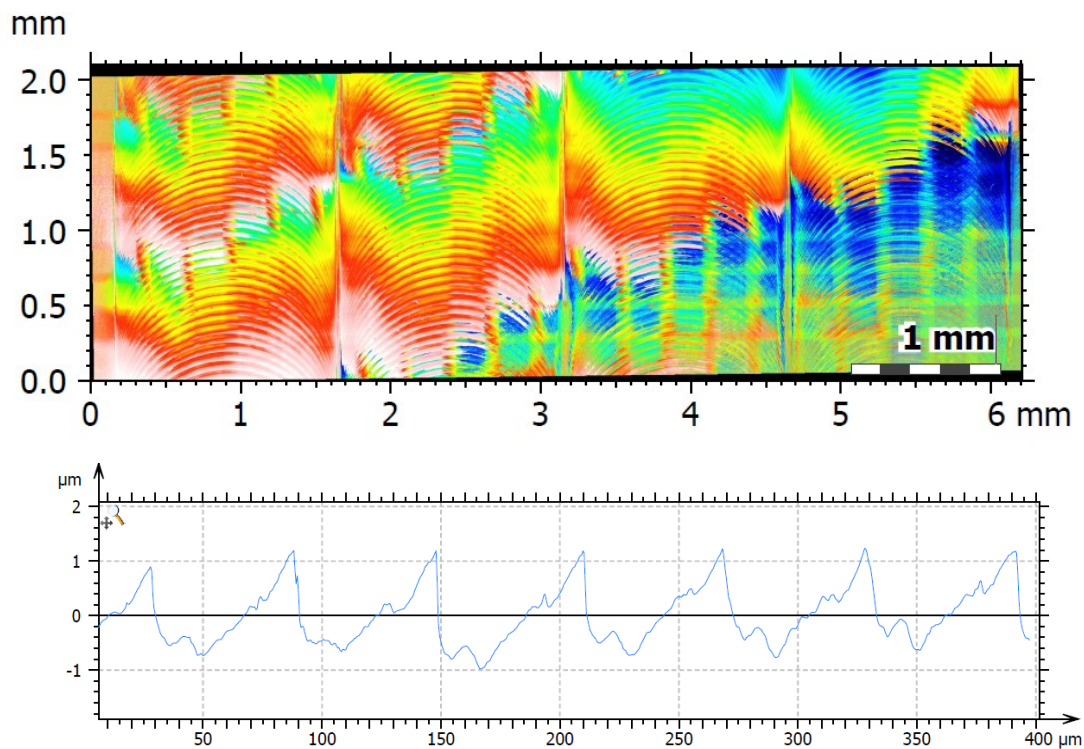


Figure 95. (a) extracted area, (b) extracted profile at 0% overlap.

The regularity of the profile of each slot is quite good, but between the two slots, by extracting the area, it's possible to see that there is minute disruption; this can be reduced with an increase of the overlap percentage.

6.3.2 Overlap: 10%

For this test, 4 slots have been realized in parallel. Since the overlap is 10%, the distance between one cut and the next is 0.9 mm, for a total width of 4.2 mm. The following images are taken from the Mahr MarSurf CWM 100 (magnification 50X, NA 0.60), the surface and an extracted profile are shown, in which the regularity can be analysed, Figure 96.

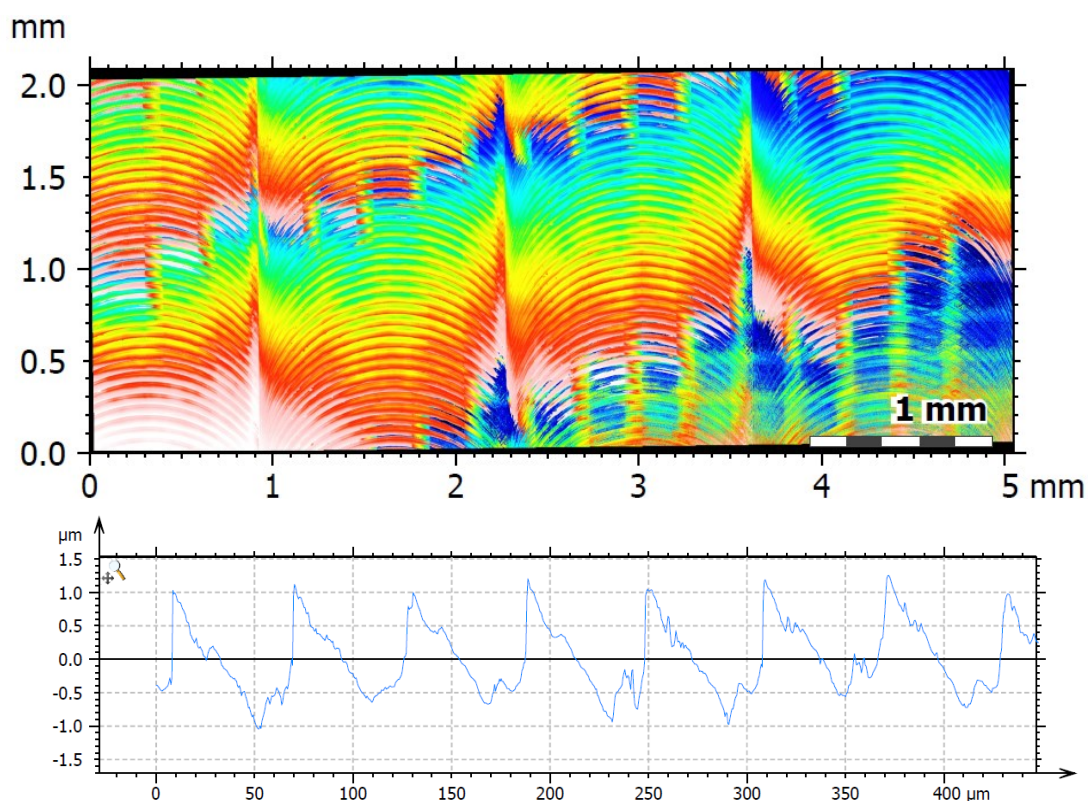


Figure 96. (a) extracted area, (b) extracted profile at 10% overlap.

By increasing the overlap between the two slots, disruption between them decreases and individual profiles of each slot are same as the previous case because the machining parameters used are the same.

6.3.3 Overlap: 40%

For this test, 4 slots have been realized in parallel. Since the overlap is 40%, the distance between one cut and the next is 1.35 mm, for a total width of 5.55 mm. The

following images are taken from the Mahr MarSurf CWM 100 (magnification 50X, NA 0.60), the surface and an extracted profile are shown, in which the regularity can be analysed, Figure 97.

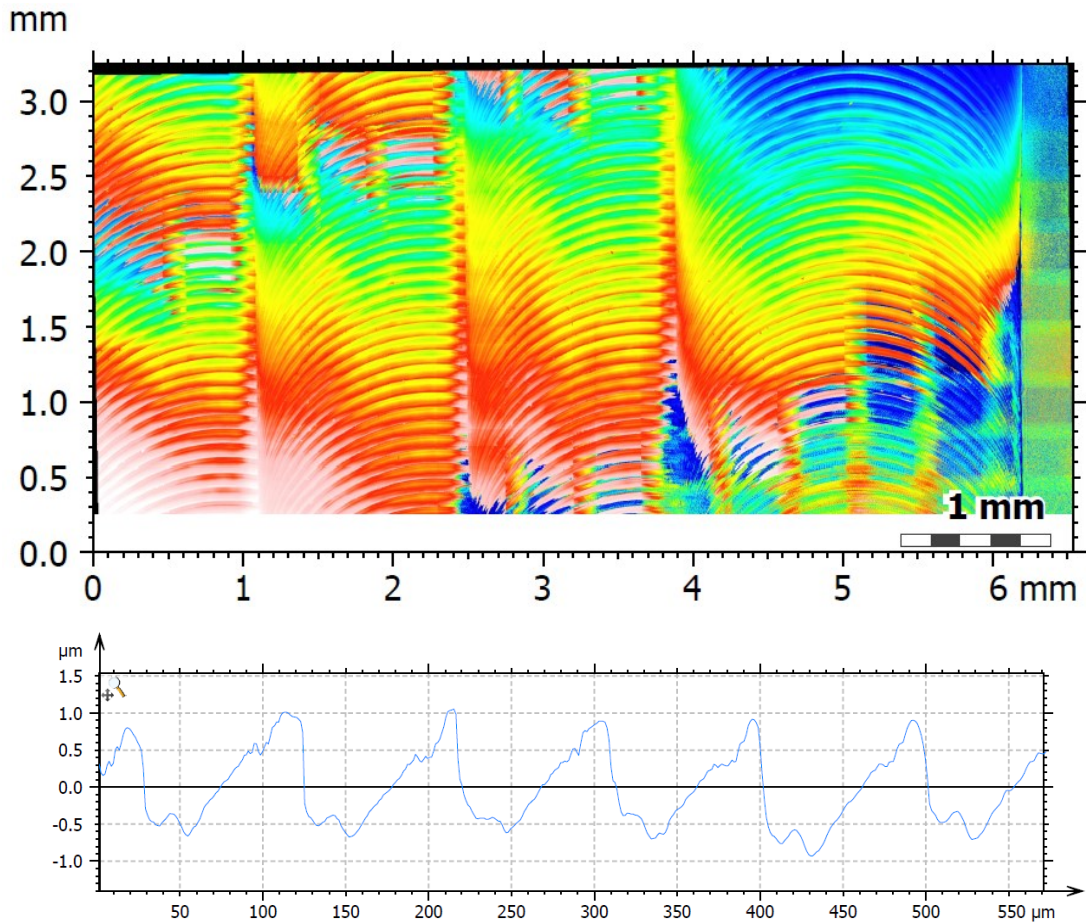


Figure 97. (a) extracted area, (b) extracted profile at 40% overlap.

In this case, increasing the overlap percentage to 40%, it is clearly shown in the extracted area that tool over runs the previous slot and this will affect the regularity of the surface.

6.3.4 Overlap: 70%

For this test, 4 slots have been realized in parallel. Since the overlap is 70%, the distance between one cut and the next is 0.45 mm, for a total width of 2.85 mm. The following images are taken from the Mahr MarSurf CWM 100 (magnification 50X, NA

0.60), the surface and an extracted profile are shown, in which the regularity can be analysed, Figure 98.

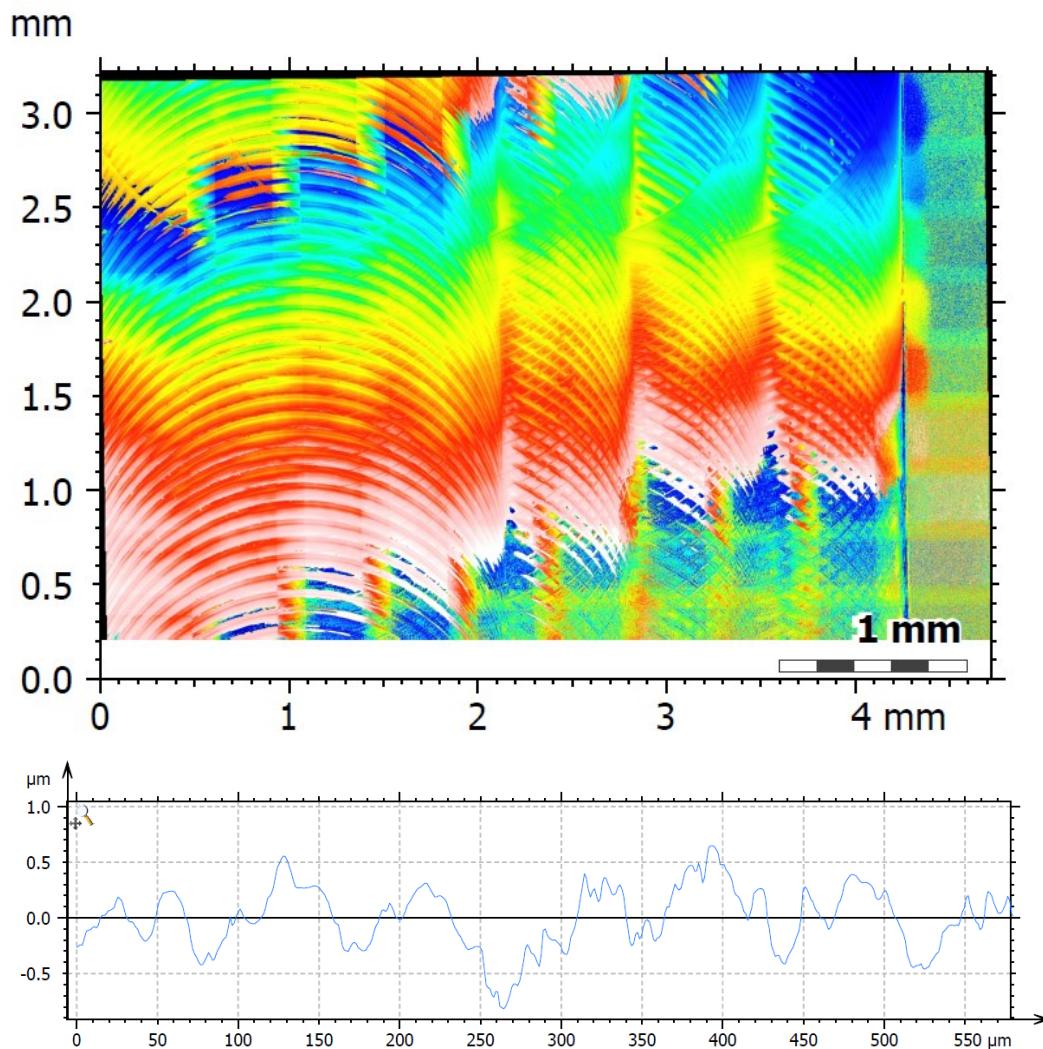


Figure 98. (a) extracted area, (b) extracted profile at 70% overlap.

In this case, as the overlap percentage is increased to 70%, regularity of profile is further disturbed as tool over run the profile again. There is another phenomenon that did not occur previously, that is the presence of the rear tooth which damages the surface just worked. This fact is probably due to the fact that the radial depth of cut is smaller, generating a lower force which causes the tool to be deflected less during cutting. Overall, this is the worst surface obtained analyzing the various cases of overlap.

6.3.5 Selection of the value of overlap

Following the experimentation on the overlap, it emerged that the 0% overlap situation presents disruptions at the edges of each slot, a phenomenon that is preferable to avoid, while for rather high overlaps, i.e. 40% and 70%, some damages is noted on the texture generated by the previous tool cuts. The optimal choice therefore is to use overlapping slots in parallel at almost 10%, as they have a good compromise on the regularity of the profiles and do not presents disruptions at the edges. The 10% overlap, combined with the cutting parameters selected in the previous paragraph, allow defining all the process parameter that will be used for machining the inserts for injection moulding.

6.4 Machining of the Stavax ESR steel inserts

All the various experiments made previously have been necessary to better understand the phenomenon through which it is possible to realize a regular saw-tooth profile on steel for moulds, to generate a diffraction grating capable of reflecting light. Once the mechanism for generating this regular texture has been understood and optimized the various cutting and overlap parameters on H13 steel specimens, the goal is to machine the inserts for injection moulding in Uddeholm Stavax ERS steel in order to obtain the same regular saw-tooth profile. From the University of Bradford, UK, 4 inserts were sent, one of which as a test sample, so that the surface of the mould, i.e. the one that will be in contact with the material to be printed, was machined to recreate the diffraction grid. The surface has a circular area with a diameter of 5 mm, while the main body of the insert has a circular shape with a diameter of 15 mm.

6.4.1 Experiments on the test insert

Before starting the processing that will lead to the realization of the diffraction grating on the inserts for injection moulding, the effectiveness of the setup was tested, observing if there were problems of microvibrations or detachment of the piece during the working of the tool. Therefore, the first test performed was done with the optimal cutting parameters, creating 3 slots in parallel with 10% overlap, obtaining excellent results both from the point of view of the stability of the setup and from the point of view of the repetition of the profile already obtained from the previous experimentation.

Since the request was to process 3 inserts with parameters and possibly also different tools, different tests were performed at different cutting parameters using a coated hard metal tool, BFT, 4 mm, with 3 teeth, so as to realize a single 4 mm wide slot. The goal would have been to exploit the same deflection principle already had in the case of the 1.5 tool, so as to allow only the front teeth to perform the machining and leave their traces, keeping the rear part of the tool raised for avoid damaging the already machined surface. Not being able to measure forces, however, tests were carried out at very high cutting parameters, greater than the nominal values given by the catalog, without however obtaining good results: the phenomenon of rear teeth upset was clearly evident and also the high forces involved generate the phenomenon of microvibration, or chatter, on the insert being machined, compromising the success of the tests.

The second attempt was to work with a ramping in z, from a greater depth to a smaller one in order to avoid gouge, keeping the piece tilted. This strategy is the equivalent of the previous one, but instead of exploiting the deflection of the tool, it is the axis of the tool that has a certain relative inclination with respect to the piece being machined, precisely through the imposition of a certain inclination on the piece when it is mounted in the clamp. This would have meant avoiding the effect of the rear tooth which damages the surface obtained. Even in this case, however, the

results have not been satisfactory, since a profile has been obtained in which the depth of cut is difficult to control and therefore not constant, therefore a sloping profile, and the various traces generated by the passage of the tool have a step-like structure, so they do not suited to what is required.

Observing the results obtained with these two strategies that are equivalent, exploiting two different mechanisms, as the deflection of the tool in the first case, while the inclination of the piece in the second case, it emerged that to obtain the desired regular profile was necessary a 5-axis machine with the B-axis (axis referred to the rotation around Y-axis) on the head and not on the piece-holder table. This solution is explained in the paragraph 5.1.

After several attempts on the test insert adopting both strategies, the decision was to abandon the use of the 4 mm tool and also machine the remaining inserts with the 1.5 tool, varying the cutting parameters.

6.4.2 Cutting parameters for machining the inserts

Since the decision was to process all the inserts using the same $\varnothing 1.5$ mm tool, in order to maintain a constant force acting on the tool during cutting to ensure the same deflection and thus avoid the rear tooth upset phenomenon, it was decided to vary the parameters of cuts such as depth of cut and feed per tooth, keeping the cutting speed constant.

Starting from this last equation of the cutting force (see paragraph 5.3), it is possible to obtain the values of depth of cut, imposing the desired feed per tooth and a λ equal to 0.2, obtaining: depth of cut of 0.140 mm, imposing a feed per tooth of 20 $\mu\text{m}/\text{tooth}$ and depth of cut of 0.200 mm, imposing a feed per tooth of 12 $\mu\text{m}/\text{tooth}$;

Thus, summarizing the various cutting parameters for each insert:

- Insert A: $V_c=188.5$ m/min (40000 rpm), $f_z=30$ $\mu\text{m}/\text{tooth}$, $a_p=0.100$ mm;
- Insert B: $V_c=188.5$ m/min (40000 rpm), $f_z=20$ $\mu\text{m}/\text{tooth}$, $a_p=0.140$ mm;
- Insert C: $V_c=188.5$ m/min (40000 rpm), $f_z=12$ $\mu\text{m}/\text{tooth}$, $a_p=0.200$ mm;

All the inserts present 3 slots with an overlap of 10%.

6.4.3 Machining of the inserts

Insert A

Process parameters:

- Cutting speed: 188.5 m/min (40000 rpm)
- Feed per tooth: 30 $\mu\text{m}/\text{tooth}$
- Depth of cut: 0.100 mm
- Overlap: 10%
- Total width: 4.2 mm (3 slots)

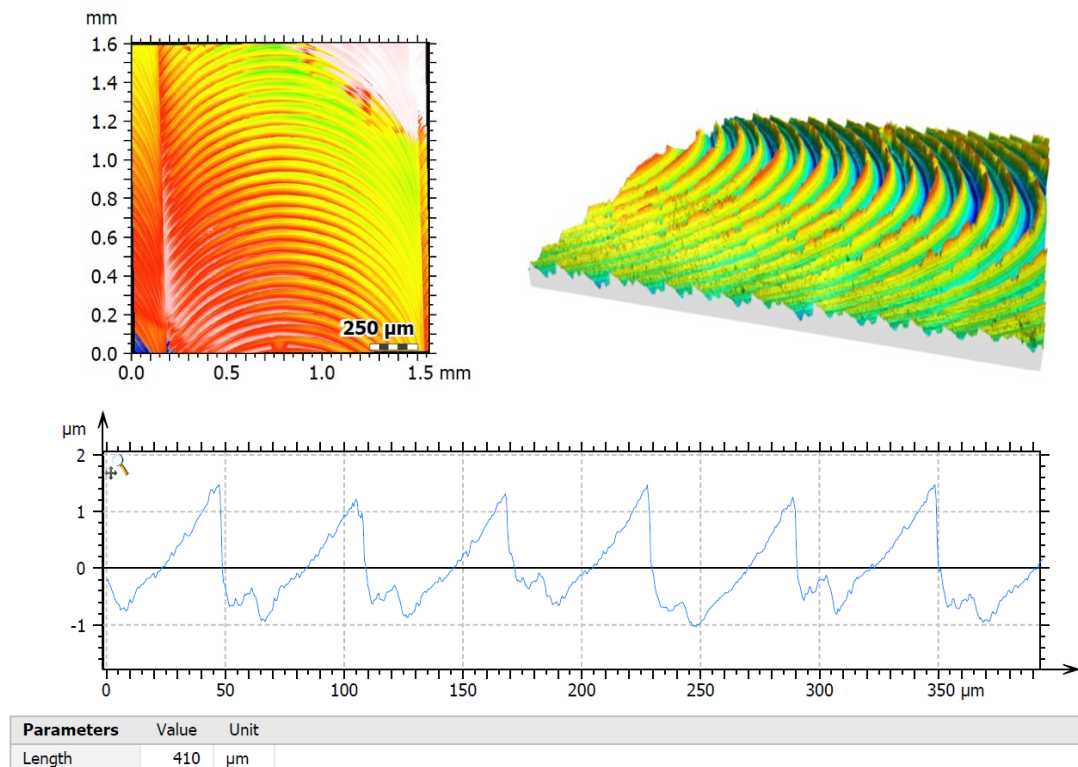


Figure 99. (a) extracted area, (b) 3D extracted area, (c) extracted profile for Insert A.

The insert A has the desired saw-tooth profile, just as already obtained in the previous experiments, it has a peak-valley distance of about 2 μm and the effect of the run-out is well evident if a period of 60 μm is considered, that is equal to twice the feed per tooth: in a period it's possible to see the presence of a peak much higher than the next one, due to the fact that the two teeth do not work in the same way.

Insert B

Process parameters:

- Cutting speed: 188.5 m/min (40000 rpm)
- Feed per tooth: 20 $\mu\text{m}/\text{tooth}$
- Depth of cut: 0.140 mm
- Overlap: 10%
- Total width: 4.2 mm (3 slots)

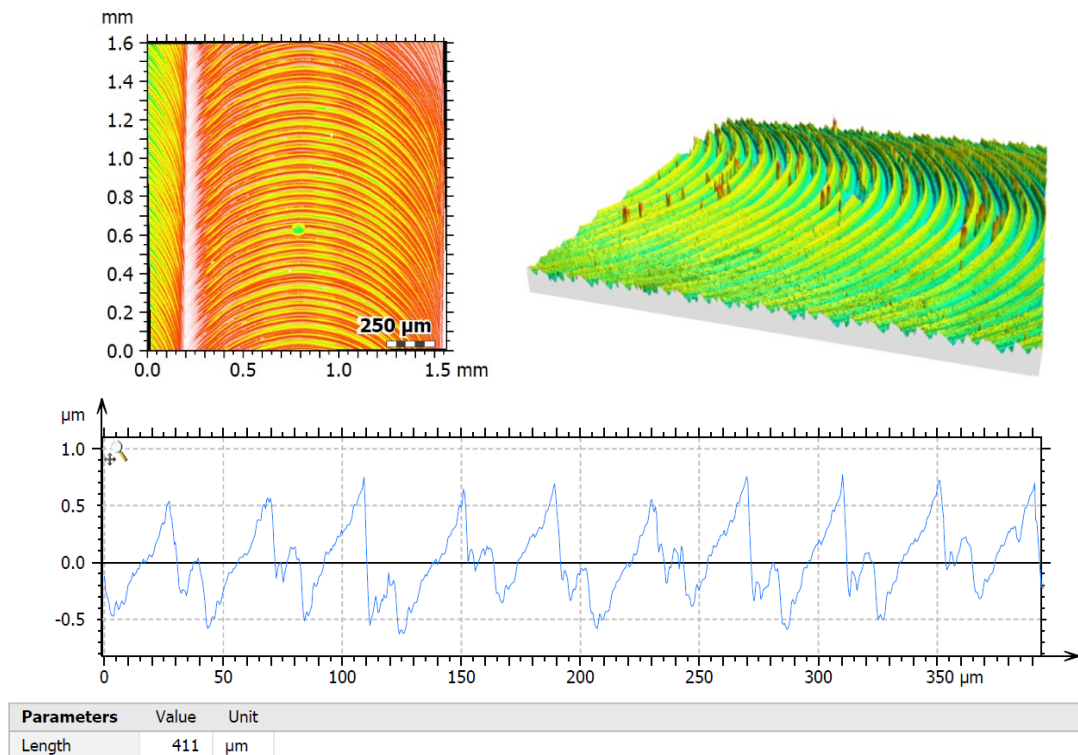


Figure 100. (a) extracted area, (b) 3D extracted area, (c) extracted profile for Insert B.

Also the insert B has the desired saw-tooth profile, it has a peak-valley distance of about 1 μm and the effect of the run-out is well evident if a period of 40 μm is considered, like for insert A. The picture of the 3D extracted area presents sudden peaks, due to the presence of parts of cut material that is difficult to eliminate.

Insert C

Process parameters:

- Cutting speed: 188.5 m/min (40000 rpm)
- Feed per tooth: 12 $\mu\text{m}/\text{tooth}$
- Depth of cut: 0.200 mm
- Overlap: 10%
- Total width: 4.2 mm (3 slots)

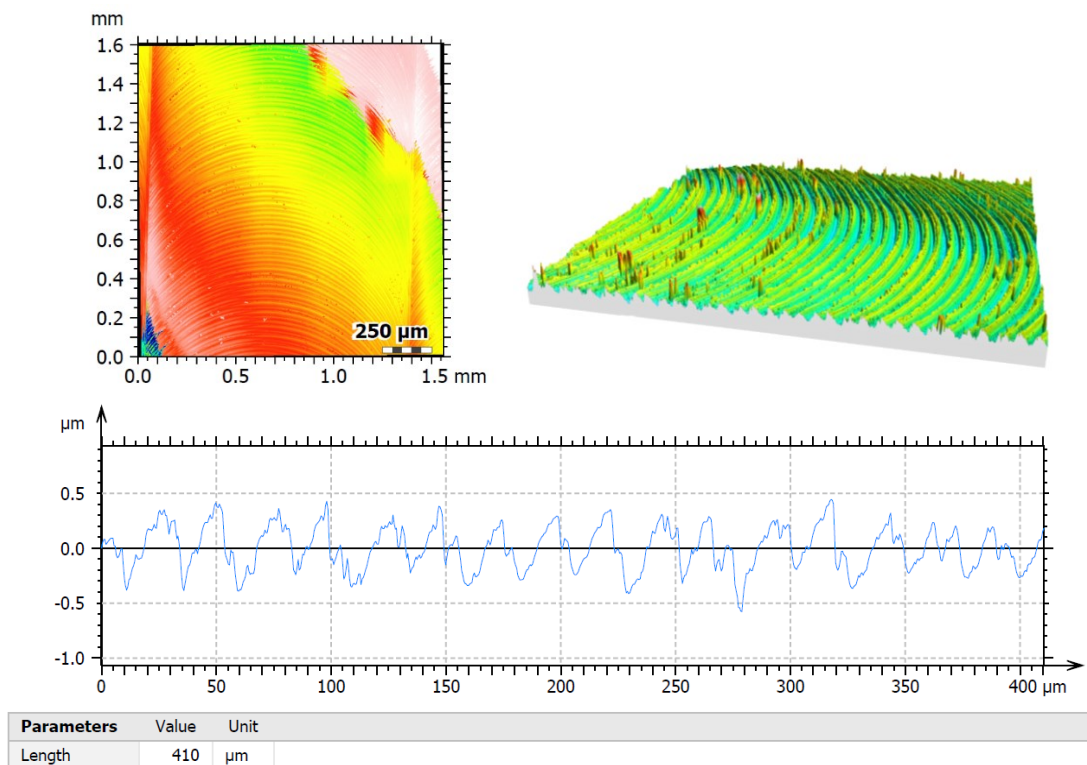


Figure 101. (a) extracted area, (b) 3D extracted area, (c) extracted profile for Insert C.

The insert C has the desired saw-tooth profile, it has a peak-valley distance lower than 1 μm and the effect of the run-out is also evident in this case. This is the case in which the run-out is higher than the feed per tooth (case 3 paragraph 5.2): only one of the two teeth cut the material generating a regular structure with peak at a distance of around 24 μm from each other, as clearly shown by Figure 101(c). Like for insert B, the picture of the 3D extracted area presents sudden peaks, due to the presence of parts of cut material that is difficult to eliminate.

7. CASE STUDY 2: EXPERIMENTS

7.1 Previous experiments

The study and experimentation on electroless-plated NiP steel in order to realize optical profiles for injection moulding was done in collaboration with the University of Padua [31]. A first experimentation was achieved in Padua: initially optimization experiments were conducted, they that consists in slotting operations carried out on the flat insert with two types of $\varnothing 0.3$ mm flat-end mills (FEM): coated (Seco, Mini 905003 Mega T) and uncoated ones (Zecha, 481.030). The two mill types allowed testing different tool sharpness levels on the cutting performance and surface finish. To ensure the sufficient level of accuracy and repeatability, the experiments were carried out on a micromilling centre (Kugler, Micromaster 5X) with a maximum spindle speed of 60 krpm with the adopted electrospindle.

The cutting optimization was carried out according to a full-factorial design with two factors, i.e. cutting speed, V_c , and feed per tooth, f_z , varied on three levels, leading to 9 runs for each milling tool. The levels for each factor are reported in Table 6.

Level	Uncoated mill		Coated mill	
	V_c [m/min]	f_z [μm]	V_c [m/min]	f_z [μm]
-1	14	0.5	14	5
0	21	1.5	21	7
1	28	2.5	28	10

Table 6. Factors level for previous test on NiP coating [31].

A series of 2-mm-long slots were milled in full slotting whilst the axial depth of cut, a_p , was set to 20 μm , which is typical for finishing passes. Surface finish was evaluated through the areal roughness parameter S_a . The central point of the experimental plan was additionally replicated twice, i.e. before and after the plan, to evaluate the tool wear, and all the experiments were replicated 3 times for a total of 33 tests per type of mill. In order to test the homogeneity of the NiP coating along the whole thickness, the three replications were carried out using new tool units but on the same insert, after machining the previous slots by face milling ($a_p = 100 \mu\text{m}$) with a $\varnothing 3$ mm flat-end mill. The results of the experiments on surface roughness are reported in Figure 100:

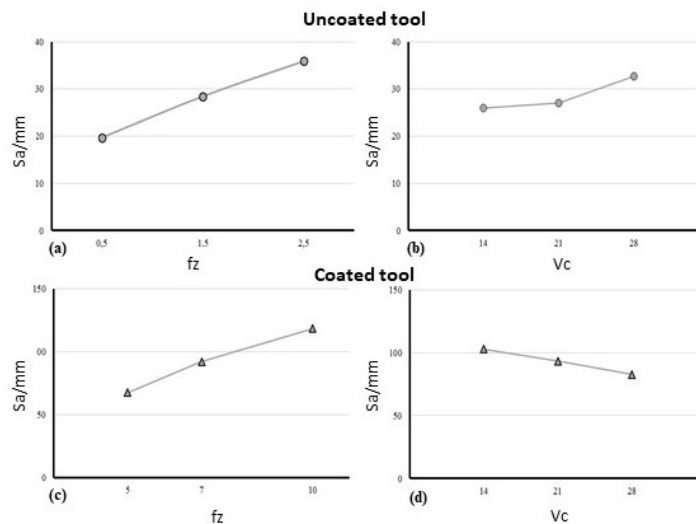


Figure 102. Effect of (a), (c) feed per tooth and (b), (d) cutting speed on surface roughness [31].

On the basis of the optimization experiments, the use of uncoated tools is the most promising for surface finishing. The second experimentation has been done to realize prismatic geometries on the NiP coated steel, using an uncoated $\varnothing 0.3$ mm ball-end milling tool (Zecha, 590.030.0030). As typical in mould manufacturing, a ball-end tool geometry (BEM) was adopted for the prism, instead of a FEM, because this tool geometry is the most suitable for achieving smooth inclined surfaces, especially when 3-axis machining cycles are adopted.

The selection of the BEM cutting parameters was driven by the optimal values obtained for the FEM tools in the optimization cutting plan, with the idea that these two tool types share most of the basic tool-material interaction phenomena that lead the cutting performance, as the surface generation. In particular, for the BEM the adopted parameters were $V_c = 20$ m/min and $f_z = 2$ μ m.

In order to vary the surface finish and to investigate its correlation with the optical performance, two NiP-coated mould inserts were machined with a Z step of 10 μ m and 4 μ m, respectively, using two uncoated $\varnothing 0.3$ mm ball-end milling tools. The scheme of the manufacturing of the workpieces is reported in Figure 103:

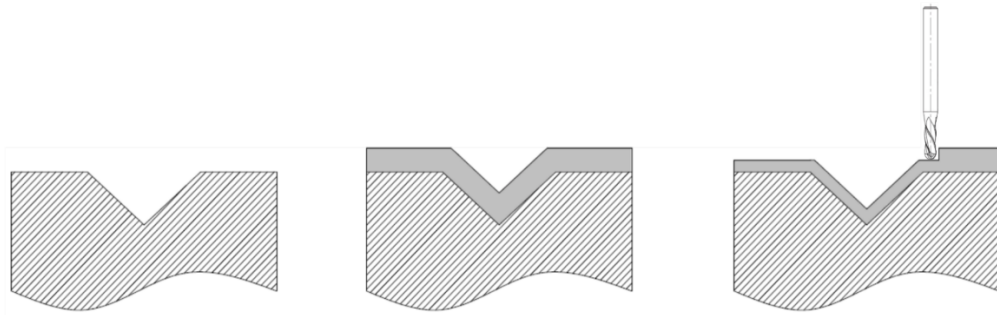


Figure 103. Scheme of the manufacturing with (a) prism fabrication using a traditional milling process, (b) NiP coating deposition and (c) finishing passes [31].

The results of the surface characterization of the NiP-coated mould inserts and their moulded samples are summarized in Table 7 for each tilt angle of the prism faces.

Tilt angle	Mould insert		Moulded RR	
	Sa [nm]	Wa [nm]	Sa [nm]	Wa [nm]
NiP 1				
45°	233	37	203	28
33.7°	86	47	94	28
18.4°	93	32	105	29
Avg.	137	39	135	28
NiP 2				
45°	67	27	72	27
33.7°	50	47	54	23
18.4°	59	38	49	20
Avg.	56	37	61	23

Table 7. Mean values of surface roughness and waviness for the NiP-coated moulds and moulded RRs [31].

In Figure 104 is reported the surface topography of the two injection moulding machined insert.

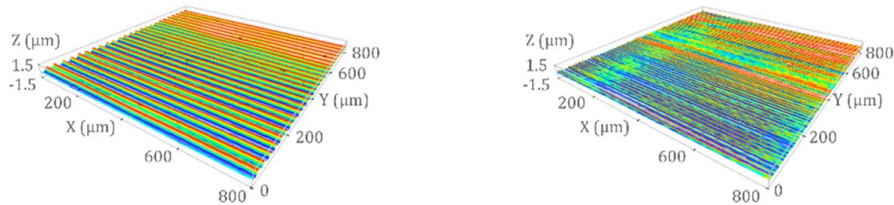


Figure 104. Surface topography of the 18.4° tilted faces on (a) NiP and (b) NiP 2 mould inserts [31].

In order to further investigate the different textures obtained on the moulded RRs, the parameters Sq and Str were calculated. Their average values are reported in Table 8. The texture aspect ratio parameter, Str, which characterizes the surface isotropy, has a value that tends to 0 and shows that machining of NiP produced an anisotropic surface with a dominant texture direction.

Parameter	NiP 1	NiP 2
Sq [nm]	151	72
Str	0.009	0.010

Table 8. Surface parameters for NiP 1 and NiP 2 [31].

7.2 Test on NiP evaluating the influence of cutting parameters

Two consecutive experimental campaigns were carried out on the NiP coated test insert, the first of which is aimed at analyzing the influence of the cutting parameters and of the inclination of the workpiece both on the surface roughness, also observing a possible formation of burrs, and on the regularity of the texture obtained; these tests are also necessary to evaluate the resistance of the tool at the different cutting conditions. Each test of cutting consists of 10 slots realized in parallel (the part program is in the Appendix A), with different radial depth of cut, determined by the desired z step and the inclination of the workpiece, as calculated in the paragraph 5.4.

The first experimental campaign has been done to test the influence of different parameters. The selected parameters and the corresponding values of each are:

- Cutting speed: 14 – 17.5 – 21 – 25 m/min
- Feed per tooth: 1 – 1.5 – 2 $\mu\text{m}/\text{tooth}$
- Inclination: 7 – 12°

The depth of cut, since it is not constant along the width of the slot, it's not a factor, but its value is selected in order to have the entire tool under cutting.

Here is reported the table, Table 9, containing all the values of the factors for each test and the values of the output variables; as output variables, it has been used the surface roughness Sa and the texture aspect ratio, Str.

Test n.	Vc [m/min]	fz [$\mu\text{m}/\text{t}$]	angle [°]	Sa [μm]	Str []
1	14	1	7	1.11	0.0233
2	14	1.5	7	1.26	0.024
3	14	2	7	1.4	0.0188
4	17.5	1	7	1.26	0.0184
5	17.5	1.5	7	1.06	0.0243
6	17.5	2	7	1.27	0.0227
7	21	1	7	1.25	0.0194
8	21	1.5	7	1.21	0.0222
9	21	2	7	1.25	0.0221
10	25	1	7	1.27	0.0191
11	25	1.5	7	1.37	0.0213
12	25	2	7	1.25	0.0192
13	14	1	12	1.2	0.0153
14	14	1.5	12	1.38	0.0146
15	14	2	12	1.22	0.0146
16	17.5	1	12	1.26	0.0145
17	17.5	1.5	12	1.16	0.0166
18	17.5	2	12	1.33	0.0157
19	21	1	12	1.12	0.0162
20	21	1.5	12	1.24	0.0142
21	21	2	12	1.27	0.014
22	25	1	12	1.32	0.0145
23	25	1.5	12	1.21	0.0203
24	25	2	12	1.2	0.0139

Table 9. Factors and outputs for NiP evaluation of cutting parameters.

During the entire experimental campaign, the tool was observed at the VTS-Marposs ultra precision tool setter mounted inside the Kern machining centre in order to monitor the wear. No obvious phenomenon of wear has been observed during all the experiments.

7.2.1 Response variable: Sa

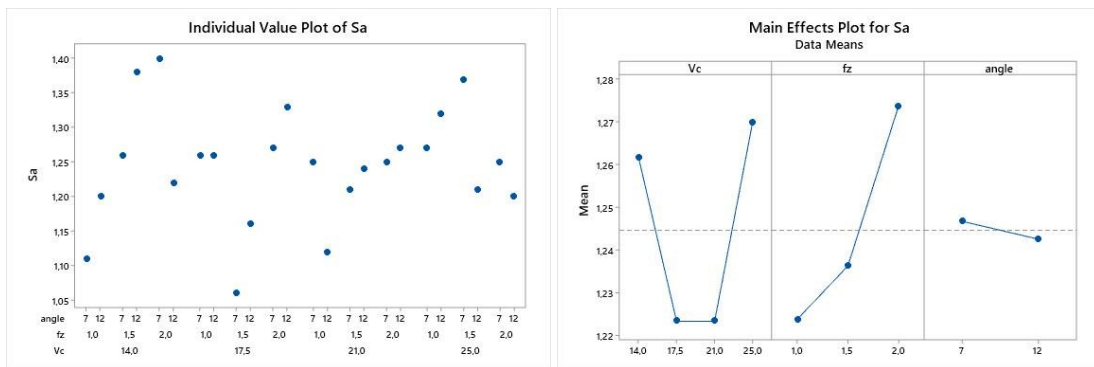


Figure 105. (a) individual value plot for Sa, (b) main effect plot for Sa, first experimental campaign on NiP coating.

The individual value plot indicates that no evident outliers appear and the variability among the factor levels appears uniform. The factors cutting speed and feed per tooth seem to be more relevant than the inclination angle of the workpiece, Figure 105. The interaction plot it's not considered because there are not any replicates.

General linear model

Factor Information

Factor	Type	Levels Values
Vc	Fixed	4 14; 17,5; 21; 25
fz	Fixed	3 1; 1,5; 2
angle	Fixed	2 7; 12

Analysis of Variance

Source	DF	Adj SS	Adj MS	F-Value	P-Value
Vc	3	0.011046	0.003682	0.47	0.709
fz	2	0.010833	0.005417	0.69	0.516
angle	1	0.000104	0.000104	0.01	0.910
Error	17	0.133812	0.007871		
Total	23	0.155796			

Model Summary

S	R-sq	R-sq(adj)	R-sq(pred)
0.0887205	14.11%	0.00%	0.00%

From the ANOVA table no factor has a p value lower than 0.05. But before concluding it's necessary to check the assumptions for standardized residuals and normality first.

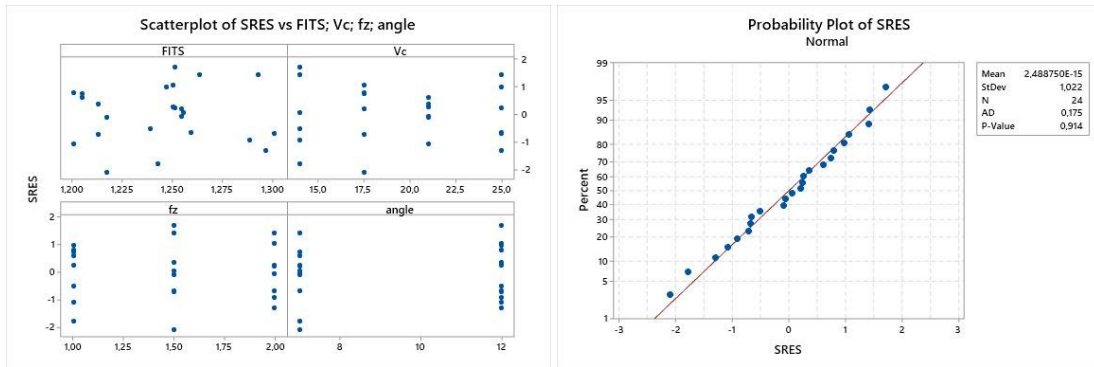


Figure 106. (a) scatterplot for Sa of SRES vs FITS; Vc; fz; angle, (b) probability plot of SRES, first experimental campaign on NiP coating.

There are not any outliers. The hypothesis of normality cannot be refused, Figure 106. It's possible to conclude that none of the factor is significant on the surface roughness generated on the test workpiece. The selection of the cutting parameters on the value of the surface roughness is not significant, thus it's possible to choose the nominal parameters given by the catalog.

7.2.2 Response variable: Str

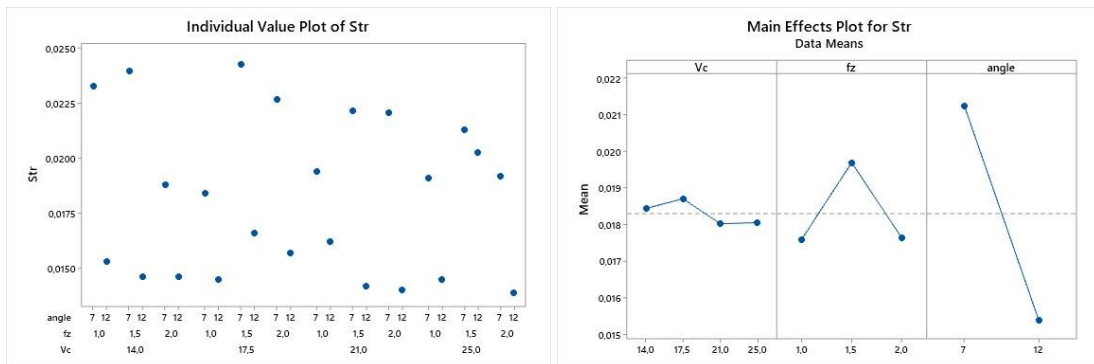


Figure 107. (a) individual value plot for Str, (b) main effect plot for Str, first experimental campaign on NiP coating.

The individual value plot indicates that no evident outliers appear and the variability among the factor levels appears uniform. The factors cutting inclination angle seems to be more relevant than the other two factors, Figure 107.

General linear model

Factor Information

Factor	Type	Levels Values
Vc	Fixed	4 14; 17,5; 21; 25
Fz	Fixed	3 1; 1,5; 2
angle	Fixed	2 7; 12

Analysis of Variance

Source	DF	Adj SS	Adj MS	F-Value	P-Value
Vc	3	0.000002	0.000001	0.18	0.909
fz	2	0.000023	0.000012	3.23	0.065
angle	1	0.000207	0.000207	57.68	0.000
Error	17	0.000061	0.000004		
Total	23	0.000292			

Model Summary

S	R-sq	R-sq(adj)	R-sq(pred)
0.0018921	79.19%	71.84%	58.51%

From the ANOVA table only the factor angle has a p value lower than 0.05, while feed per tooth has a p value close to 0.05, but higher. But before concluding it's necessary to check the assumptions for standardized residuals and normality first.

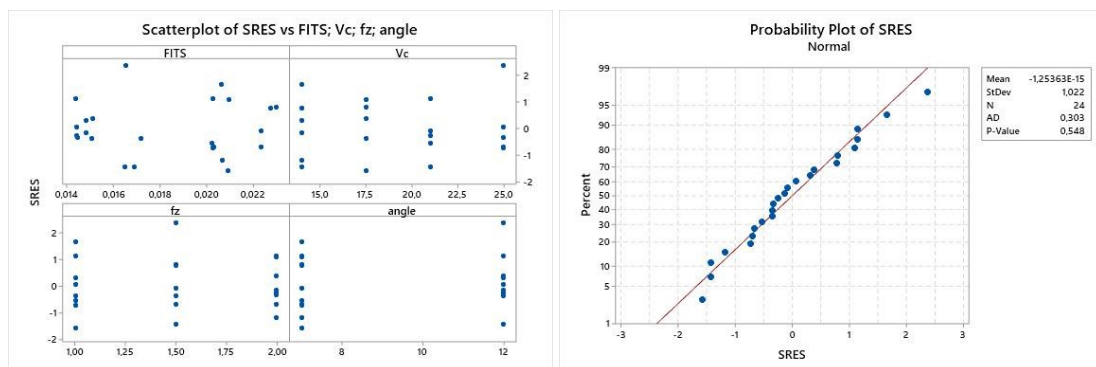


Figure 108. (a) scatterplot for Str of SRES vs FITS; Vc; fz; angle, (b) probability plot of SRES, first experimental campaign on NiP coating.

There are not any outliers. The hypothesis of normality cannot be refused, Figure 108.

It's possible to conclude that only the factor angle is significant on the surface texture ratio generated on the test workpiece. This fact is related to the definition of Str and to the calculation of the radial depth of cut by imposing z-step: therefore, for greater angles of inclination of the workpiece, the a_e is smaller and the lines generated by the passage of the tool are more dense. This greater density causes a decrease in the numerator of the formula for the calculation of Str (paragraph 2.2.2).

7.2.3 Acquired surfaces varying the cutting parameters

Here are shown, Figures 109, 110 and 111, three examples of surfaces acquired at the Mahr MarSurf CWM 100 (magnification 50X, NA 0.60) at different cutting parameters and inclinations in order to show the regularity of the texture generated on the NiP coated test insert (all the extracted surfaces are reported in Appendix F). It should be noted that the saw-tooth profile is clearly evident using a z-step equal to 5 μm , while the presence of burrs is almost nil since the tool pass eliminates the burr formed in the previous one.

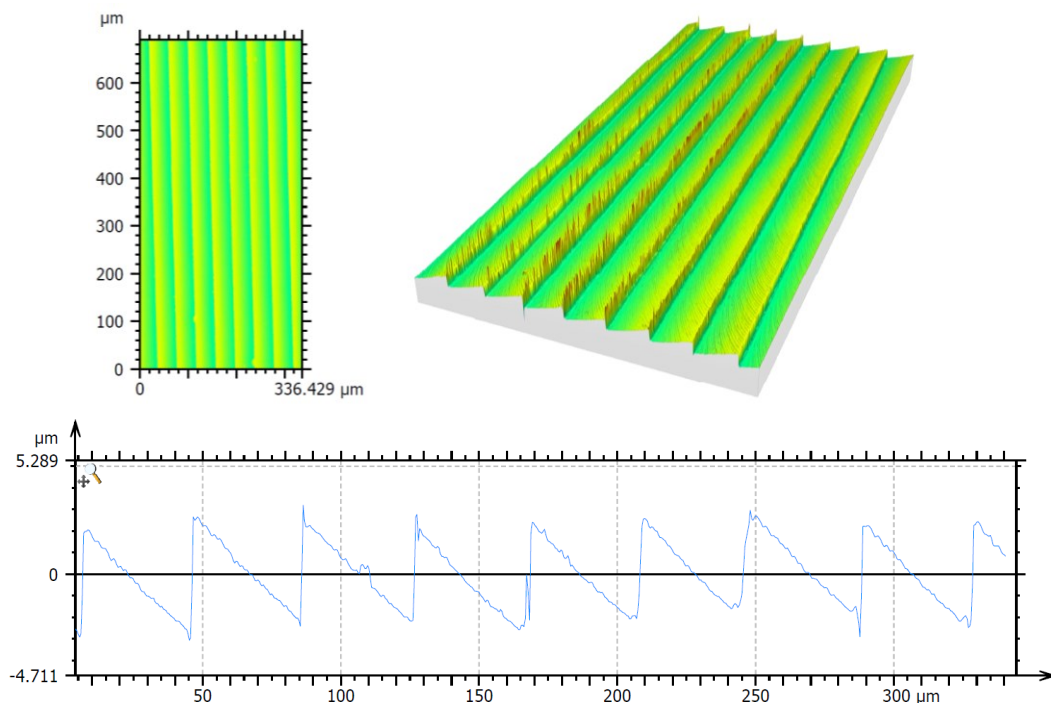


Figure 109. (a) extracted area, (b) 3D extracted area, (c) extracted profile at $V_c=14$ m/min, $f_z=1.5$ $\mu\text{m}/\text{tooth}$, angle= 7° .

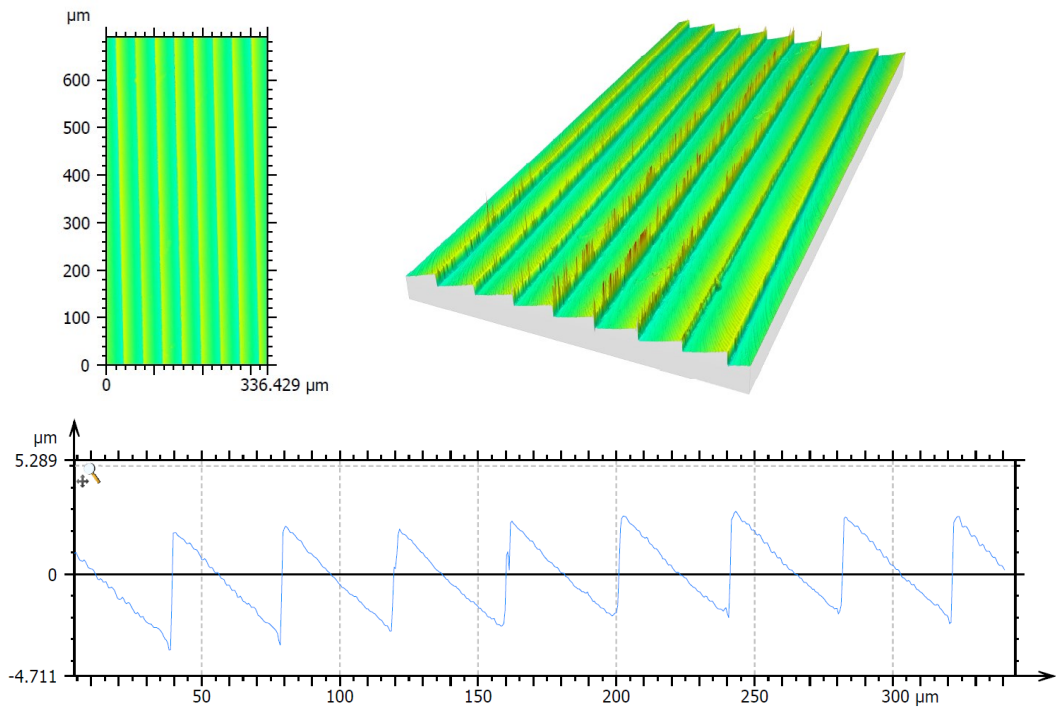


Figure 110. (a) extracted area, (b) 3D extracted area, (c) extracted profile at $V_c=21$ m/min, $f_z=2$ $\mu\text{m}/\text{tooth}$, $\text{angle}=7^\circ$.

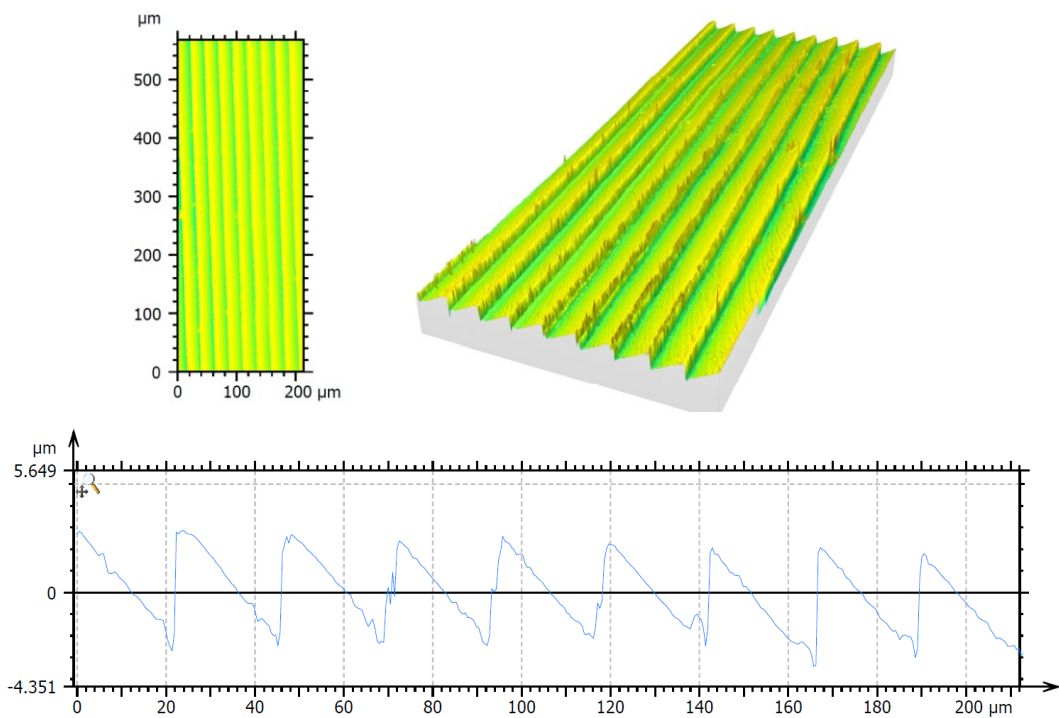


Figure 111. (a) extracted area, (b) 3D extracted area, (c) extracted profile at $V_c=17.5$ m/min, $f_z=1$ $\mu\text{m}/\text{tooth}$, $\text{angle}=12^\circ$.

7.3 Test on NiP evaluating z-step, tool and inclination angle

The second experimental campaign is aimed at analyzing the influence of the z step variation on surface roughness and texture regularity, replicating the experiment twice for each condition, using two different tools Zecha 481.030, named tool 1, new, and tool 2, already used. This experimentation is not linked with the previous, because now the need is to analyse the behaviour of the material when it is cut at different z step, considering the optimal cutting parameters taken from the previous campaign.

Since no cutting parameters were significant on the output response Sa and Str, it has been selected a cutting speed of 17.5 m/min and a feed per tooth equal to 1.5 $\mu\text{m}/\text{tooth}$ for all the cutting test.

The factor under investigation are the following:

- z step: 1 – 3 – 5 μm
- Inclination: 7 – 12°
- Tool: tool1 (new) – tool2 (already used)

Here is reported the table, Table 10, containing all the values of the factors for each test and the values of the output variables; as output variables, it has been used the surface roughness Sa and the texture aspect ratio, Str.

Test n.	z-step [μm]	tool	angle [°]	Sa [μm]	Str []
1	1	New	7	0.256	0.0145
2	3	New	7	0.686	0.0158
3	5	New	7	1.30	0.0190
4	1	Used	7	0.270	0.0152
5	3	Used	7	0.771	0.0150
6	5	Used	7	1.31	0.0189
7	1	New	12	0.152	0.0306
8	3	New	12	0.636	0.0145
9	5	New	12	1.21	0.0162
10	1	Used	12	0.157	0.0149
11	3	Used	12	0.667	0.0148
12	5	Used	12	1.24	0.0149

Table 10. Factors and outputs for NiP evaluation of z-step, tool and angle as parameters.

7.3.1 Response variable: Sa

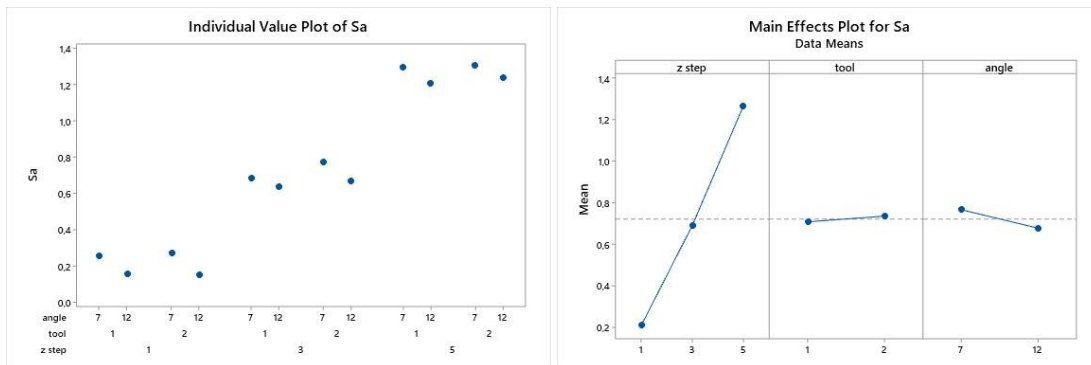


Figure 112. (a) individual value plot for Sa, (b) main effect plot for Sa, second experimental campaign on NiP coating.

The individual value plot indicates that no evident outliers appear and the variability among the factor levels appears uniform. The factor z step seems to be more relevant than the other two, Figure 112. The interaction plot it's not considered because there are not any replicates.

General linear model

Factor Information

Factor	Type	Levels Values
z step	Fixed	3 1; 3; 5
tool	Fixed	2 1; 2
angle	Fixed	2 7; 12

Analysis of Variance

Source	DF	Adj SS	Adj MS	F-Value	P-Value
z step	2	2.23719	1.11859	2576.34	0.000
tool	1	0.00227	0.00227	5.23	0.056
angle	1	0.02350	0.02350	54.12	0.000
Error	7	0.00304	0.00043		
Total	11	2.26599			

Model Summary

S	R-sq	R-sq(adj)	R-sq(pred)
0.0208370	99.87%	99.79%	99.61%

From the ANOVA table z step and angle have p values lower than 0.05, while tool has a p value close to 0.05, but a little higher. But before concluding it's necessary to check the assumptions for standardized residuals and normality first.

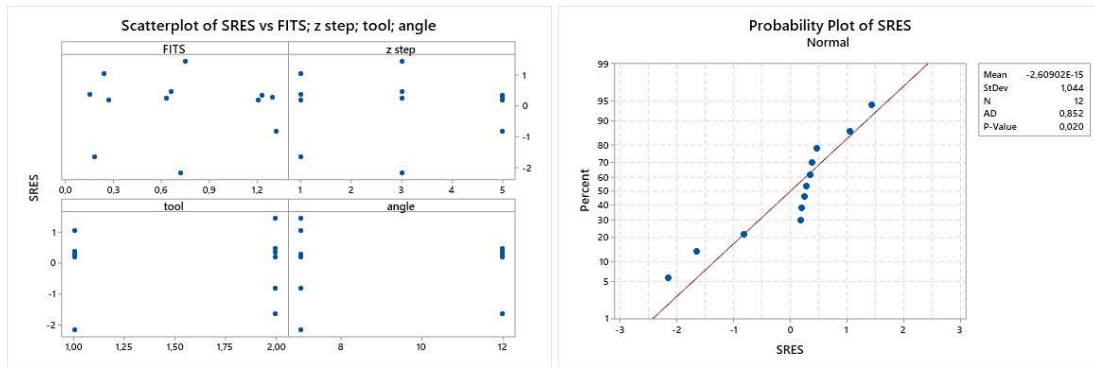


Figure 113. (a) scatterplot for S_a of SRES vs FITS; z step; tool; angle, (b) probability plot of SRES, second experimental campaign on NiP coating.

There are not any outliers. All the standardized residuals belong to the interval (-3; +3). The normality hypothesis cannot be accepted, Figure 113. If the model is reduced not considering tool as a factor, the normality assumption would not be rejected with a higher p-value. The hypothesis of normality cannot be refused, Figure 114.

It's possible to conclude that the factors z step and angle are significant on the surface roughness generated on the test workpiece, but looking at the results of the ANOVA, also the selection of a new tool is significant on surface roughness.

This conclusion is obvious because by imposing a higher z-step, a saw-tooth profile is created in the material whose height is equal to the z-step. This greater height has a direct impact on S_a measurement. The fact of using a new tool is a better choice as it turns out to be totally sharp and avoids the phenomena of wear due to prolonged cutting of material.

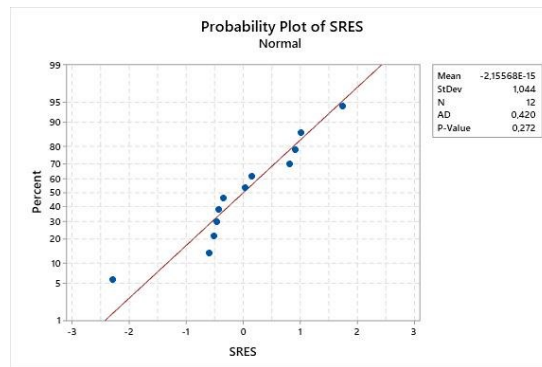


Figure 114. Probability plot of SRES of the reduced model, second experimental campaign on NiP coating.

7.3.2 Response variable: Str

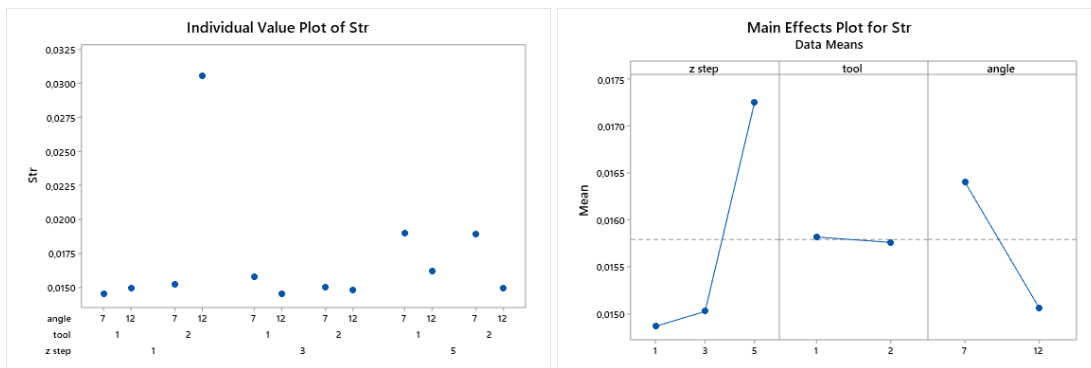


Figure 115. (a) individual value plot for Str, (b) main effect plot for Str, second experimental campaign on NiP coating.

Individual value plot shows the presence of an evident outlier. The outlier has been deleted from the analysis. The factors z step and inclination angle seem to be more relevant than tool, Figure 115. The interaction plot it's not considered because there are not any replicates.

General linear model

Factor Information

Factor	Type	Levels Values
z step	Fixed	3 1; 3; 5
tool	Fixed	2 1; 2
angle	Fixed	2 7; 12

Analysis of Variance

Source	DF	Adj SS	Adj MS	F-Value	P-Value
z step	2	0.000015	0.000008	6.80	0.029
tool	1	0.000000	0.000000	0.43	0.535
angle	1	0.000007	0.000007	5.96	0.050
Error	6	0.000007	0.000001		
Total	10	0.000027			

Model Summary

S	R-sq	R-sq(adj)	R-sq(pred)
0.0010600	75.04%	58.40%	15.07%

From the ANOVA table the factors z step and angle have p values lower than 0.05. But before concluding it's necessary to check the assumptions for standardized residuals and normality first.

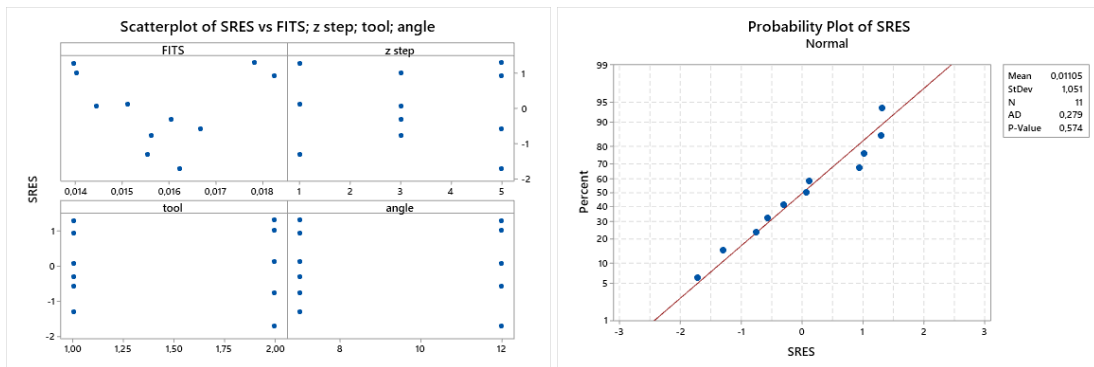


Figure 116. (a) scatterplot for Str of SRES vs FITS; Vc; fz; angle, (b) probability plot of SRES, second experimental campaign on NiP coating.

There are not any outliers. The hypothesis of normality cannot be refused, Figure 116. It's possible to conclude that the factors z step and angle are significant on the surface texture ratio generated on the test workpiece.

This result confirms what was also observed in the previous experimentation. The two quantities that are significant are exactly those that fall within the calculation of the radial depth of cut (paragraph 5.4). As previously observed, a_e has direct impact in the calculation of Str, so for smaller values of z-steps and larger of inclination angle, Str is smaller, since the numerator to calculate this quantity becomes smaller.

7.3.3 Acquired surfaces varying z-step, tool and angle

Here are shown, Figures 117, 118, 119, three examples of surfaces acquired at the Mahr MarSurf CWM 100 (magnification 50X, NA 0.60) at different z-step and inclinations in order to show the regularity of the texture generated on the NiP coated test insert (all the extracted surfaces are reported in Appendix F). All these surfaces are cut using a new tool. It should be noted that the saw-tooth profile is clearly evident using a z-step equal to 3 and 5 μm , while the regularity of the profile is lost when 1 μm is given as the value of z-step.

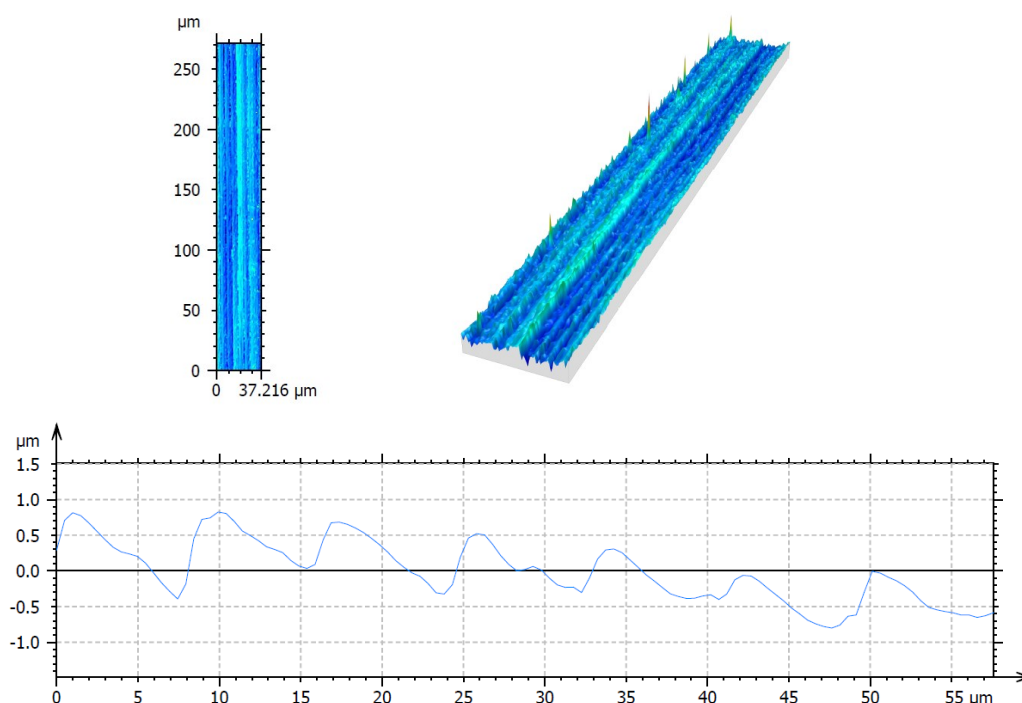


Figure 117. (a) extracted area, (b) 3D extracted area, (c) extracted profile at z-step=1 μm , new tool, angle=7°.

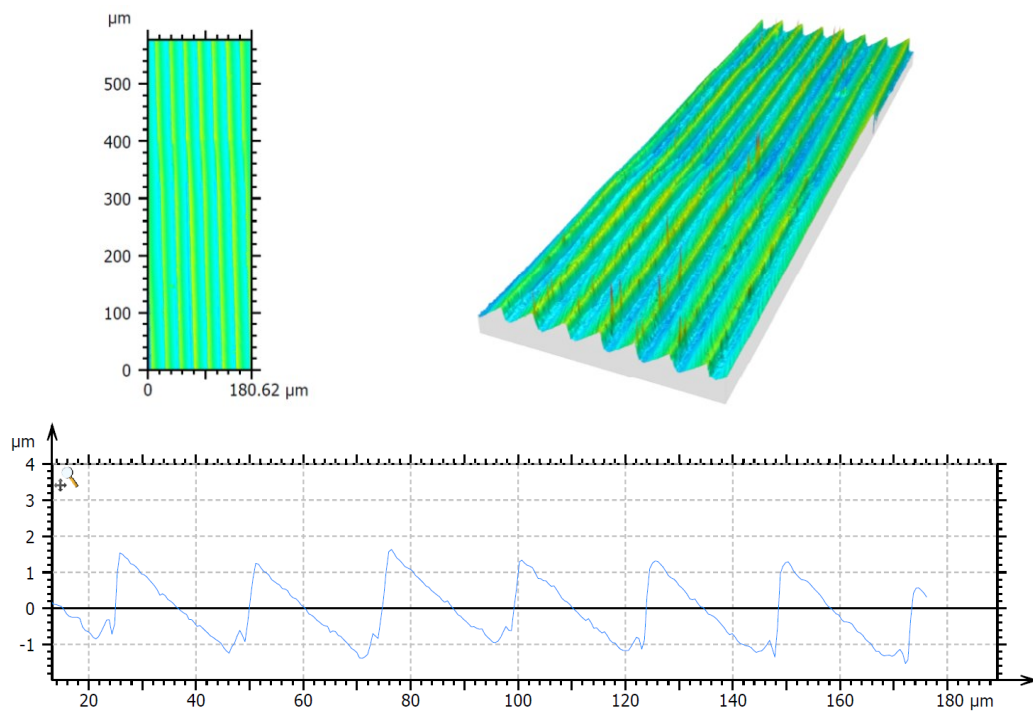


Figure 118. (a) extracted area, (b) 3D extracted area, (c) extracted profile at $z\text{-step}=3\ \mu\text{m}$, new tool, $\text{angle}=7^\circ$.

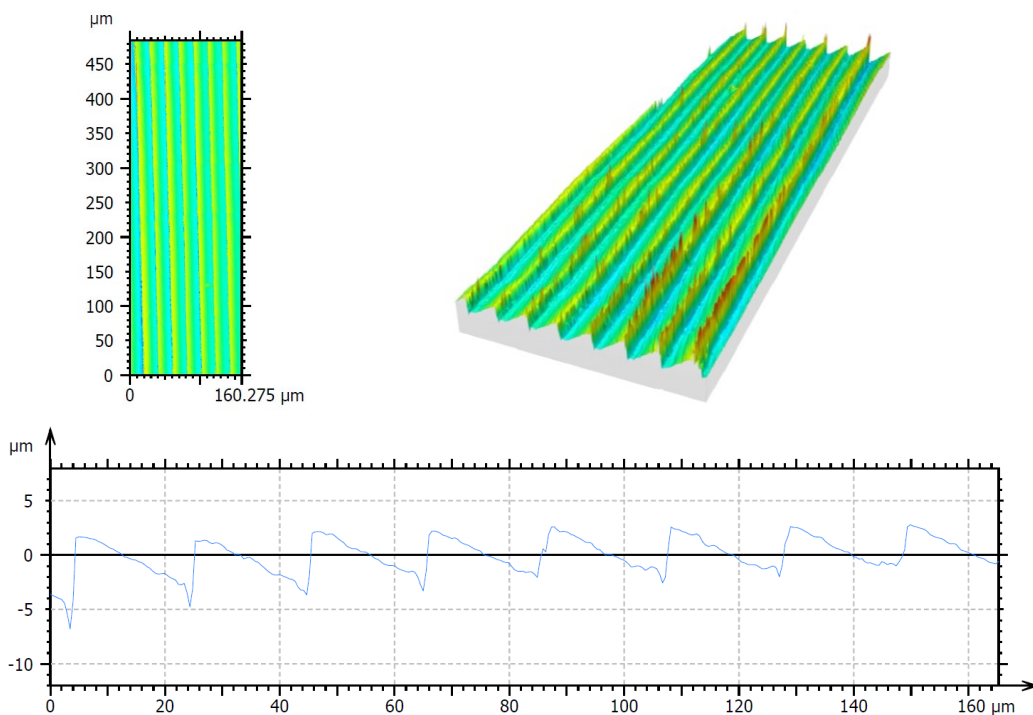


Figure 119. (a) extracted area, (b) 3D extracted area, (c) extracted profile at $z\text{-step}=5\ \mu\text{m}$, new tool, $\text{angle}=12^\circ$.

7.4 Results on NiP coating

From the two experimental campaigns it emerged that NiP coating turns out to be a good material on which to make regular profiles using micromilling. The cutting parameters are not significant on the quality of the profile created, thus it is possible to choose those recommended by the catalog. The surface generated is quite different from that achieved in previous studies by the University of Padua: the fact of using a flat end mill with an imposed z-step generates a saw-tooth profile whose peak-valley difference is exactly equal to z-step value, except for machine positioning errors and wear of the tool. In the work carried out previously, the use of a ball end mill leads to having another type of regular profile, although always saw-tooth. For this reason, by imposing a z-step of 10 μm and an inclination angle of 18.4° there is a peak-valley difference of about 1 μm , up to about 0.3 μm in the case of z-steps equal to 4 μm and angle of 45° . This is due to the fact that the geometry of the two tools is different, i.e. the FEM can be schematized as a rotating cylinder, while the BEM is like a rotating hemisphere. Therefore, an imposed z-step value on the FEM generates an equal peak-valley distance, but this does not happen in the case of a BEM, since the sphericity of the tool leads to having a smaller distance. The profiles obtained with high z-steps turn out to be very regular, while with z-steps equal to 1 μm the regularity seems to be lost, probably due to machine positioning errors and tool difficulty in cutting so little material. The following table, Table 11, summarizes the surface roughness values, Sa and surface texture ratio, Str, for the different z-steps:

z-step [μm]	Sa [μm]	Str []
1	0.209	0.0149
3	0.690	0.0150
5	1.265	0.0173

Table 11. Mean values of Sa and Str varying the z-step.

The mean values of Sa and Str increase for higher values of z-step. Regarding Sa, this is a logical consequence, since a greater z-step generates higher peaks that have an

impact on the value of the S_a which therefore increases. The values of S_{tr} instead tend to zero for all the values of z -step, which means that in all cases there is an anisotropy in the surface texture of the machined sample.

8. CONCLUSIONS

8.1 Conclusions on case study 1

H13 and Uddeholm Stavax ESR are hard steels capable of replicating regular surfaces due to the passage of a tool being processed. From the various experimental campaigns carried out, it was possible to conclude that:

- From the screening campaign in which different levels of some cutting parameters were tested, i.e. cutting speed, feed per tooth and depth of cut, it emerged that the RMS of the force in the plane and of the total force are significantly influenced by all the cutting parameters taken into consideration, while as regards surface roughness, the only significant factor is the feed. The best regularity of the profile has emerged for higher levels of cutting speed, feed and depth of cut.
- By analyzing the values of the forces obtained from the screening experiment, the mechanism of generating regular traces on the surface of the specimen was studied during the cut. It has been noted that the higher the RMS of the force in the plane is the more regular is the profile. This fact is due to the fact that for higher values of forces, the tool bends and only the front tooth comes into contact with the workpiece, generating the regular texture.
- From the design of experiments, it is showed that the factors cutting speed and depth of cut were significant for the RMS of the force in the plane and

the total force, while feed per tooth was the only significant factor on the value of surface roughness. By performing 3 replicas of each condition, the best cutting parameters were selected to process the inserts for injection moulding in order to obtain a more regular texture as possible.

- Having to work an area, whose width is higher than the tool diameter, the overlap was tested. The best percentage of overlap was 10%, while higher values generate a texture that is no longer regular, due to the lower force applied to the tool which causes less deflection and therefore the upset effect of the rear tooth that damages the already machined surface.

Once the cutting parameters and the overlap percentage to be used were selected, the three injection moulding inserts were processed. Being three inserts, the cutting parameters for the remaining two inserts have been obtained starting from the cutting force formula, which has feed per tooth and depth of cut as factors. In Figure 120, there is a photo of the machined inserts:

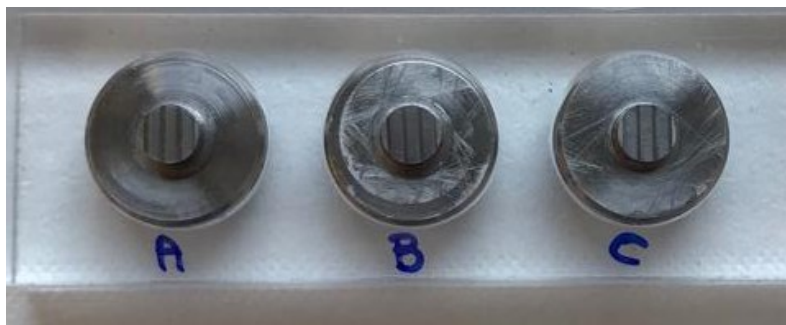


Figure 120. Picture of the three machined inserts.

8.2 Conclusions on case study 2

NiP turns out to be a good coating material on which replicate regular optical profiles.

From the various experiments conducted, it emerged that:

- As a conclusion of the first experiment, the cutting parameters, i.e. cutting speed and feed per tooth, are not significant on surface parameters, i.e. surface roughness, S_a , and surface texture ratio, Str , while the angle of inclination is significant only on the parameter Str : for higher angles Str tends

more and more to zero, confirming the fact that for both angles there is an anisotropic texture in the material, but more dense in the case of greater angles.

- As a conclusion of the second experimental campaign, the z-step and inclination angle parameters of the piece are significant, both on the surface roughness of the piece and on the surface texture ratio. Looking at the surfaces acquired at Mahr MarSurf CWM 100, it's possible to note that the profiles obtained with z-steps equal to 1 μm are not very regular, although the Str parameter is very small, thus ensuring the presence of an anisotropic texture in the material. The fact is linked both to errors in positioning the machine and to the difficulty of the tool in cutting a small part of material.
- At the end of the experiments, it is evident that there is a difference of profiles obtained with a flat end mill or with a ball end mill, used for previous experiments: due to the different geometry of the two tools, a z-step imposed using a FEM, schematized as a cylinder in rotation, generates a peak-valley distance equal to this value, but this does not happen in the case of a BEM, since it can be schematized as a rotating hemisphere, thus generating a lower peak-valley distance.

The next steps will be to replicate what was done on the test insert on the insert for injection moulding, using a number of passes greater than 10 to have a larger machined area, in order to also test the replicability of these regular profiles on a moulded sample. A first attempt has already been made on the test insert with z-steps equal to 1 and 3 μm and an inclination of 7° using a new tool, Figure 121:

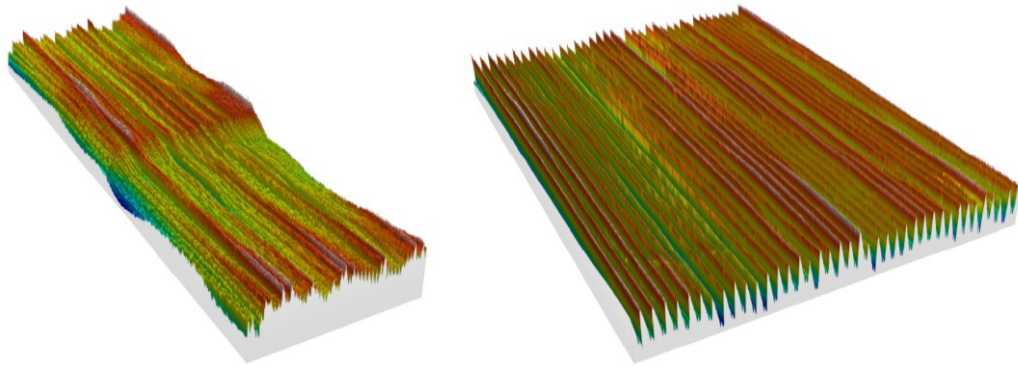


Figure 121. 3D extracted area (a) z-step=1 μm , new tool, angle=7°, (b) z-step=3 μm , new tool, angle=7°.

9. APPENDIX

9.1 Appendix A

Here are reported the G-code used on Kern to perform the cutting test:

Slots on H13:

```
BEGIN PGM Cave_H13 MM
BLK FORM 0.1 Z X-12,5 Y-12,5 Z-12
BLK FORM 0.2 X+12,5 Y+12,5 Z+0
;
CYCL DEF 247 DATUM SETTING ~
    Q339=+113 ;DATUM NUMBER
;
TOOL CALL 417 Z S30000
M3
; Cava1
L Z+100 F500
L X+0 Y+0
L X-2 Y-17
L Z-0,08 F500 ;
L Y-4,5 FZ0,03
L Z+50 F500
STOP
; Cava2
L X+0 Y-17
L Z-0,08 F500 ;
L Y-4,5 FZ0,03
L Z+50 F500
STOP
; Cava3
L X+2 Y-17
```

L Z-0,08 F500 ;
L Y-4,5 FZ0,015
L Z+50 F500
STOP
; Cava4
L X-2 Y+17
L Z-0,08 F500 ;
L Y+4,5 FZ0,005
L Z+50 F500
STOP
; Cava5
TOOL CALL 417 Z S20000
L X+0 Y+17
L Z-0,08 F500 ;
L Y+4,5 FZ0,03
L Z+50 F500
STOP
; Cava6
TOOL CALL 417 Z S30000
L X+2 Y+17
L Z-0,04 F500 ;
L Y+4,5 FZ0,03
L Z+50 F500
STOP
; Cava7
L X-17 Y-2
L Z-0,04 F500 ;
L X-4,5 FZ0,03
L Z+50 F500
STOP
; Cava8
L X-17 Y+0
L Z-0,04 F500 ;
L X-4,5 FZ0,015
L Z+50 F500
STOP
; Cava9
L X-17 Y+2
L Z-0,04 F500 ;
L X-4,5 FZ0,005
L Z+50 F500
STOP
; Cava10
TOOL CALL 417 Z S20000
L X+17 Y-2

```
L Z-0,04 F500 ;
L X+4,5 FZ0,03
L Z+50 F500
STOP
; Cava11
TOOL CALL 417 Z S10000
L X+17 Y+0
L Z-0,08 F500 ;
L X+4,5 FZ0,005
L Z+50 F500
STOP
; Cava12
L X+17 Y+2
L Z-0,04 F500 ;
L X+4,5 FZ0,005
L Z+50 F500
M30
END PGM Cave_H13 MM
```

Overlap on H13:

```
BEGIN PGM Overlap MM
BLK FORM 0.1 Z X-12,5 Y-12,5 Z-12
BLK FORM 0.2 X+12,5 Y+12,5 Z+0
;
CYCL DEF 247 DATUM SETTING ~
  Q339=+113 ;DATUM NUMBER
;
TOOL CALL 417 Z S30000
M3
;
Q1601=0,03; fz
Q1602=0,09; ap
;
; Overlap1 0%
L Z+100 F500
L X+0 Y+0
L X-2,25 Y-25
L Z-Q1602 F500 ;
L Y-4,5 FZQ1601
L Z+20 F500
L X-0,75 Y-25
L Z-Q1602 F500 ;
L Y-4,5 FZQ1601
L Z+20 F500
L X+0,75 Y-25
```

L Z-Q1602 F500 ;
L Y-4,5 FZQ1601
L Z+20 F500
L X+2,25 Y-25
L Z-Q1602 F500 ;
L Y-4,5 FZQ1601
L Z+20 F500
;
; Overlap2 10%
L X-2 Y+25
L Z-Q1602 F500 ;
L Y-4,5 FZQ1601
L Z+20 F500
L X-0,65 Y+25
L Z-Q1602 F500 ;
L Y-4,5 FZQ1601
L Z+20 F500
L X+0,7 Y+25
L Z-Q1602 F500 ;
L Y-4,5 FZQ1601
L Z+20 F500
L X+2,05 Y+25
L Z-Q1602 F500 ;
L Y-4,5 FZQ1601 L Z+20 F500
;
; Overlap3 40%
L X-25 Y-1,3
L Z-Q1602 F500 ;
L X-4,5 FZQ1601
L Z+20 F500
L X-25 Y-0,4
L Z-Q1602 F500 ;
L X-4,5 FZQ1601
L Z+20 F500
L X-25 Y+0,5
L Z-Q1602 F500 ;
L X-4,5 FZQ1601
L Z+20 F500
L X-25 Y+1,4
L Z-Q1602 F500 ;
L X-4,5 FZQ1601
L Z+20 F500
;
; Overlap4 70%
L X+25 Y-0,8

```
L Z-Q1602 F500 ;
L X+4,5 FZQ1601
L Z+20 F500
L X+25 Y-0,35
L Z-Q1602 F500 ;
L X+4,5 FZQ1601
L Z+20 F500
L X+25 Y+0,1
L Z-Q1602 F500 ;
L X+4,5 FZQ1601
L Z+20 F500
L X+25 Y+0,55
L Z-Q1602 F500 ;
L X+4,5 FZQ1601
L Z+50 F500
;
M30
END PGM Overlap MM
```

Slots on NiP:

```
BEGIN PGM slotsNiP MM
BLK FORM 0.1 Z X+0 Y+0 Z-5
BLK FORM 0.2 X+10 Y+5 Z+0
;
CYCL DEF 247 DATUM SETTING ~
  Q339=+123 ;DATUM NUMBER
;
TOOL CALL 436 Z S23000
M3
;
Q1601 = 0,03 ; Depth of cut
Q1602 = 0,0015 ; Feed per tooth
Q1603 = 0,005 ; z step
Q1604 = 0,01 ; ae
;
;Cava1
L X+0 Y+0 Z+15 F240
L X+0 Y-3 F240
L Z-Q1601 F240
L Y+2 FZQ1602
L Z+5 F240
;Cava2
L X-0,04 Y-3 F240
L Z-0,025 F240
L Y+2 FZQ1602
```

L Z+5 F240
;Cava3
L X-0,08 Y-3 F240
L Z-0,02 F240
L Y+2 FZQ160223 L Z+5 F240
;Cava4
L X-0,12 Y-3 F240
L Z-0,015 F240
L Y+2 FZQ1602
L Z+5 F240
;Cava5
L X-0,16 Y-3 F240
L Z-0,01 F240
L Y+2 FZQ1602
L Z+5 F240
;Cava6
L X-0,20 Y-3 F240
L Z-0,005 F240
L Y+2 FZQ1602
L Z+5 F240
;Cava7
L X-0,24 Y-3 F240
L Z-0 F240
L Y+2 FZQ1602
L Z+5 F240
;Cava8
L X-0,28 Y-3 F240
L Z+0,005 F240
L Y+2 FZQ1602
L Z+5 F240
;Cava9
L X-0,32 Y-3 F240
L Z+0,01 F240
L Y+2 FZQ1602
L Z+5 F240
;Cava10
L X-0,36 Y-3 F240
L Z+0,015 F240
L Y+2 FZQ1602
L Z+50 F240
;
M30
END PGM slotsNiP MM

9.2 Appendix B

KERN Evo CNC machining center

The result of intelligent evolution



As the name suggests, the KERN Evo is the product of many years of consistent development. The result of these ongoing improvements is the highest precision and productivity when milling with high and medium part quantities.

The machine's design allows maximum smoothness and an excellent surface finish ($<1 \mu\text{m}$) even at high speeds and acceleration values.

Short distances between components and drives ensure minimal angle errors, while high-resolution direct measuring systems guarantee maximum repeat accuracy. The KERN Evo can be optionally equipped with a 4th and 5th axis without compromising the stability and precision of the basic machine.

High-quality components in all peripheral modules in addition to the machine's compact design have enabled the KERN Evo to prevail in many different industries. The KERN Evo is the first choice whenever the application requires high productivity and series-tested precision on the workpiece. Its versatility and outstanding performance make the KERN Evo the most cost-effective solution in the world of high-precision machining centers.

Features and benefits at a glance:

- **High precision on the workpiece**

The axes are designed for extreme precision and provide the basis for the machine's outstanding basic accuracy. Ongoing improvements in the components and control processes help to further increase precision on the workpiece and manufacturing productivity.

- **Outstanding surface quality**

Its unique machine frame made of mineral casting gives the KERN Evo a high degree of stiffness that is essential when machining high-precision surfaces. It is insensitive to thermal influences and up to ten times better at vibration damping than conventional GG20. In addition to the quality of the installed components and the solid installation, these factors provide the basis for exceptional surface quality on the machined parts.

- **Optimal ergonomics**

The clear and balanced machine design allows full access to the working space as well as free access to the clamping surface. Thus, efficient operation is easily ensured - even in non-automated production.

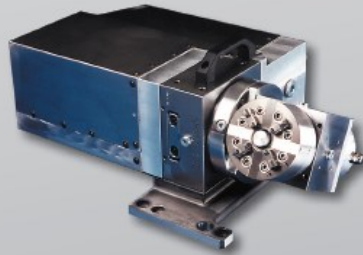
- **Flexible and fully automatable**

A comprehensive range of modules and accessories enables the KERN Evo to be tailored to your requirements and applications. Automatic workpiece loading systems can be integrated seamlessly into the machine and optimized for each application. Even after delivery, we are ready to support you with process creation and production optimization.



Workpiece loading in the workspace

Technical specifications KERN Evo



CNC precision indexing head (4th/5th axis)



Watch plates in 6-fold clamping

Axes

Traverse paths X/Y/Z: 300/280/250 mm
 Max. clamping surface: 350 x 230 mm
 Max. workpiece weight: 50 kg

4th and 5th axis

Rotary axis: 360° continuous
 Swivel axis: -10° to +100°

Spindle

HSK 25: 50,000 rpm, 6.4KW

Workpiece size

280 x 260 mm

Tool changer

HSK 25: 32, 63 or 95 capacity
 Max. tool diameter: 50 mm
 Max. tool length: 105 mm
 Chip-to-chip time: 5.5 s

Technical concept

Mineral-cast stand in monoblock design
 Optional CNC precision indexing head (4th/5th axis)
 Heidenhain ITNC 530 controller

Dimensions and weight

Weight: 3,100 kg
 Space requirements min. W/D/H: 2.50 x 2.80 x 2.20 m



Technical changes reserved

Data sheet available: <https://www.kern-microtechnik.com/en/home/>

9.3 Appendix C

Force – FMP

KISTLER
measure. analyze. innovate.

3-Component Force Link

25 x 25 x 30 mm up to 2 kN

Type 9317B

Miniature force link for measuring the three orthogonal components of a dynamic or quasistatic force acting in an arbitrary direction.

- Very extended measuring range
- High rigidity
- Minimal cross talk
- Calibrated force link
- Simple installation
- Multipole connector

Description

The force sensor is mounted under preload between two plates and, therefore can measure compression and tensile forces. The piezo element yields an electric charge which is proportional to the force. This is picked off by electrodes and transferred via a connector. The charge signal is fed via a screened cable to a charge amplifier, which converts it into a proportional output voltage. An appropriate evaluation circuit can record and further process the measurand.

Thanks to their high rigidity they cover a wide frequency range. The elastic behaviour of the test object is practically not influenced. Quasistatic measurements, are possible, too.

The sensor is mounted ground-isolated. This largely eliminates ground loop problems.

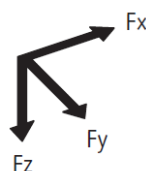
The force link is supplied calibrated. After correct installation, it is immediately ready for use without re-calibration.

Application

The force links can measure the 3 orthogonal force components easily, directly and precisely, because these sensors feature an inherently low cross talk.

Application examples

- Cutting forces
- Impact forces
- Determination of coefficients of friction



Technical Data

Range (Without moments if e.g. four force links are mounted into one force plate)	F_x, F_y	N	-1 000 ... 1 000
Range (Example with point of force application F_{xy} 12 mm above top plate)	F_x, F_y	N	-200 ... 200
Range (Point of force application F_z centric)	F_z	N	-2 000 ... 2 000
Overload		%	10
Calibrated range (Point of force application F_{xy} 7,5 mm below top plate surface)	F_x, F_y	N	0 ... 600; 0 ... 60
Calibrated range (Point of force application F_z centric)	F_z	N	0 ... 2000; 0 ... 200
Max. moments ($M_x = 0; F_z = 0$)	M_{xy}	N-m	-5/5
($M_{xy} = 0; F_z = 0$)		N-m	-4/4
Threshold		N	<0,01

9317B_000-464e-12.04

Sensitivity	F_x, F_y F_z	pC/N pC/N	≈-26 ≈-11
Linearity, each axis		% FSO	±0,5
Hysteresis, each axis		% FSO	±0,5
Cross talk (Cross talk $F_x, F_y \rightarrow F_z$ is ±3% if e.g. four force links are mounted in to one force plate)	$F_z \rightarrow F_x, F_y$ $F_x \leftrightarrow F_y$ $F_x, F_y \rightarrow F_z$	% % %	±1 ±3 ±4
Natural frequency	$f_n(x)$ $f_n(y)$ $f_n(z)$	kHz kHz kHz	≈5 ≈5 ≈21
Operating temperature range		°C	-50 ... 80
Insulation resistance		Ω	≥10 ¹³
Ground insulation		Ω	>10 ⁸
Capacitance, each channel		pF	≈39
Connector			3 pole M8 x 0,75
Weight		g	85

Multicomponent Force Plate with 4 Force Links
Four force links can be mounted together with a common top plate. Such we gain a multicomponent force plate.

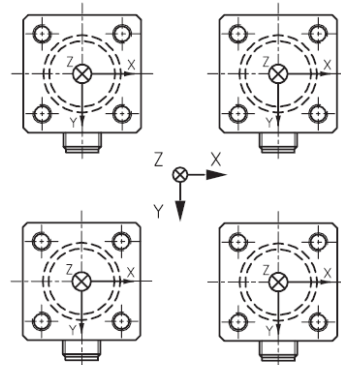


Fig. 1: Force plate with 4 force links Type 9317B

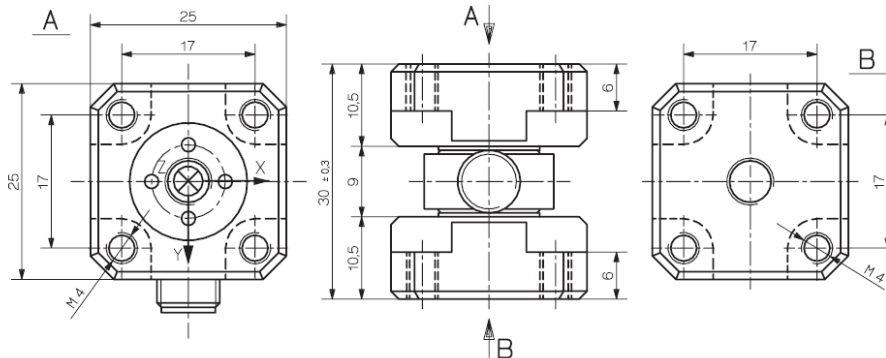


Fig. 2: Dimensions Type 9317B

9317B_000-464e-12.04

Data sheet available: <https://www.kistler.com/en/product/type-9317c/>

9.4 Appendix D

Force

KISTLER
measure. analyze. innovate.

MicroDyn

Type 9109AA

Multicomponent dynamometer up to 500 N, cover plate 30x30 mm

Multicomponent dynamometer for measuring the three orthogonal components of a force and the torque M_z . The very low threshold and the high sensitivity allow even the smallest forces to be measured. With a natural frequency higher than 15 kHz in all three axes, highly dynamic forces can be recorded with extremely high accuracy.

- Very compact design
- Patented sensor arrangement
- High sensitivity and natural frequency
- Reduced influence of temperature through compensation
- Cover plate made of hard-anodized lightweight material
- For cutting force measurements in micro-machining
- For general multicomponent force measurements

Description

The dynamometer consists of four, 3-component force sensors which are mounted under high pretension between the cover plate and the four lateral assembly elements. Thanks to this special mounting of the sensors, temperature influences can be partially compensated for and the influence of the temperature thereby minimized. The force measurement of the sensors is based on the piezoelectric principle. The application of a force causes the crystal rings installed in the sensor (one crystal ring for each of the force components that is to be measured) to release a charge that is proportional to this force. The charge signals of the four installed force sensors are internally connected and output by a 9-pin flange socket. In addition to the direct measurement of the three force components, an indirect measurement of the torque M_z is possible through an appropriate calculation. The sensors are mounted ground-isolated (dry state). Ground-loop problems can thereby be largely avoided.

The dynamometer is corrosion resistant and protected against the penetration of cooling lubricant. Together with the 8-pin connecting cable Type 1677A5, Type 1677AQ02 or Type 1679A5, the dynamometer is protected against the penetration of dust and liquids according to degree of protection IP67.

Application examples

- Multicomponent force measurement of extremely small and highly dynamic forces
- Cutting force measurement in
 - precision machining
 - micromachining
 - ultra-high precision machining of brittle materials



Technical data

Measuring range (central), Single component	F_x, F_y, F_z M_z	N N·m	-500 ... 500 -50 ... 50
Measuring range when components act simultaneously (central)	F_x, F_y, F_z M_z	N N·m	-250 ... 250 25
Calibrated measuring range			
100%	F_x, F_y, F_z	N	0 ... 500
10%	F_x, F_y, F_z	N	0 ... 50
2%	F_x, F_y, F_z	N	0 ... 10
Overload (central)	F_x, F_y, F_z M_x, M_y M_z	N N·m N·m	-1 000/1 000 -30/30 -60/60
Threshold	N		<0.002
Average sensitivity	F_x, F_y F_z	pC/N pC/N	±12.5 ±20
Linearity			
Measuring range 10% ... 100%		%/FSO	±0.5
Measuring range 0% ... <10%		%/FSO	±1.0
Hysteresis			
Measuring range 10% ... 100%		%/FSO	±0.5
Measuring range 0% ... <10%		%/FSO	±1.0
Crosstalk	$F_x \rightarrow F_y$ $F_x \rightarrow F_z$ $F_y \rightarrow F_z$ $F_y \rightarrow F_x$ $F_z \rightarrow F_x$ $F_z \rightarrow F_y$	% % % % % %	±0.4 ±0.2 ±0.4 ±0.2 ±0.2 ±0.2
Natural frequency (without additional mass)	$f_n(x)$ $f_n(y)$ $f_n(z)$	kHz kHz kHz	>15 >15 >15
Operating temperature range		°C	-20 ... 70
Capacitance	X_0, X_1, Y_1, Y_4 X_{0-4}, Y_{1-4} Z	pF pF pF	~60 ~120 ~240
Insulation resistance (20 °C)		Ω	>10 ¹¹
Ground isolation (dry state)		Ω	>10 ¹¹
Degree of protection EN60529			IP67 ^{*)}
Weight	Dynamometer Cover plate	kg kg	1.040 0.050
Mounting surface		mm	30x30

9109AA_C03-346e-08.18

9.5 Appendix E

The Matlab script used for the forces analysis is reported here:

```
clear all
clc
close all

filenames='Force 1';
cd('C:\Users\Luca\Desktop\ForceMeasurement');
[DataOut,PathName]=ReadExperireData("",'yes','no','no');
Fx=DataOut.Data(:,1);
Fy=DataOut.Data(:,2);
Fz=DataOut.Data(:,3);
figure
plot(Fx)
[xx,yy]=ginput(2);
gh=1;
eval(['Fx',num2str(gh),'=Fx(xx(1):xx(2));']);
eval(['Fy',num2str(gh),'=Fy(xx(1):xx(2));']);
eval(['Fz0',num2str(gh),'=Fz(xx(1):xx(2));']);
if 1
    % remove a trend in Fz
    eval(['begFz=mean(Fz0',num2str(gh),'(1:20));']);
    eval(['Fz',num2str(gh),'=Fz0',num2str(gh),'-begFz;']);
    eval(['endFz=mean(Fz',num2str(gh),'(end-20:end));']);
    eval(['mm=endFz/(length(Fz',num2str(gh),'));']);
    eval(['linerem=mm*(0:length(Fz',num2str(gh),'-1);']);
    % figure,plot(Fz1),hold on, plot(linerem)
    eval(['Fz',num2str(gh),'=Fz',num2str(gh),'-linerem;']);
end
gh=gh+1;
%% force analysis
Fxy1=(Fx1.^2+Fy1.^2).^0.5; %XY Plane resultant Force
TetaXY1=atan2(Fy1,Fx1); %XY planeangle
Fxz1=(Fx1.^2+Fz1.^2).^0.5; %XZ Plane resultant Force
TetaXZ1=atan2(Fz1,Fx1); %XZ planeangle
Fyz1=(Fy1.^2+Fz1.^2).^0.5; %YZ Plane resultant Force
TetaYZ1=atan2(Fz1,Fy1); %YZ planeangle
FR_tot1=(Fx1.^2+Fy1.^2+Fz1.^2).^0.5; %XYZ resultant Force
sig1=[Fx1,Fy1,Fz1,Fxy1,Fxz1,Fyz1,FR_tot1];

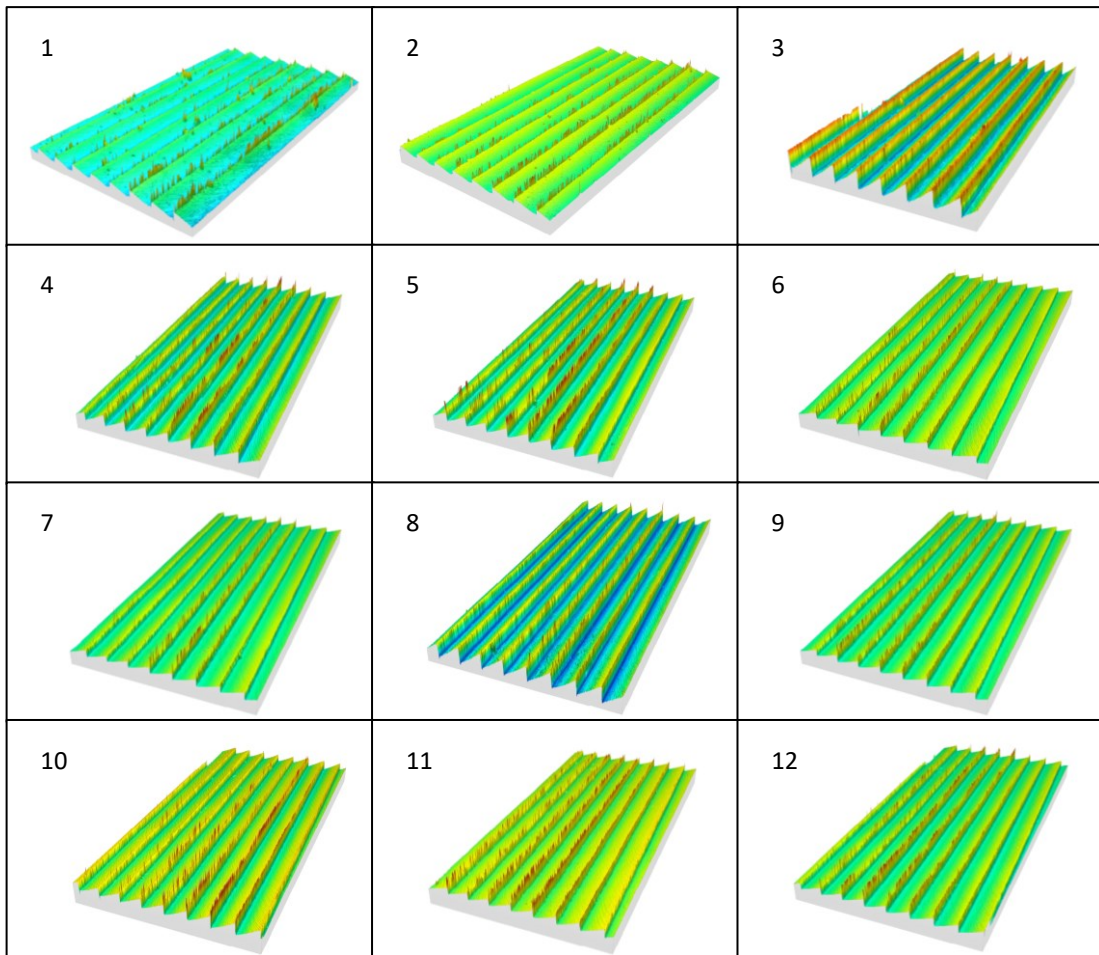
figure(1)
plot(FR_tot1)
hold on
```

```
figure(2)
plot(Fz1)
hold on
```

```
F1=rms(FR_tot1)
save(filenamees)
```

9.6 Appendix F

Here are reported tables with extracted surfaces of the different tests on NiP coating. Table 12 contains all the extracted surfaces of NiP coating on the experimental campaign aimed for testing the different cutting parameters (all the cutting parameters values are reported in Table 9, paragraph 7.2). Each surface has a number that corresponds to the number of the cutting test performed, as reported in the Table 9.



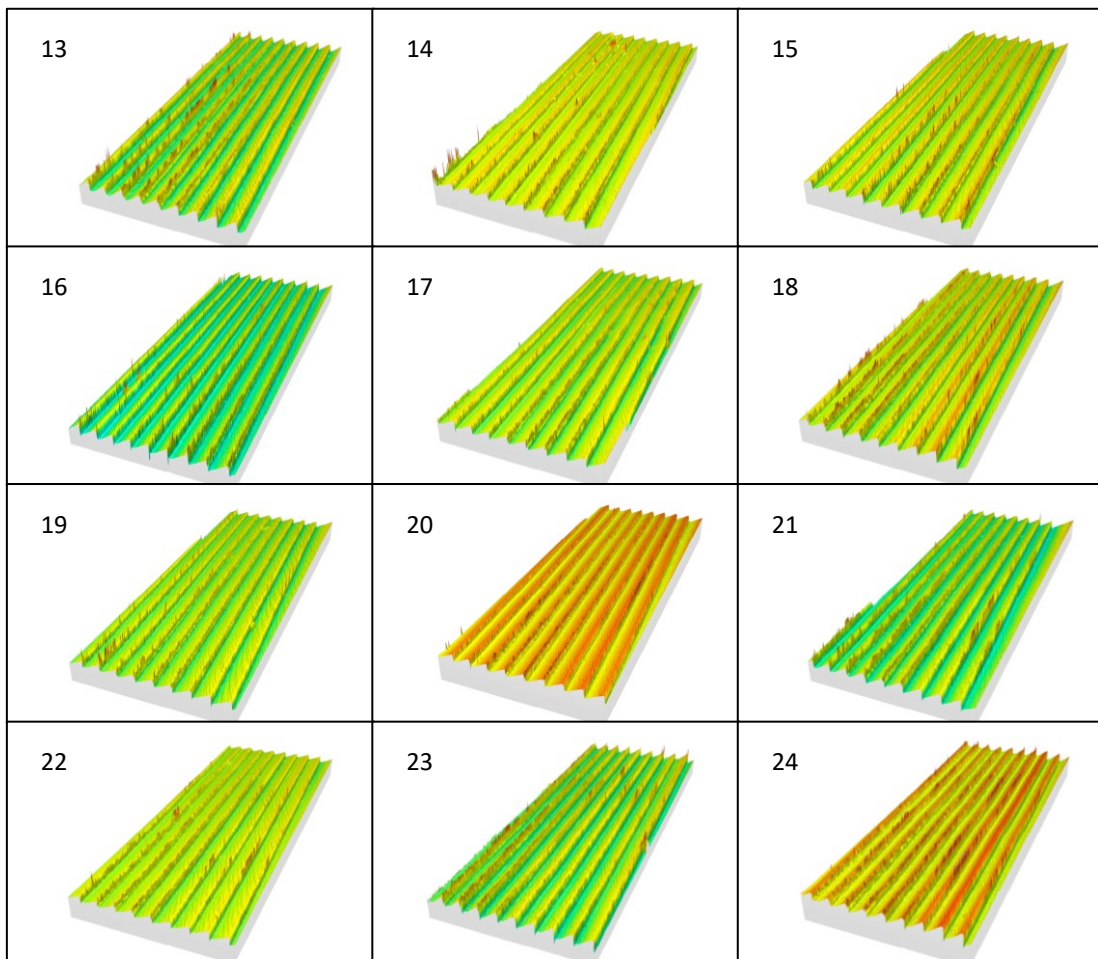
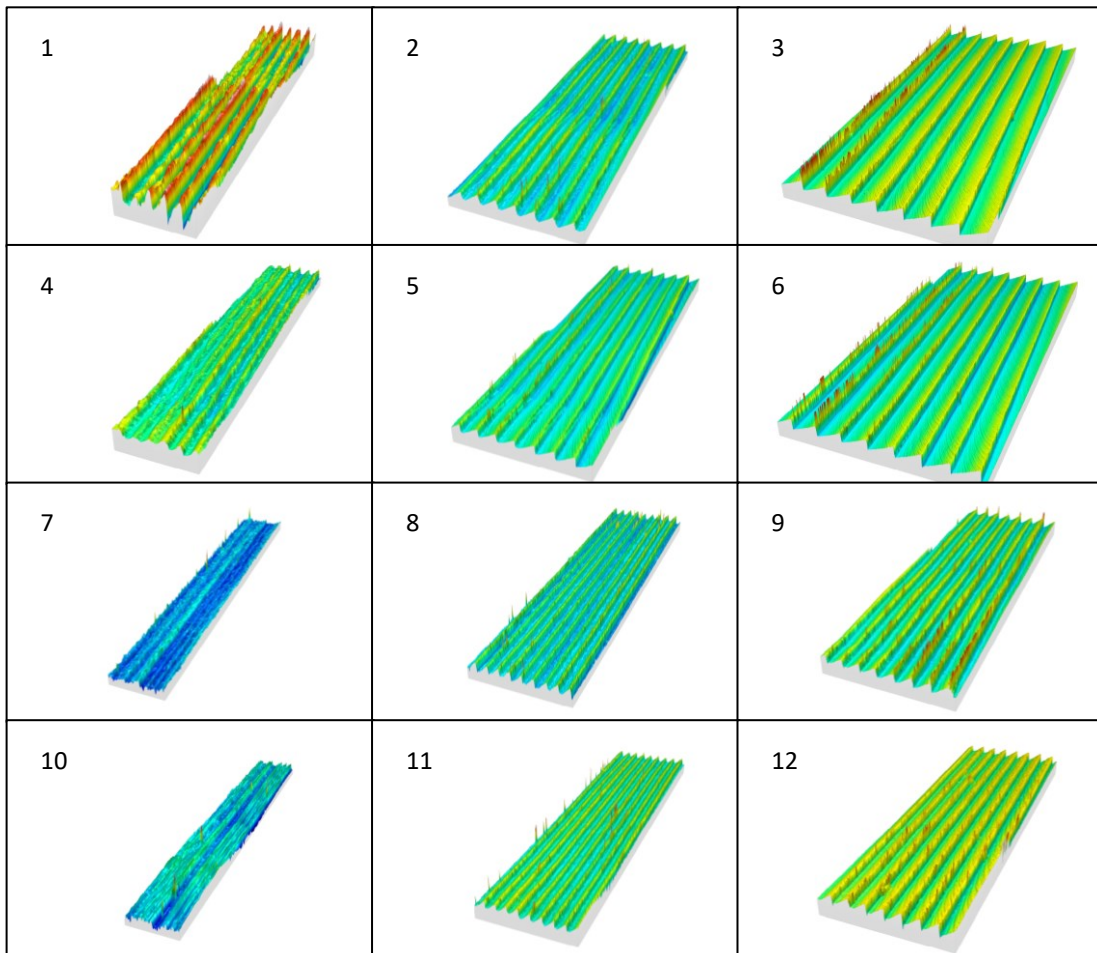


Table 12. *Extracted surfaces of NiP coating for the tests on cutting parameters.*

Table 13 contains all the extracted surfaces on NiP coating of the experimental campaign aimed for testing the z-step, tool and inclination angle (all the parameters values are reported in Table 10, paragraph 7.3). Each surface has a number that corresponds to the number of the cutting test performed, as reported in the Table 10.



References

- [1] M. A. Camara, J. C. C. Rubio, A. M. Abrao and J. P. Davim, "State of the Art on Micromilling of Materials , a Review," vol. 28, no. 8, pp. 673–685, 2012.
- [2] G. Bissacco, H. N. Hansen and L. De Chiffre, "Size Effects on Surface Generation in Micro Milling of Hardened Tool Steel," vol. 55, no. 2, pp. 3–6, 2006.
- [3] P. Sahoo, T. Pratap, K. Patra and A. A. Dyakonov, "Size effects in Micro End-Milling of Hardened P-20 Steel," vol. 5, pp. 23726–23732, 2018.
- [4] J. Chae, S. S. Park and T. Freiheit, "Investigation of micro-cutting operations," vol. 46, pp. 313–332, 2006.
- [5] A. Aramcharoen and P. T. Mativenga, "Size effect and tool geometry in micromilling of tool steel," vol. 33, pp. 402–407, 2009.
- [6] G. Bissacco, H. N. Hansen and J. Slunsky, "Modelling the cutting edge radius size effect for force prediction in micro milling," vol. 57, pp. 113–116, 2008.
- [7] M. P. Vogler, R. E. Devor and S. G. Kapoor, "Microstructure-Level Force Prediction Model for Micro-milling of Multi-Phase Materials," vol. 125, 2003.
- [8] D. Dornfeld, S. Min and Y. Takeuchi, "Recent Advances in Mechanical Micromachining," vol. 55, no. 1, pp. 745–768, 2006.
- [9] F. B. de Oliveira, A. R. Rodrigues, R. T. Coelho and A. F. de Souza, "Size effect and minimum chip thickness in micromilling," *Int. J. Mach. Tools Manuf.*, vol. 89, pp. 39–54, 2015.
- [10] C. Kim, M. Bono and J. Ni, "Experimental Analysis of Chip Formation in Micro-Milling," 2002.
- [11] X. Liu, M. B. G. Jun, R. E. Devor and S. G. Kapoor, "Cutting Mechanisms and Their Influence on Dynamic Forces, Vibrations and Stability in Micro-Endmilling," 2004.
- [12] K. Lee and D. A. Dornfeld, "Micro-burr formation and minimization through process control," vol. 29, no. September 2003, pp. 246–252, 2005.
- [13] S. Nadimi, B. Oliaei and Y. Karpaz, "Influence of tool wear on machining forces and tool deflections during micro milling," pp. 1963–1980, 2016.
- [14] H. Li, X. Lai, C. Li, J. Feng and J. Ni, "Modelling and experimental analysis of the effects of tool wear , minimum chip thickness and micro tool geometry on the surface roughness in micro-end-milling," 2008.

-
- [15] E. V. Bordatchev and A. M. K. Hafiz, "Advanced measurement and analysis of surface textures produced by micro-machining processes," 2014.
- [16] F. Blateyron, "The Areal Field Parameters," no. March, 2014.
- [17] Q. Zeng, Y. Qin, W. Chang and X. Luo, "Correlating and evaluating the functionality-related properties with surface texture parameters and specific characteristics of machined components," *Int. J. Mech. Sci.*, vol. 149, no. July, pp. 62–72, 2018.
- [18] S. N. B. Oliaei and Y. Karpat, "Experimental Investigations on Micro Milling of Stavax Stainless Steel," vol. 14, pp. 377–382, 2014.
- [19] K. S. Neo, M. Rahman, X. P. Li, H. H. Khoo, M. Sawa and Y. Maeda, "Performance evaluation of pure CBN tools for machining of steel," vol. 140, pp. 326–331, 2003.
- [20] D. Li et al., "Evaluation of optical functional surfaces on the injection moulding insert by micro milling process," no. November, pp. 2–4, 2017.
- [21] D. Li, A. Davoudinejad, Y. Zhang, G. Tosello, M. Engineering and D. K. Lyngby, "Evaluation of an improved micro milling strategy for the generation of tool steel micro features with optical functionality," pp. 978–981, 2018.
- [22] X. Wu and X. Yin, "Surface Roughness Analysis and Parameter Optimization Milling Milling," *Procedia CIRP*, vol. 71, pp. 317–321, 2018.
- [23] Y. Zhenchao, X. Yang, L. Yan, X. Jin and W. Quandai, "The effect of milling parameters on surface integrity in high-speed milling of ultrahigh strength steel," *Procedia CIRP*, vol. 71, pp. 83–88, 2018.
- [24] C. Felho, B. Karpuschewski and J. Kundrak, "Surface roughness modelling in face milling," vol. 31, pp. 136–141, 2015.
- [25] L. Morrish, R. Morton and R. Williams, "Laser diffraction for waste identification and sorting," no. June, 2012.
- [26] C. Lee, T. Kuriyagawa and D. Woo, "Optimizing the fabrication process of a high-efficiency blazed grating through diamond scribing and molding," 2010.
- [27] Y. Wang, Q. Zhao, Y. Shang, P. Lv, B. Guo and L. Zhao, "Ultra-precision machining of Fresnel microstructure on die steel using single crystal diamond tool," *J. Mater. Process. Tech.*, vol. 211, no. 12, pp. 2152–2159, 2011.
- [28] A. Holthusen, O. Riemer, J. Schmütz and A. Meier, "Mold machining and injection molding of diffractive microstructures," *J. Manuf. Process.*, vol. 26, pp. 290–294, 2017.
- [29] A. Meijer, J. A. Bergmann, E. Krebs, D. Biermann and P. Wiederkehr, "Analytical and Simulation-Based Prediction of Surface Roughness for Micromilling Hardened HSS," no. 2, 2019.
- [30] F. Baruffi, P. Parenti, F. Cacciatore, M. Annoni and G. Tosello, "Investigation on the micromilled

surface characterization through replica technology,” pp. 1–4, 2016.

- [31] G. Lucchetta, M. Sorgato, N. Milan, P. Parenti and M. Annoni, “Micromilling of NiP-coated injection molds for prismatic retroreflectors,” pp. 9–11, 2019.